



INSTITUTO DE BIOINGENIERÍA

TESIS DOCTORAL

Matrices 3D de fosfato tricálcico-silicocarnotita
con micro-/nano-estructura eutectoide y
formación *in situ* de apatito

Anabel Díaz Arca

Directora: Piedad N. de Aza Moya

Co-directora: Patricia Mazón Canales

Programa de Doctorado en Bioingeniería

Elche, 2021

INDICIOS DE CALIDAD

La Tesis Doctoral titulada “*Matrices 3D de fosfato tricálcico-silicocarnotita con micro-/nano-estructura eutectoide y formación in situ de apatito*”, realizada por Dña. ANABEL DÍAZ ARCA, con NIE: Y4937458Q, bajo la dirección de las profesoras Piedad N. De Aza Moya y Patricia Mazón Canales, se presenta bajo la modalidad de Tesis por compendio de publicaciones con los siguientes índices de calidad según el Campo de la ANEP de Ciencia y Tecnología de Materiales.

Publicaciones Científicas:

- 1. A. Díaz-Arca, P. Mazón, P.N. De Aza. Eutectoid scaffold as a potential tissue engineer guide.**

Journal of the American Ceramic Society 102 (2019) 7168-7177

DOI: 10.1111/jace.16639

Factor de Impacto (2019): 3.502

Nº de la revista en su área (2019): 3/28 (Materials Science, Ceramics)

- 2. A. Díaz-Arca, P. Ros-Tárraga, P. Mazón, P.N. De Aza. In vitro characterization of new biphasic scaffolds in the sub-system $\text{Ca}_3(\text{PO}_4)_2-\text{Ca}_5\text{SiP}_2\text{O}_{12}$.**

Ceramics International 46 (2020) 18123-18130

DOI: 10.1016/j.ceramint.2020.04.133

Factor de Impacto (2019): 3.830

Nº de la revista en su área (2019): 2/28 (Materials Science, Ceramics)

- 3. A. Díaz-Arca, P. Velásquez, P. Mazón, P.N. De Aza. Mechanism of *in vitro* reaction of a new scaffold ceramic similar to porous bone.**

Journal of the European Ceramic Society 40 (2020) 2200–2206

DOI: 10.1016/j.jeurceramsoc.2020.01.045

Factor de Impacto (2019): 4.495

Nº de la revista en su área (2019): 1/28 (Materials Science, Ceramics)

- 4. A. Díaz-Arca, P. Ros-Tárraga, M. J. Martínez Tomé, A.H. De Aza, L. Meseguer-Olmo, P. Mazón, P.N. De Aza. Micro-/Nano-Structured Ceramic Scaffolds That Mimic Natural Cancellous Bone.**

Materials 14 (2021) 1439

DOI: 10.3390/ma14061439

Factor de Impacto (2019): 3.057

Nº de la revista en su área (2019): 132/314 (Materials Science, Multidisciplinary)

Los abajo firmantes, Piedad N. De Aza Moya, Catedrática de Ciencia de Materiales e Ingeniería Metalúrgica y Directora del Grupo Ciencia de Materiales de la Universidad Miguel Hernández de Elche, y Patricia Mazón Canales, Profesora Contratada Doctora de Ciencia de Materiales e Ingeniería Metalúrgica de la misma Universidad.

INFORMAN:

Que la memoria presentada para optar al grado de Doctor por la Universidad Miguel Hernández de Elche por Dña. ANABEL DÍAZ ARCA, con NIE: Y4937458Q, titulada "*Matrices 3D de fosfato tricálcico-silicocarnotita con micro-/nano-estructura eutectoide y formación in situ de apatito*", ha sido realizada bajo nuestra dirección.

Que han revisado los contenidos científicos y los aspectos formales del trabajo y dan su conformidad para su presentación a la Comisión de Doctorado de la Universidad Miguel Hernández de Elche.

Y para que así conste, y a los efectos oportunos, firmamos el presente documento en Elche a 6 de mayo de 2021.

Fdo. Piedad N. De Aza Moya
Directora de Tesis

Fdo. Patricia Mazón Canales
Co-directora de Tesis

Piedad N. De Aza Moya, Coordinadora del Programa de Doctorado en Bioingeniería de la Universidad Miguel Hernández de Elche por Resolución Rectoral 3120/19, de 09 de diciembre de 2019

INFORMA

Que la Tesis Doctoral titulada "*Matrices 3D de fosfato tricálcico-silicocarnotita con micro-/nano-estructura eutectoide y formación in situ de apatito*", ha sido realizada por Dña. ANABEL DÍAZ ARCA, con NIE: Y4937458Q, bajo la dirección de la profesora Piedad N. De Aza Moya y la co-dirección de la profesora Patricia Mazón Canales, y da su conformidad para que sea presentada a la Comisión de Doctorado de la Universidad Miguel Hernández.

Y para que así conste, y a los efectos oportunos, firma el presente documento en Elche a 6 de mayo de 2021.

Profesora Piedad N. De Aza Moya
Coordinadora del Programa de Doctorado en Bioingeniería

AGRADECIMIENTOS

Quisiera agradecer a todas las personas e instituciones que, de una forma u otra, han contribuido a mi formación profesional y superación personal durante todo este tiempo:

En primer lugar, al Vicerrectorado de Investigación e Innovación de la Universidad Miguel Hernández de Elche por la ayuda enmarcada en dicho vicerrectorado para el apoyo a la formación de personal investigador (Resolución 0192/2018) del 23 de enero de 2018, sin la cual no hubiera sido posible desarrollar este trabajo.

A mi directora de tesis la Dra. Piedad Nieves de Aza Moya por acogerme en su grupo de trabajo, por iniciarme en un tema de investigación tan interesante, por todo el tiempo dedicado y los conocimientos transmitidos.

A mi co-directora de tesis la Dra. Patricia Mazón Canales por asesorarme continuamente en el trabajo de laboratorio, por las largas horas de análisis e interpretación de resultados y por sus consejos siempre tan oportunos.

Al Dr. Pablo Velásquez Castillo, por instruirme en el funcionamiento de los equipos de laboratorio, las herramientas informáticas y el análisis de resultados.

Al Dr. Ángel Murciano Cases por escucharme siempre con paciencia, por darme puntos de vista diferentes y por asistirme siempre en mis consultas sobre temas específicos de la investigación. También agradecerle que haya compartido conmigo sus exquisitos gustos culinarios y enológicos, sin dudas una experiencia muy especial.

Al Dr. Luis Meseguer Olmo por acogerme en su laboratorio de Biomateriales e Ingeniería de Tejidos de la Universidad Católica de San Antonio de Murcia durante 3 meses (febrero-abril de 2019) para el desarrollo de los ensayos de biocompatibilidad de los materiales con células mesenquimales humanas adultas.

A la Dra. Patricia Ros Tárraga por iniciarme en el fascinante mundo de las células, por transmitirme todos sus conocimientos y experiencias. Patricia es una

Agradecimientos

investigadora muy dinámica y estoy muy agradecida de haber trabajado con ella. También le doy las gracias por ser una buena amiga.

A Nayarit A. Mata Alayón y Carlos Navalón Donat mis compañeros de laboratorio. Ellos entienden que soy mala para esto de las dedicatorias, pero saben que son muy especiales para mí. No tengo como agradecerles todo su apoyo y todos los momentos compartidos. Más que compañeros, somos amigos y ha sido una fortuna tenerlos a mi lado durante este proceso.

A Luis Daniel por ser mi compañero y apoyarme incondicionalmente todo este tiempo. Por soportar mis momentos más difíciles e impulsarme a seguir adelante. Gracias por ser mi sostén lejos de casa.

A toda mi familia por brindarme siempre lo mejor y apoyarme incondicionalmente aun en la distancia. Son ellos mi motor impulsor.

A todos dedico este trabajo con el mayor amor y gratitud del mundo porque sin ellos nada de esto hubiera sido posible.

A todos

¡Muchas Gracias!

“Necesitamos especialmente de la imaginación en las ciencias. No todo es matemáticas y no todo es simple lógica, también se trata de un poco de belleza y poesía.”

María Montessori
Pedagoga y Científica (1870 -1952)

SIGLAS Y FÓRMULAS QUÍMICAS

AB: Alamar Blue

ah-MSCs: Células madre mesenquimales humanas adultas

ALP: Fosfatasa alcalina

ATR-FTIR: Espectroscopía de infrarrojos por transformadas de Fourier con reflectancia total atenuada

CaP: Fosfato cálcico

DCPA: Fosfato dicálcico anhidro

DCPD: Fosfato dicálcico dihidratado

EDS: Espectroscopía de energía dispersiva de rayos X

GM: Medio de cultivo basal

HA: Hidroxiapatito

ICP-OES: Espectrometría de emisión óptica de plasma acoplado inductivamente

ITO: Ingeniería de tejido óseo

OCP: Fosfato octocálcico

OM: Medio osteogénico

OMS: Organización Mundial de la Salud

PCL: Poli- ϵ -caprolactona

PEEK: Poliéster éter cetona

PGA: Ácido poliglicólico

PLA: Ácido poliláctico

PNP: p-nitrofenol

PNPP: p-nitrofenilfosfato

PPF: Fumarato de polipropileno

SAD: Difracción de electrones de área seleccionada

SBF: Suero fisiológico artificial

SEM: Microscopía electrónica de barrido

Silicato dicálcico: $2\text{CaO}\cdot\text{SiO}_2$

Silicocarnotita: $5\text{CaO}\cdot\text{SiO}_2\cdot\text{P}_2\text{O}_5$

Si- α -TCP: Alfa-fosfato tricálcico sustituido con silicio

TCP: Fosfato tricálcico, $3\text{CaO}\cdot\text{P}_2\text{O}_5$

TEM: Microscopía electrónica de transmisión

TTCP: Fosfato tetracálcico

XRD: Difracción de rayos X

RESUMEN

Las opciones terapéuticas para el tratamiento de las patologías óseas constituyen uno de los principales retos en salud pública hoy en día, por lo que se hace necesario el desarrollo de nuevas estrategias para la reconstrucción y/o sustitución del tejido óseo.

En la presente Tesis Doctoral se desarrollaron matrices 3D bifásicas de silicocarnotita y α -TCP con posibles aplicaciones en ITO. Estas se obtuvieron mediante el método de réplica sobre esponja polimérica a partir de un polvo cerámico de composición eutectoide dentro del subsistema Silicocarnotita-TCP contenido en el sistema Silicato dicálcico -TCP.

Las matrices se caracterizaron desde el punto de vista mineralógico, físico-químico, macro-/micro-/nano-estructural y biológico. Se utilizaron diversas técnicas de caracterización como: XRD, EDS, ATR-FTIR, espectroscopía Raman, porosimetría de mercurio, SEM, y TEM-SAD.

Las matrices 3D presentaron una composición mineralógica de silicocarnotita (53.6% en peso) y α -TCP (46.4% en peso) muy próxima al punto invariante eutectoide (53.4/46.6) del subsistema Silicocarnotita - TCP.

Los resultados confirmaron la posibilidad de controlar la macro-/micro-/nano-estructura de las matrices mediante la selección de la plantilla de poliuretano (25, 30 y 40 ppi) y el tratamiento térmico adecuado. En todos los casos se obtuvieron matrices 3D con estructuras porosas altamente interconectadas (83-96%) y una micro-/nano-estructura eutectoide formada por lamelas alternas de silicocarnotita y α -TCP. Mediante la velocidad de enfriamiento a través de la temperatura eutectoide (50°C/h, 16.5°C/h, 5.5°C/h) se controló el tamaño de las lamelas así como la resistencia a la compresión axial de las matrices, con valores que variaron desde 100-250 nm y 0.62 ± 0.07 MPa para una velocidad de enfriamiento de 50°C/h hasta 600-940 nm y 3.38 ± 0.06 MPa para una velocidad de enfriamiento de 5.5°C/h.

Para evaluar la posible aplicación de las matrices 3D en ITO se realizaron ensayos de bioactividad y biocompatibilidad *in vitro*. Los ensayos de bioactividad se llevaron a cabo según la norma ISO/FDIS 23317 por inmersión de las matrices

en SBF a diferentes tiempos (1-21 días). Los ensayos de biocompatibilidad se llevaron a cabo cultivando las ah-MSCs sembradas en las matrices a diferentes tiempos (7-28 días) y en diferentes medios de cultivo (GM y OM).

Los ensayos de bioactividad mostraron que las matrices 3D reaccionan en SBF disolviendo la fase de silicocarnotita y desarrollando una nanoestructura porosa de HA por transformación pseudomórfica de las lamelas de α -TCP. A continuación, y tras 21 días de inmersión en SBF, se produce la precipitación de una capa densa de HA sustituido con silicio sobre las matrices previamente transformadas.

Los estudios de biocompatibilidad mostraron que las ah-MSCs fueron capaces de adherirse y proliferar en estrecho contacto con las matrices 3D. Los ensayos AB confirmaron que el número de células y su actividad metabólica aumentaron con el tiempo de cultivo hasta los 28 días. El incremento de la actividad de la ALP con el tiempo de cultivo y la formación de nanofibras tipo colágeno con depósitos minerales sugirieron la posible diferenciación de las ah-MSCs en osteoblastos y la subsecuente formación de matriz extracelular mineralizada.

Una posible biofuncionalización con moléculas de interés para la regeneración de tejido óseo se evaluó a través de la unión de la enzima ALP con las matrices 3D. La ALP se injertó con éxito manteniendo su actividad enzimática tras 21 días de funcionalización.

Finalmente se comparó la micro-/nano-estructura de las matrices 3D obtenidas con la micro-/nano-estructura de un hueso trabecular natural de epífisis femoral de cerdo adulto. Se concluyó que las matrices 3D presentaron una composición química y una estructura muy similar a la del hueso trabecular natural examinado (porosidad, tamaño de poro y lamelas alternas con orientación aleatoria).

Para los ensayos biológicos se contó con la aprobación del Comité de Ética de la Universidad Católica San Antonio de Murcia (Referencia CE051904).

Por todo lo expuesto se puede concluir que las matrices 3D bifásicas desarrolladas en la presente Tesis Doctoral tienen una potencial aplicación en ITO.

ABSTRACT

Today's, the therapeutic options in bone pathology constitute one of the main challenges for public health. Therefore, it is necessary to development new strategies for bone tissue reconstruction and replacement.

In the present Doctoral Thesis, 3D biphasic scaffolds of silicocarnotite and α -TCP were developed with possible applications in bone tissue engineering. Scaffolds were obtained by polymer replica method from a ceramic powder with eutectoid composition within the subsystem Silicocarnotite-TCP and enclosing in the system Dicalcium silicate-TCP.

Scaffolds were characterized from the mineralogical, physico-chemical, structural and biological point of view. Several characterization techniques were used such as: XRD, EDS, ATR-FTIR, Raman spectroscopy, mercury porosimetry, SEM and TEM-SAD.

The 3D scaffolds presented a mineralogical composition of silicocarnotite (53.6 wt%) and α -TCP (46.4 wt%), which came very close to the eutectoid invariant point (53.4/46.6) within the subsystem Silicocarnotite-TCP.

The results confirmed the possibility to control the macro-/micro-/nano-structure of scaffolds by the selection of the polyurethane template (25, 30 and 40 ppi) and the suitable heat treatment. In all cases, biphasic 3D scaffolds with highly interconnected porous structures (83-96%) and a eutectoid nanostructure formed by alternating lamellae of silicocarnotite and α -TCP were obtained. It was possible to control the lamellar size and axial compressive strength of the scaffolds by the cooling rate used via the eutectoid temperature, with values that varying from 100-250 nm and 0.62 ± 0.07 MPa for a cooling rate of $50^{\circ}\text{C}/\text{h}$ to 600-940 nm and 3.38 ± 0.06 MPa for a cooling rate of $5.5^{\circ}\text{C}/\text{h}$.

In order to evaluate the possible application of the 3D scaffolds in bone tissue engineering, their bioactivity and biocompatibility were studied *in vitro*. The bioactivity test was assessed by the scaffolds immersion in SBF at different times (1-21 days), according to Standard ISO / FDIS 23317. The biocompatibility tests were performed by incubating the ah-MSCs seeded on the 3D scaffolds at different times (7-28 days) and two culture media (GM and OM).

Abstract

The bioactivity test showed that the 3D scaffolds, when placed in SBF, react firstly by dissolving the silicocarnotite phase and then developing a HA porous structure by pseudomorphic transformation of α -TCP lamellae. Afterwards, silicon substituted HA precipitation formed a dense layer on the previously transformed scaffolds after 21 days of immersion in SBF.

In vitro cell tests showed that the ah-MSCs were capable to adhere and proliferate in close contact with the 3D scaffolds. AB assays indicated that the number of cells and their metabolic activity increased with culture time up to 28 days. Increase in the ALP activity and the formation of collagen-like nanofibers meshwork together with mineral deposits suggested the possible differentiation of the ah-MSCs into osteoblasts and the subsequent formation of mineralized extracellular matrix.

The possible biofunctionalization with molecules involved in bone tissue regeneration was evaluated by ALP enzyme bonding on the 3D scaffolds. ALP was successfully grafted onto scaffolds, whose enzymatic activity was maintained after 21 days of functionalization.

Finally, a comparative SEM study between the bioinspired 3D scaffolds and natural cancellous bone of adult pig distal femoral epiphysis was performed to evaluate structural similarity. It was concluded that the 3D scaffolds presented a chemical composition and a macro-/micro-/nano-structure very close to that of the examined natural cancellous bone (porosity, pore size and alternating lamellae with random orientation).

The protocols for biological tests was approved by the Institutional Ethics Committee of the Catholic University of Murcia (Reference CE051904).

Because of the above, it can be concluded that the 3D biphasic scaffolds developed in this Doctoral Thesis have a potential application in bone tissue engineering.

ÍNDICE DE CONTENIDOS

1. Introducción.....	1
1.1. Tejido óseo.....	2
1.2. Ingeniería de tejidos y regeneración ósea	6
1.2.1. Matrices en ingeniería de tejido óseo	6
1.2.2. Biomateriales aplicados al diseño de matrices.....	8
1.2.2.1. Fosfatos cárnicos.....	9
1.3. Diagramas de equilibrio y diseño de cerámicas	10
1.3.1. Sistema $2\text{CaO}\cdot\text{SiO}_2 - 3\text{CaO}\cdot\text{P}_2\text{O}_5$	11
2. Objetivos	15
3. Materiales y Métodos	17
3.1. Síntesis de los polvos cerámicos.....	17
3.2. Caracterización de los polvos cerámicos.....	17
3.3. Obtención de las matrices 3D cerámicas.....	17
3.4. Caracterización de las matrices 3D	18
3.5. Ensayos de bioactividad <i>in vitro</i>	18
3.6. Ensayos de biocompatibilidad <i>in vitro</i>	19
3.7. Funcionalización con fosfatasa alcalina.....	21
3.8. Estudio comparativo con hueso trabecular	21
4. Resultados	23
4.1. Caracterización de los polvos cerámicos.....	23
4.2. Obtención y caracterización de las matrices 3D	23
4.3. Ensayos de bioactividad <i>in vitro</i>	25
4.4. Ensayos de biocompatibilidad <i>in vitro</i>	27
4.5. Funcionalización con fosfatasa alcalina.....	29
4.6. Estudio comparativo con hueso trabecular	30
5. Discusión	32
6. Conclusiones.....	41
7. Proyecciones Futuras.....	43
8. Referencias	45
9. Anexos: Compendio de Artículos.....	54
9.1. Artículo 1.....	54
9.2. Artículo 2.....	65
9.3. Artículo 3.....	74
9.4. Artículo 4.....	82

1. Introducción

En la actualidad, las opciones terapéuticas para el tratamiento de enfermedades y traumatismos que afectan al sistema óseo constituyen uno de los principales retos en salud pública.

El sistema óseo presenta una estructura compleja y dinámica la cual desempeña importantes funciones como son: sostén, movilidad y protección de órganos. Al igual que muchas otras partes de nuestro cuerpo los huesos se encuentran en constante renovación. El tejido más viejo se va reemplazando por tejido recién formado en un ciclo de remodelación que permite reforzar su estructura. Sin embargo, diversas patologías pueden alterar el correcto funcionamiento de este ciclo y derivar en daños estructurales severos.

Las patologías del sistema óseo constituyen una de las principales causas de discapacidad funcional y dolor crónico a nivel mundial que limitan enormemente la calidad de vida de las personas. Según datos de la OMS entre un 20-30% de la población presenta algún tipo de discapacidad ósea [1]. El hueso es el segundo tejido más transplantado a nivel mundial con al menos cuatro millones de operaciones en el año 2020 [2]. En consecuencia, el número de cirugías ortopédicas crece entre un 10-12% anualmente a nivel mundial [3]. Se prevé un aumento significativo en la incidencia de dichas patologías debido a múltiples factores como el acelerado envejecimiento de la población mundial, el incremento de accidentes, la escasa actividad física y la mala nutrición [4]. En este sentido, la reconstrucción de defectos óseos continuará siendo un reto importante para la cirugía ortopédica en los próximos años.

Tradicionalmente, los xenoinjertos, los aloinjertos y, especialmente, los autoinjertos han sido las opciones terapéuticas más difundidas en la práctica clínica. Sin embargo, estos presentan una serie de inconvenientes asociados a la cantidad limitada de tejido, la morbilidad del sitio donante, los riesgos de incompatibilidad inmunológica y de transmisión de enfermedades [5,6]. Estas limitaciones reducen significativamente las opciones de tratamiento, por lo que la cirugía ortopédica se apoya en el uso de biomateriales para la corrección de

defectos óseos. Los materiales metálicos han sido los más utilizados, principalmente en la fabricación de prótesis, placas y tornillos de fijación para brindar soporte estructural en artroplastias articulares y fracturas de huesos largos. No obstante, los metales presentan muy baja osteointegración y un valor de módulo de Young muy superior al del hueso natural, lo que con frecuencia provoca la resorción del tejido óseo circundante (osteopenia proximal) y por consiguiente el fallo del implante [7,8].

Por tanto, el desarrollo de nuevas estrategias para la reconstrucción y/o sustitución del tejido óseo constituye un campo de investigación con alto impacto socio-económico. Las principales investigaciones se encuentran dirigidas hacia la medicina regenerativa y al desarrollo de sistemas de liberación de fármacos, superficies biofuncionales y matrices 3D para ingeniería de tejido [6,7,9]. El tratamiento de los defectos y fracturas óseas mediante estas técnicas produce la regeneración del tejido respetando la anatomía y recuperando la funcionalidad del mismo.

1.1. Tejido óseo

El tejido óseo se clasifica como un tejido conjuntivo micro-/nano-estructurado, muy vascularizado, y altamente especializado. Conocer sus principales características resulta esencial para el desarrollo de nuevos biomateriales dirigidos a su tratamiento y regeneración.

Desde el punto de vista anatómico, el tejido óseo exhibe una organización jerárquica que incluye diferentes niveles: macroestructural (hueso cortical y hueso trabecular) (Figura 1), microestructural (osteonas, trabéculas y células) y nanoestructural (laminillas, fibras de colágeno, proteínas y minerales). En cuanto a su composición, se encuentra integrado por diferentes tipos de células y una matriz orgánica mineralizada.

Hueso cortical

El hueso cortical constituye la zona más externa y cumple importantes funciones biomecánicas y de protección. Presenta una porosidad variable entre el 3-12% con una densidad promedio de 1.80 g/cm³. Sus propiedades mecánicas están

muy influenciadas por la porosidad y el grado de mineralización, que varían en función de la edad y la localización anatómica [10,11].

La matriz del hueso cortical se encuentra ordenada en forma de estructuras laminares concéntricas llamadas osteonas. Cada osteona constituye un cilindro alargado que se orienta paralelo al eje longitudinal del hueso, con un diámetro de aproximadamente 200-250 µm. En su interior se alojan, en sentido longitudinal, los canales de Havers por los que discurren vasos sanguíneos y fibras nerviosas. En sentido horizontal, conectando los canales de Havers, se encuentran los canales de Volkmann (Figura 1).

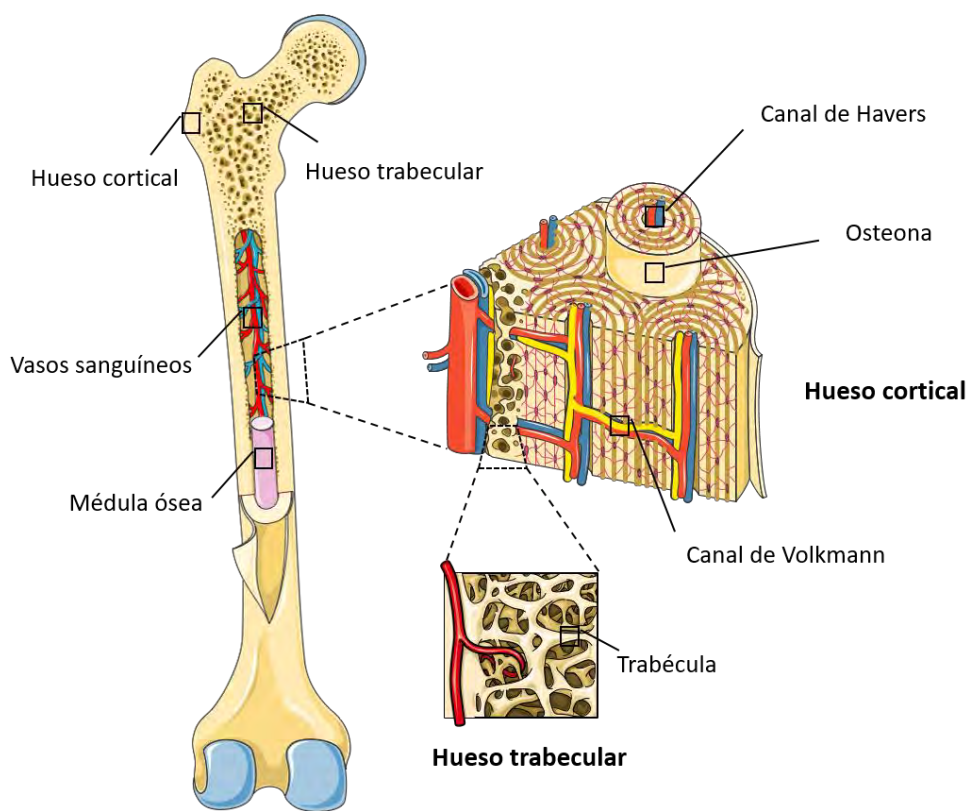


Figura 1: Anatomía general del tejido óseo [Servier Medical Art].

Hueso trabecular

El hueso trabecular constituye la zona más interna y su principal función es alojar la médula ósea hematopoyética. Su alta porosidad y la elevada interconexión entre poros permiten que discurran por él numerosos nervios y vasos sanguíneos [10,11]. Sus propiedades mecánicas se encuentran muy influenciadas también por la edad y la localización anatómica.

El hueso trabecular presenta una matriz ordenada en forma de trabéculas aleatorias con diámetros que varían entre 50-300 μm (Figura 1). La estructura del hueso trabecular es menos densa que la del cortical con una porosidad entre el 50-90% y una densidad promedio de 0.2 g/cm³ [10].

Matriz ósea

Desde el punto de vista químico, la matriz ósea se compone de una fase orgánica y una inorgánica. La fase orgánica representa entre un 25-30% del peso total y está formada principalmente por colágeno, lípidos y otras proteínas no colágenas. La fase inorgánica representa entre un 65-70% del peso del hueso y su componente mayoritario son cristales de apatito no estequiométrico, carbonatado y deficiente en calcio. Estos cristales de apatito biológico varían entre 25-50 nm y pueden presentar pequeñas sustituciones de otros iones como magnesio, sodio, potasio, estroncio y flúor. Finalmente, el tejido óseo también contiene agua que representa entre un 5-8% de su peso.

Células del tejido óseo

Las células del tejido óseo se encuentran dentro de la propia matriz o en la médula ósea hematopoyética, rica en células mesenquimales indiferenciadas. Estas células pueden dar origen a cinco estirpes celulares distintas: osteoblastos, fibroblastos, condroblastos, mioblastos y adipocitos, en respuesta a diferentes factores de señalización.

A medida que las células precursoras se diferencian, expresan proteínas o marcadores específicos de su función en la membrana celular. El colágeno tipo I y la ALP se expresan de manera temprana en las células osteoprogenitoras. Los principales tipos de células que podemos distinguir en el tejido óseo son: osteoblastos, osteocitos, osteoclastos y células del revestimiento óseo.

Los osteoblastos son los encargados de formar el nuevo tejido óseo. Son células grandes de entre 20-30 μm que se encuentran en las superficies externas de los huesos y en las cavidades óseas. Los osteoblastos provienen de las células mesenquimales indiferenciadas de la médula ósea, el periostio y el endostio. En la fase inicial de la formación de nuevo hueso los osteoblastos secretan moléculas de colágeno que polimerizan con rapidez en forma de nanofibras. El

tejido resultante de este proceso se denomina osteoide o matriz orgánica. Los osteoblastos sintetizan osteoide a un ritmo de 2 a 3 μm por día. A medida que se forma la matriz orgánica algunos osteoblastos quedan atrapados en su interior y entran en fase de reposo, formándose así los osteocitos. Estos últimos son las células más abundantes del tejido óseo y se organizan formando una red celular interconectada que garantiza el intercambio de nutrientes y oxígeno.

Tras la formación del osteoide y favorecido por la expresión de enzimas específicas como la ALP, ocurre el proceso de biominerilización de la matriz orgánica. Esto consiste en la precipitación, principalmente, de iones Ca^{2+} y grupos PO_4^{3-} desde el medio extracelular sobre la superficie de las fibras de colágeno. El precipitado aparece primero a intervalos a lo largo de las fibras de colágeno, formando nichos pequeños que se multiplican y crecen para formar cristales de apatito. La mineralización ocurre a un ritmo de 1-2 μm por día. La vida media de los osteoblastos humanos es de 1 a 10 semanas, al término de las cuales pueden desaparecer por apoptosis o transformarse en osteocitos o células del revestimiento óseo [11].

El hueso también se encuentra bajo reabsorción continua por la acción de los osteoclastos, que son células grandes (100 μm), fagocitarias y multinucleadas que disuelven la matriz orgánica mineralizada. Los osteoclastos reabsorben hueso durante unas tres semanas excavando en túneles de entre 0.2-1 mm de diámetro, al cabo de este tiempo los osteoclastos dejan lugar a los osteoblastos que invaden el túnel y comienzan la formación de hueso nuevo en la cavidad [11].

En condiciones normales las tasas de reabsorción/formación se equilibran entre sí de forma que la masa ósea total permanece constante. El remodelado óseo es, por tanto, un proceso de reconstrucción que permite mantener las características estructurales y funcionales del hueso. Un desequilibrio de este proceso, bien por exceso o por defecto, deriva en una patología ósea y en muchos casos se requiere de la intervención clínica para la reconstrucción y/o sustitución del tejido dañado.

1.2. Ingeniería de tejidos y regeneración ósea

La ingeniería de tejidos se define como un campo multidisciplinar que busca restaurar los tejidos dañados a su condición original, estimulando los propios mecanismos naturales de reparación mediante el uso de células, factores de señalización y biomateriales [12,13].

Las células son las encargadas de formar el nuevo tejido. Preferentemente se utilizan células madre indiferenciadas ya que son capaces de dar origen a los distintos tipos celulares del organismo, en nuestro caso, células osteoprogenitoras. En ITO la capacidad de producir nuevo tejido por la acción de las células se conoce como osteogénesis.

Por su parte, los factores de señalización son los encargados de estimular a las células madre indiferenciadas para diferenciar a un tipo celular específico. Concretamente para ITO estimulan la diferenciación hacia células osteoprogenitoras, lo que se conoce como osteoinducción.

Por último, un biomaterial en este contexto hace referencia a una matriz 3D temporal que proporciona una arquitectura y entorno específicos de soporte para el anclaje celular y organización del tejido neoformado, lo que se conoce como osteoconducción en ITO [14]. Estas matrices 3D constituyen la unidad básica dentro de la triada célula-señal-biomaterial, ya que se pueden utilizar simplemente como sistemas no funcionalizados o como vehículos para las células y/o los factores de señalización. Por tanto, el diseño de las mismas representa un punto clave para la ingeniería de tejidos [15].

1.2.1. Matrices en ingeniería de tejido óseo

A día de hoy no existe un consenso en cuanto a lo que sería una definición única de matriz 3D para ITO. Dado que los huesos tienen formas y estructuras muy diferentes, según su edad, función y ubicación, serían necesarias matrices de diversos tamaños, formas, porosidades y resistencias mecánicas.

A grandes rasgos, se espera que una matriz 3D para regeneración de tejido óseo mimetice la composición química y estructura jerárquica (desde la macro hasta

la nanoscala) del hueso natural. La misma, debe actuar como un soporte temporal en 3D sobre el cual las células se adhieran, proliferen, diferencien y se organicen hasta formar el nuevo tejido.

Para diseñar y fabricar matrices adecuadas en ITO se han de tener en cuenta una serie de criterios importantes que deben cumplir dichas matrices, entre los cuales destacan [6,15-20]:

- Composición y requerimientos biológicos: Selección de materiales biocompatibles, bioactivos y biorreabsorbibles con tasas de degradación acordes a la velocidad de regeneración y crecimiento del nuevo tejido.
- Procesamiento y estructura: Mediante el control de la forma y el tamaño, se debe poder obtener una arquitectura a medida con el defecto óseo.
- Porosidad, interconectividad y tamaño de poro: Deben presentar una estructura jerarquizada en forma de red porosa altamente interconectada con tamaños de poros que permitan el desarrollo celular, el crecimiento del tejido, la vascularización y el transporte de nutrientes y sustancias de desechos metabólicos.
- Topografía y química de superficie: Las características superficiales deben facilitar la adhesión y proliferación celular, así como la adsorción de metabolitos biológicos. Las superficies irregulares presentan mayor área específica, proporcionando más sitios de unión para los receptores de las membranas celulares y mejorando la biocompatibilidad.
- Funcionalización: Deben tener la capacidad de retener moléculas bioactivas que influyan en la regeneración ósea natural, permitiendo su liberación de forma local y dirigida.
- Productos de disolución: Influyen en las células para promover su proliferación y diferenciación hacia linajes formadores de hueso.
- Osteointegración: Integrarse al tejido circundante mediante enlaces químicos/físicos estables.
- Propiedades mecánicas: Proporcionar soporte mecánico adecuado para las fuerzas de carga según el sitio de implantación. Así como que dichas propiedades se mantengan en el tiempo.

1.2.2. Biomateriales aplicados al diseño de matrices

Con el fin de cumplir los requisitos biológicos, estructurales y mecánicos citados con anterioridad; se ha investigado ampliamente con distintos tipos de biomateriales para la fabricación de matrices en ITO, estando los polímeros y las cerámicas a la cabeza de las principales investigaciones.

Los polímeros de origen natural (colágeno tipo I, fibrina, ácido hialurónico y quitosano) presentan buena biocompatibilidad y bioactividad, sin embargo, su uso se encuentra limitado por la baja estabilidad mecánica [21,22]. Los de origen sintético (PPF, PCL, PLA, PGA, PEEK, etc.) presentan propiedades mecánicas superiores a los de origen natural, pero una capacidad bioactiva menor [23]. En muchas ocasiones requieren ser modificados con CaPs y vidrios bioactivos para aumentar la osteointegración [24,25]. Por último, los productos de degradación de los polímeros sintéticos pueden producir inflamación del tejido por bioacumulación y en muchos casos se desconocen los posibles efectos sistémicos [26,27].

Las cerámicas constituyen una alternativa muy prometedora para dar solución a algunos de los principales problemas asociados al uso de polímeros. En general, se han utilizado en diversas aplicaciones ortopédicas como el remplazo de articulaciones, recubrimientos de implantes metálicos y rellenos para pequeñas cavidades óseas [28-30]. Las cerámicas presentan una resistencia a la compresión cercana a la del hueso trabecular y se pueden trasformar fácilmente en estructuras altamente porosas mediante diferentes métodos de manufactura [7].

Por otra parte, las cerámicas bioactivas reaccionan con los fluidos fisiológicos formando una capa de HA en su superficie que genera un enlace químico estable entre la matriz y el tejido óseo circundante (osteointegración) [31,32].

Los CaPs, en particular el HA y el TCP, constituyen las cerámicas más utilizadas como sustitutos óseos. Estas biocerámicas, al presentar una composición muy similar a la fase inorgánica del hueso, son biocompatibles y se integran muy bien con el tejido óseo [5,16]. Además, son excelentes osteoconductores y pueden

ser, según la composición, reabsorbidos a medida que son remplazados por el nuevo tejido.

1.2.2.1. Fosfatos cárnicos

La familia de los CaPs comprende una variedad de compuestos caracterizados por su relación molar Ca/P y su solubilidad. En la Tabla 1 se muestran dichas características para algunos de los principales CaPs. Ahora bien, aquellos con una relación Ca/P ≤ 1 presentan una solubilidad muy alta y se degradan antes de que el tejido nuevo se regenere, por lo que no resultan adecuados para la implantación [33].

Tabla 1: Principales CaPs [33]

Compuesto	Fórmula Química	Ca/P	Solubilidad (mg/L)(37°C)
DCPD	CaHPO ₄ ·2H ₂ O	1.00	74
DCPA	CaHPO ₄	1.00	41
OCP	Ca ₈ H ₂ (PO ₄) ₆ ·5H ₂ O	1.33	0.018
α-TCP	α-Ca ₃ (PO ₄) ₂	1.50	0.24
β-TCP	β- Ca ₃ (PO ₄) ₂	1.50	0.15
HA	Ca ₁₀ (PO ₄) ₆ ·(OH) ₂	1.67	0.000096
TTCP	Ca ₄ O(PO ₄) ₂	2.00	0.39-0.075

Para aplicaciones biomédicas son de particular interés aquellos CaPs con una relación Ca/P entre 1.50 (TCP) - 1.67 (HA). Sin embargo, está demostrado que el HA sintético puede permanecer durante más tiempo en el interior del organismo debido a su cristalinidad y relación Ca/P relativamente altas que retrasan la reabsorción *in vivo* [34,35]. Es por esto que en la práctica clínica se suele utilizar el HA mezclado con TCP (en una relación 60HA/40TCP) para disminuir el tiempo de reabsorción, utilizándose ampliamente en forma de rellenos temporales para el tratamiento de pequeños defectos óseos. Por su parte, el TCP presenta tres polimorfos: uno de baja temperatura (β-TCP) y dos de alta temperatura (α-TCP y α'-TCP). Este último carece de interés práctico

porque sólo existe a temperaturas por encima de $\sim 1465^{\circ}\text{C} \pm 5^{\circ}\text{C}$ y revierte a α -TCP por debajo de la temperatura de transición. Sin embargo, el β -TCP es estable a temperatura ambiente y transforma a α -TCP a $\sim 1115^{\circ}\text{C} \pm 10^{\circ}\text{C}$ [36].

Un aspecto significativo en el desarrollo de las cerámicas a base de CaPs es que algunas sustituciones iónicas y productos de disolución pueden ejercer un control en la expresión de los genes que regulan la osteogénesis, así como estimular la producción de factores de crecimiento [37-39]. En este contexto, está demostrado que las sustituciones de silicio en las estructuras cristalinas de los CaPs mejoran sus propiedades biológicas en comparación con sus homólogos estequiométricos [40,41]. El silicio constituye un elemento esencial en los procesos fisiológicos de renovación del tejido óseo, estimulando la diferenciación osteogénica de las células madre mesenquimales [42] y favoreciendo el proceso de biominerilización [43,44]. Para el caso específico del TCP, se ha demostrado que las sustituciones parciales de grupos PO_4^{3-} por SiO_4^{4-} estabilizan la fase α disminuyendo la temperatura de transición polimórfica de β a α -TCP [45]. En los últimos años se ha mostrado un interés significativo en el desarrollo de cerámicas de Si- α -TCP para mejorar sus propiedades biológicas y mecánicas, así como su tasa de reabsorción [46,47].

Otra alternativa interesante para la mejora de las propiedades biológicas y mecánicas consiste en la fabricación de cerámicas multifásicas a base de CaPs, dado que sus tasas de bioactividad, osteoconductividad y biodegradación pueden adaptarse controlando la relación de las fases presentes [6].

En general, las propiedades de las cerámicas de CaPs pueden variar significativamente en función de la composición química, las fases presentes, la microestructura y la porosidad.

1.3. Diagramas de equilibrio y diseño de cerámicas

Los diagramas de equilibrio constituyen representaciones gráficas de las condiciones mediante las cuales ciertas fases o mezclas de fases existen en un sistema bajo equilibrio termodinámico. La correcta comprensión de los mismos permite predecir las fases presentes y la fracción o porcentaje que representan

dentro del sistema, así como la microestructura resultante en función de la composición química y de las variables de procesado.

Se puede afirmar que un sistema se encuentra en equilibrio termodinámico cuando los potenciales que inducen cambios en sus propiedades químicas, térmicas y mecánicas tienden a cero. Las características de dicho sistema no variarán en el tiempo a menos que se apliquen potenciales energéticos externos capaces de modificar el estado de equilibrio.

El concepto de fase resulta indispensable para comprender los diagramas de equilibrio. Una fase se define como una porción homogénea de un sistema que tiene características físicas y químicas uniformes. Si en un sistema coexisten más de una fase (sistema heterogéneo), existirá un límite definido entre ellas y cada una tendrá sus propias características. La combinación de propiedades de un sistema multifase difiere de las propiedades de las fases individuales y, por lo general, resultan mejoradas.

Como se planteó anteriormente, la composición, las fases presentes y la microestructura influyen significativamente en las propiedades físico-químicas y biológicas de una cerámica. Es por ello que el estudio de los diagramas de equilibrio de fases nos permite comprender el comportamiento de las mismas y aplicar ese conocimiento al diseño de nuevas biocerámicas específicas según las necesidades de cada paciente.

1.3.1. Sistema $2\text{CaO}\cdot\text{SiO}_2 - 3\text{CaO}\cdot\text{P}_2\text{O}_5$

El sistema $2\text{CaO}\cdot\text{SiO}_2 - 3\text{CaO}\cdot\text{P}_2\text{O}_5$ es un sistema binario a presión constante cuyos primeros estudios publicados corresponden a Nurse y col. en el año 1959 [48] y desde entonces ha sido objeto de varias revisiones. En 1969, Fix y col. definen dos compuestos intermedios que funden congruentemente: $7\text{CaO}\cdot\text{P}_2\text{O}_5\cdot2\text{SiO}_2$ (Fase A) y $5\text{CaO}\cdot\text{SiO}_2\cdot\text{P}_2\text{O}_5$ (silicocarnotita) [49]. El diagrama propuesto por Fix y col. se muestra en la Figura 2. El sistema quedó dividido, para su estudio, en tres subsistemas como se muestra a continuación:

- Subsistema $2\text{CaO}\cdot\text{SiO}_2 - 7\text{CaO}\cdot\text{P}_2\text{O}_5\cdot2\text{SiO}_2$ modificado por Rubio y col. donde redefinen el punto invariante eutectoide E1 a $518^\circ\text{C} \pm 6^\circ\text{C}$ con una

composición de 69% en peso de $2\text{CaO}\cdot\text{SiO}_2$ y 31% en peso de $3\text{CaO}\cdot\text{P}_2\text{O}_5$ [50].

- Subsistema $7\text{CaO}\cdot\text{P}_2\text{O}_5\cdot2\text{SiO}_2$ - $5\text{CaO}\cdot\text{SiO}_2\cdot\text{P}_2\text{O}_5$ modificado por Ros-Tárraga y col. donde redefinen el punto invariante eutectoide E2 a $1366^\circ\text{C} \pm 4^\circ\text{C}$ con una composición de 40.5% en peso de $2\text{CaO}\cdot\text{SiO}_2$ y 59.5% en peso de $3\text{CaO}\cdot\text{P}_2\text{O}_5$ [51].
- Subsistema $5\text{CaO}\cdot\text{SiO}_2\cdot\text{P}_2\text{O}_5$ - $3\text{CaO}\cdot\text{P}_2\text{O}_5$ modificado por Martínez y col. donde redefinen el punto invariante eutectoide E3 a $1158^\circ\text{C} \pm 2^\circ\text{C}$ con una composición de 17% en peso de $2\text{CaO}\cdot\text{SiO}_2$ y 83% en peso de $3\text{CaO}\cdot\text{P}_2\text{O}_5$ [52].

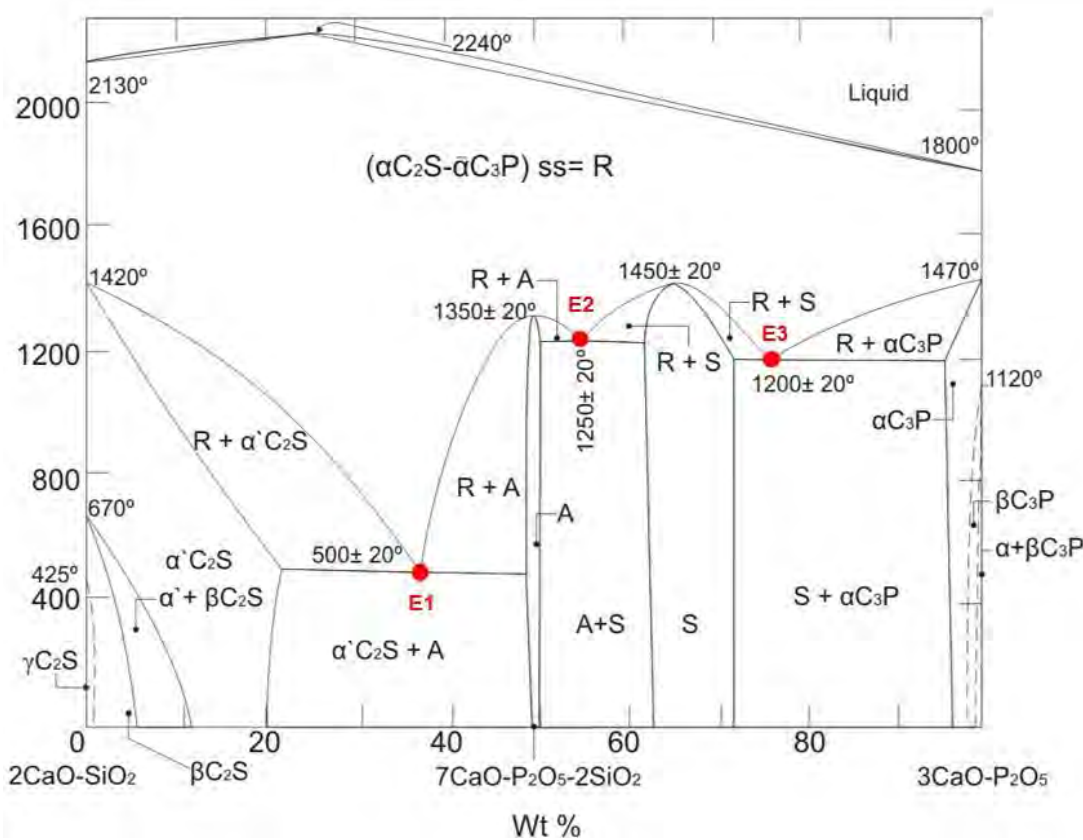


Figura 2: Sistema $2\text{CaO}\cdot\text{SiO}_2$ - $3\text{CaO}\cdot\text{P}_2\text{O}_5$, diagrama propuesto por Fix y col. [49].

Se entiende por punto invariante eutectoide aquel en el que, a una temperatura determinada, una fase sólida de alta temperatura transforma a dos fases sólidas de baja temperatura. A la reacción que tiene lugar se le conoce como reacción eutectoide.

La presente Tesis Doctoral se enmarca en el desarrollo de matrices 3D con una composición eutectoide E3 del subsistema $5\text{CaO}\cdot\text{SiO}_2\cdot\text{P}_2\text{O}_5$ - $3\text{CaO}\cdot\text{P}_2\text{O}_5$ (Figura 3), correspondiente con silicocarnotita (53.4% en peso) y α -TCP (46.6% en peso).

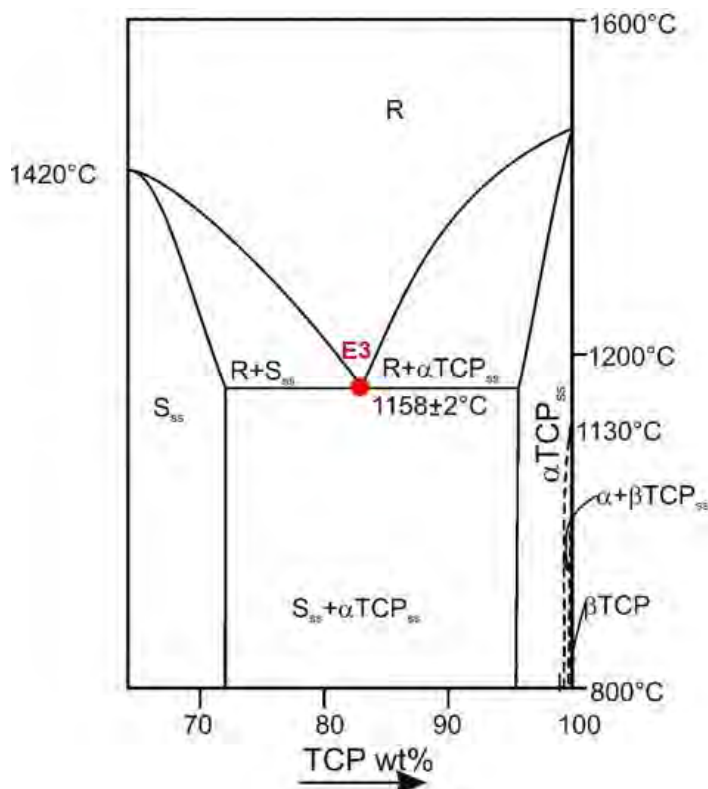


Figura 3: Subsistema $5\text{CaO}\cdot\text{SiO}_2\cdot\text{P}_2\text{O}_5$ - $3\text{CaO}\cdot\text{P}_2\text{O}_5$ modificado, Martínez y col. [52].

Las ventajas del α -TCP para aplicaciones en ITO se han expuesto en la sección anterior. Por su parte, la silicocarnotita constituye un silicofosfato de calcio con estructura de carnotita [53] y está considerada como un polimorfo del HA con un alto grado de sustituciones de grupos SiO_4^{4-} [54]. A pesar de no estar muy difundido su uso en aplicaciones para ITO, en los últimos años la silicocarnotita ha ganado protagonismo debido a su excelente bioactividad [55]. También está demostrado que presenta una biocompatibilidad, biodegradabilidad y osteoconductividad superior a las cerámicas de HA estequiométrico [56].

2. Objetivos

Las cerámicas con composiciones dentro del sistema $2\text{CaO}\cdot\text{SiO}_2$ - $3\text{CaO}\cdot\text{P}_2\text{O}_5$ constituyen excelentes candidatas para el desarrollo de nuevos biomateriales. El **objetivo principal** de esta Tesis Doctoral es obtener y caracterizar matrices 3D cerámicas con una composición eutectoide (17% en peso de $2\text{CaO}\cdot\text{SiO}_2$ - 83% en peso de $3\text{CaO}\cdot\text{P}_2\text{O}_5$) correspondiente al punto invariante del subsistema $5\text{CaO}\cdot\text{SiO}_2\cdot\text{P}_2\text{O}_5$ - $3\text{CaO}\cdot\text{P}_2\text{O}_5$, con la intención de que las mismas puedan ser aplicadas al diseño de nuevos biomateriales para ITO. Para ello se establecen los siguientes objetivos específicos:

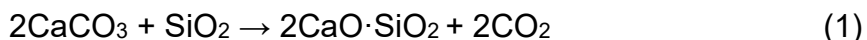
- Sintetizar polvos cerámicos por reacción en estado sólido con una composición correspondiente al punto invariante eutectoide en el subsistema $5\text{CaO}\cdot\text{SiO}_2\cdot\text{P}_2\text{O}_5$ - $3\text{CaO}\cdot\text{P}_2\text{O}_5$.
- Obtener matrices 3D cerámicas mediante el método de réplica sobre esponja polimérica.
- Optimizar el diseño de las matrices mediante la modificación de las variables de procesado.
- Caracterizar las matrices obtenidas desde el punto de vista mineralógico, físico-químico y macro-/micro-/nano- estructural.
- Evaluar la bioactividad *in vitro* de las matrices en SBF de acuerdo con la norma ISO/FDIS 23317. Análisis de los procesos de disolución/precipitación en la interfase de reacción en función del tiempo de inmersión. Determinación del mecanismo de reacción.
- Evaluar la biocompatibilidad mediante ensayos de adhesión y proliferación de ah-MSCs *in vitro*.
- Funcionalizar las matrices 3D con un modelo de proteína *in vitro*.
- Estudio micro-/nano-estructural comparativo entre las matrices 3D y hueso trabecular natural.

3. Materiales y Métodos

3.1. Síntesis de los polvos cerámicos

Los materiales en polvo cerámico para la conformación de las matrices 3D, se sintetizaron por reacción en estado sólido.

La composición 17% en peso de $2\text{CaO}\cdot\text{SiO}_2$ y 83% en peso de $3\text{CaO}\cdot\text{P}_2\text{O}_5$, correspondiente al punto invariante eutectoide, se obtuvo a partir de la síntesis previa de $2\text{CaO}\cdot\text{SiO}_2$ y $3\text{CaO}\cdot\text{P}_2\text{O}_5$ mediante la mezcla estequiométrica de los reactivos comerciales: hidrógeno fosfato de calcio (CaHPO_4) (Panreac, Castellar del Vallés, Spain), carbonato cálcico (CaCO_3) (>99 wt% Fluka, St. Louis, MO), y dióxido de silicio (SiO_2) (>99.7 wt% Strem Chemica, Inc., Newburyport, MA, USA), de acuerdo con la ecuaciones 1 y 2. Las condiciones del procesado se especifican en la sección 2.1 “*Ceramic synthesis*” del Artículo 1 (pg. 56).



El tratamiento térmico de síntesis de los polvos cerámicos y la reducción del tamaño de partícula necesario para la aplicación del método de réplica sobre esponja polimérica, se especifican en la sección 2.1 “*Ceramic synthesis*” del Artículo 1 (pg. 56).

3.2. Caracterización de los polvos cerámicos

La caracterización mineralógica de los polvos cerámicos se realizó por XRD, la distribución del tamaño de partícula por difracción láser y el análisis morfológico por SEM. Las condiciones para cada caracterización se especifican en la sección 2.2 “*Characterization of raw material*” del Artículo 1 (pg. 56).

3.3. Obtención de las matrices 3D cerámicas

Para la obtención de las matrices 3D cerámicas se utilizó el método de réplica sobre esponja polimérica. Este método resulta muy práctico ya que es aplicable a cualquier material cerámico que pueda ser completamente dispersado en una suspensión. La réplica de esponja polimérica permite obtener estructuras

cerámicas altamente porosas con tamaños de poros heterogéneos y elevada interconexión.

Para la conformación de las matrices se utilizaron tres prototipos de plantillas de poliuretano (25, 30 y 40 ppi) y suspensiones de los polvos cerámicos previamente sintetizados.

Las características de las plantillas, la preparación de las barbotinas, el proceso de impregnación, así como los tratamientos térmicos para la sinterización de las matrices cerámicas se especifican en las secciones: 2.3 “*Preparing scaffolds by the polymer replica method*” del Artículo 1 (pg. 56), 2.2. “*Synthesis of porous scaffolds*” del Artículo 2 (pg. 67), 2. “*Materials and Methods*” del Artículo 3 (pg. 76) y 2.1. “*Ceramic Scaffolds Synthesis*” del Artículo 4 (pg. 83).

3.4. Caracterización de las matrices 3D

La caracterización mineralógica de las matrices cerámicas se realizó por XRD. Por su parte, el análisis de la composición y los enlaces químicos presentes se llevó a cabo por EDS, ATR-FTIR y espectroscopía Raman. Las condiciones para la caracterización mineralógica y química se encuentran descritas en las secciones: 2.4 “*Scaffolds Characterization*” del Artículo 1 (pg. 56), 2.3. “*Scaffolds characterization*” del Artículo 2 (pg. 67), 2. “*Materials and Methods*” del Artículo 3 (pg. 76) y 2.2. “*Scaffolds Characterization*” del Artículo 4 (pg. 83).

La caracterización macro-/micro-/nano-estructural de las matrices 3D se realizó mediante porosimetría de mercurio, SEM y TEM. La resistencia mecánica se evaluó bajo compresión mediante la aplicación de una fuerza axial constante hasta la fractura de las matrices. Las especificaciones de cada técnica se encuentran descritas en las secciones: 2.4 “*Scaffolds Characterization*” del Artículo 1 (pg. 59), 2.3. “*Scaffolds characterization*” del Artículo 2 (pg. 67), 2. “*Materials and Methods*” del Artículo 3 (pg. 76) y 2.2. “*Scaffolds Characterization*” del Artículo 4 (pg. 83).

3.5. Ensayos de bioactividad *in vitro*

La bioactividad de un material puede ser evaluada *in vitro* a través de su capacidad de formar HA al ser expuesto a SBF con una concentración iónica

similar a la del plasma sanguíneo humano. Los ensayos de bioactividad para las matrices 3D cerámicas se realizaron siguiendo las pautas establecidas por Kokubo y Takadama [57], contenidas en la norma ISO/FDIS 23317 [58].

Las matrices se sumergieron en SBF a diferentes tiempos (1, 3, 7, 14 y 21 días), tras los cuales se analizaron los cambios morfológicos y químicos ocurridos en las estructuras, así como las variaciones en las concentraciones iónicas del SBF. Los cambios morfológicos se analizaron por SEM y TEM-SAD, mientras que los químicos se evaluaron mediante EDS y ATR-FTIR. Las variaciones en las concentraciones iónicas del SBF se determinaron por ICP-OES.

Las condiciones para los ensayos de bioactividad, los tiempos de inmersión y las especificaciones para cada técnica de caracterización se encuentran descritos en las secciones: 2.4. “*In vitro bioactivity test*” del Artículo 2 (pg. 67) y 2. “*Materials and Methods*” del Artículo 3 (pg. 79).

3.6. Ensayos de biocompatibilidad *in vitro*

La biocompatibilidad se evaluó *in vitro* en términos de la capacidad de adhesión y proliferación de ah-MSCs sobre las matrices 3D cerámicas.

Las ah-MSCs se sembraron sobre las matrices y se incubaron a distintos tiempos (7, 14, 21 y 28 días) en dos medios de cultivo diferentes (GM y OM). Tras cada tiempo de incubación se estudiaron los principales cambios morfológicos a nivel celular y de superficie por SEM y TEM-SAD.

La actividad metabólica de las ah-MSCs se evaluó mediante el ensayo de viabilidad AB. Este ensayo se ha utilizado ampliamente para evaluar la citotoxicidad y viabilidad en diferentes líneas celulares frente a diferentes fármacos y materiales [59]. El componente activo del ensayo AB es la resazurina, compuesto azul no fluorescente, estable en medio de cultivo y no tóxico. En ambientes donde las células son metabólicamente activas la resazurina se reduce químicamente a resorufina, compuesto de color rosa altamente fluorescente. La fluorescencia resultante de cada ensayo es entonces proporcional a la actividad metabólica y al crecimiento celular.

La influencia de los productos de disolución de las matrices en una posible diferenciación osteogénica de las ah-MSCs se estimó mediante la monitorización de la actividad de la ALP en células cultivadas en contacto indirecto con las cerámicas. Como se mencionó anteriormente, dicha enzima es un marcador temprano de diferenciación osteogénica. La actividad de la ALP a diferentes tiempos de cultivo se evaluó mediante la reacción con el sustrato PNPP. En condiciones óptimas, la ALP hidroliza al PNPP para dar como resultado PNP, compuesto que se caracteriza por un color amarillo. La cantidad de PNP resultante es proporcional a la actividad de la ALP y puede cuantificarse mediante técnicas de espectroscopía.

La Figura 4 muestra un esquema de la configuración de los ensayos celulares *in vitro*. Se representan los tiempos de análisis (7, 14, 21 y 28 días), los medios de cultivo (GM y OM) y las técnicas de caracterización utilizadas en cada tiempo para una mejor comprensión.

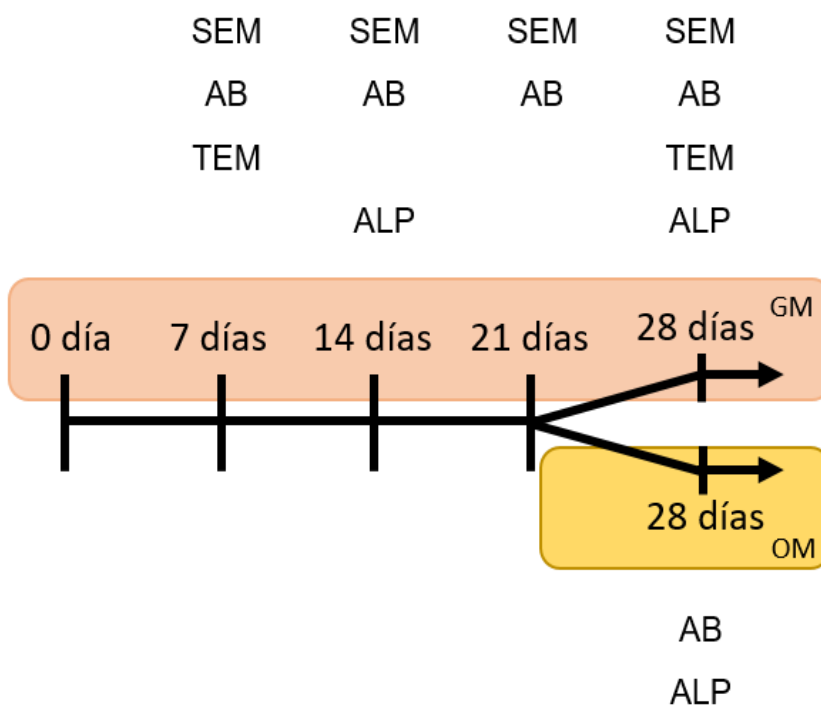


Figura 4: Esquema de la configuración de los ensayos celulares *in vitro*.

El aislamiento, la expansión y caracterización de las células utilizadas para cada ensayo quedan descritos en las secciones: 2.5. “*The ah-MSCs: isolation,*

expansion and characterization" del Artículo 2 (pg. 67) y 2.4. "Ah-MSCs: Isolation, Expansion and Characterization" del Artículo 4 (pg. 84).

Las condiciones de cultivo, los tiempos de análisis y las técnicas de caracterización utilizadas quedan descritas en las secciones: 2.6 "*In vitro cell test*" del Artículo 2 (pg. 67), 2.5. "Ah-MSCs Adhesion and Proliferation In Vitro Test" del Artículo 4 (pg. 84) y 2.6. "Testing Alkaline Phosphatase Specific Activity in Cells" del Artículo 4 (pg. 85).

3.7. Funcionalización con fosfatasa alcalina

Se evaluó la capacidad de funcionalización de las matrices 3D con la enzima ALP *in vitro*. Se eligió este modelo de proteína por ser la ALP una enzima que juega un papel fundamental en los procesos de formación y mineralización del tejido óseo, proporcionando un entorno local enriquecido en iones Ca²⁺ y grupos PO₄³⁻ [60]. Además, estudios previos han demostrado alcanzar una correcta funcionalización de vidrios y cerámicas bioactivas con dicha enzima [61]. Una correcta funcionalización con ALP permitiría mejorar las propiedades biológicas de las matrices.

El procedimiento para la funcionalización de las matrices con la ALP y el test de actividad enzimática se encuentran descritos en las secciones: 2.7. "Alkaline Phosphatase Grafting to Scaffolds" del Artículo 4 (pg. 85). y 2.8. "Enzymatic Activity Test" del Artículo 4 (pg. 85).

3.8. Estudio comparativo con hueso trabecular

Se realizó un estudio comparativo mediante SEM entre las matrices 3D obtenidas y hueso trabecular natural de cerdo adulto para evaluar las similitudes estructurales entre ambos. Los procedimientos para la obtención y preparación de las muestras de hueso natural se especifican en la sección: 2.3. "SEM Examination of Natural Cancellous Bone" del Artículo 4 (pg. 84).

Todos los ensayos de biocompatibilidad se realizaron de acuerdo con las directrices de la Declaración de Helsinki y fueron aprobados por el Comité de Ética de la Universidad Católica San Antonio de Murcia (Referencia CE051904).

4. Resultados

4.1. Caracterización de los polvos cerámicos

El análisis XRD de los polvos cerámicos evidenció que todos los picos de difracción se correspondían con las fases cristalinas de: silicocarnotita (JCPDS card No. 73-1181) y α -TCP (JCPDS card No. 09-0348), ver Figura 1 del Artículo 1 (pg. 57).

Los polvos cerámicos de composición eutectoide se molieron en molino planetario a varios intervalos (de 30 minutos a 4 horas) con el fin de seleccionar el tiempo de molienda que proporcionara la distribución de tamaño de partícula más pequeña y homogénea. También se caracterizaron por XRD para identificar una posible amorfización debida al proceso de molienda. Los datos para el análisis del tamaño de partícula y los XRD para cada tiempo de molienda se muestran en la Figura 2A y 2B del Artículo 1 (pg. 57).

El tiempo óptimo de molienda fue 1.5 horas ya que presentó la distribución de tamaño de partícula más fina y homogénea con 12 μm de media. No se observaron diferencias significativas en las fases cristalinas y en el grado de cristalinidad de los polvos cerámicos, por lo que no ocurrió amorfización durante los procesos de molienda.

El análisis SEM de la morfología de los polvos para los diferentes tiempos de molienda mostró una distribución de partículas irregulares aglomeradas, como se puede observar en la Figura 3 del Artículo 1 (pg. 58).

4.2. Obtención y caracterización de las matrices 3D

En la Figura 4A y 4B del Artículo 1 (pg. 58) se muestran imágenes representativas de dos de las plantillas utilizadas para la conformación de las matrices: 40 ppi y 25 ppi. Después de la impregnación con la barbotina y del correspondiente tratamiento térmico se consolidaron las matrices cerámicas como se puede observar en la Figura 4C y 4E del Artículo 1 (pg. 61).

En el análisis XRD de las matrices obtenidas no se observaron fases adicionales en comparación con los polvos cerámicos de partida, como se muestra en la

Figura 1 del Artículo 2 (pg. 68), lo que confirmó que no ocurrieron cambios mineralógicos durante el proceso de conformación de las matrices. Se identificaron dos fases: silicocarnotita (53.6% en peso) (COD no. 00-073-1181) y α -TCP (46.4% en peso) (COD no. 96-210-6195). El análisis por Rietveld confirmó la obtención de una composición mineralógica de silicocarnotita (53.6% en peso) y α -TCP (46.4% en peso), muy próxima al punto invariante E3 del subsistema $5\text{CaO}\cdot\text{SiO}_2\cdot\text{P}_2\text{O}_5 - 3\text{CaO}\cdot\text{P}_2\text{O}_5$ (53.4/46.6), ver Figura 2 del Artículo 3 (pg. 77).

El estudio por ATR-FTIR mostró que las principales bandas de absorción de las matrices ($1200\text{-}500\text{ cm}^{-1}$) se correspondieron con grupos SiO_4^{4-} y PO_4^{3-} , ver Figura 7 del Artículo 1 (pg. 60). Con fines comparativos, se analizaron los espectros ATR-FTIR de dos cerámicas monofásicas de silicocarnotita y α -TCP.

El análisis por espectroscopía Raman también mostró intensidades (400-1200 cm^{-1}) correspondientes con grupos SiO_4^{4-} y PO_4^{3-} , ver Figura 4 del Artículo 4 (pg. 88). Al igual que en el caso anterior, se analizaron los espectros Raman de las cerámicas monofásicas.

El análisis SEM de la microestructura de las matrices reveló, en todos los casos, un alto grado de porosidad (83-96%) e interconexión entre poros (120-1500 μm), como se muestra en la Figura 5 del Artículo 1 (pg. 62), Figura 2 del Artículo 2 (pg. 69) y Figuras 1A y 1B del Artículo 4 (pg. 86). Las estructuras densificaron correctamente conservando cierto grado de microporosidad sobre las superficies (5-10 μm), ver Figuras 5E y 5F del Artículo 1 (pg. 59), a pesar de la contracción (30-34%) producida durante la sinterización de las matrices. Las medidas realizadas por SEM y la porosimetría de mercurio mostraron una distribución heterogénea del tamaño de los poros, ver Tabla 1, Tabla 2 y Figura 6 del Artículo 1 (pg. 59-60).

El análisis por TEM mostró una nanoestructura irregular eutectoide en forma de lamelas alternas, distribuida uniformemente en la estructura de las matrices, como se muestra en la Figura 2 del Artículo 4 (pg. 87). El microanálisis EDS mostró una fase rica en silicio y una en fosfato de calcio, que se correspondieron con silicocarnotita y α -TCP respectivamente. Ambas fases se observaron compactas y densas sin regiones intermedias entre ellas.

Después del ataque químico con ácido acético (1%) durante 4 segundos para revelar la nanoestructura, el análisis SEM y el microanálisis EDS de las lamelas resultantes indicaron la presencia de calcio, fósforo y silicio en una proporción variable $1.34 < \text{Ca} / (\text{P} + \text{Si}) < 1.88$. En promedio, este valor se acercó al de la silicocarnotita estequiométrica ($\text{Ca} / (\text{P} + \text{Si}) = 1.66$) lo que confirmó que la fase eliminada por ataque químico fue la α -TCP, ver Figura 8 del Artículo 1 (pg. 61).

El grosor de las lamelas (100-940 nm) se pudo controlar variando la velocidad de enfriamiento (50°C/h, 16.5°C/h, 5.5°C/h) a través de la temperatura eutectoide durante el tratamiento térmico para la conformación de las matrices, como se muestra en la Figura 3 del Artículo 4 (pg. 88). También fue posible controlar la resistencia a la compresión (0.62-3.38 MPa) por esta vía, ver Tabla 1 del Artículo 4 (pg. 86).

4.3. Ensayos de bioactividad *in vitro*

Los ensayos de bioactividad *in vitro* mostraron cambios morfológicos y químicos importantes en las matrices 3D.

Tras 1 día de inmersión en SBF se detectó la presencia de una nanoestructura en forma de lamelas alternas en las matrices, que se reveló completamente tras los 3 días de inmersión, ver Figuras 3D y 3F del Artículo 3 (pg. 77). El microanálisis EDS de las lamelas determinó una relación Ca/P promedio de 1.62 sin trazas de silicio.

El análisis SEM mostró la formación de un precipitado de partículas globulares ($\leq 5\mu\text{m}$) tipo apatito sobre la nanoestructura en lamelas previamente transformada entre los 3 y 7 días de inmersión, ver Figuras 3E y 3F del Artículo 2 (pg. 69). En algunas áreas dicho precipitado se introdujo en los espacios entre lamelas como señalan las flechas en la Figura 4B del Artículo 3 (pg. 78). El microanálisis EDS determinó que las partículas globulares presentaron una relación Ca/P entre 1.47-1.53 con pequeñas cantidades de silicio, ver Tabla 2 del Artículo 3 (pg. 78).

El precipitado tipo apatito creció gradualmente con el tiempo de inmersión hasta formar una capa densa y compacta sobre las superficies de las matrices tras 14 y 21 días de inmersión en SBF, ver Figuras 3G y 3H del Artículo 2 (pg. 69) y

Figuras 4D, 4E y 5 del Artículo 3 (pg. 78). En algunas áreas la capa de precipitado era tan gruesa que se desprendió debido a su peso, esto reveló la presencia de una nanoestructura en lamelas bajo dicha capa como se muestra en las Figuras 4C, 4D y 5 del Artículo 3 (pg. 78). El microanálisis EDS indicó una pequeña sustitución de silicio en la capa precipitada, que a su vez presentó una relación Ca/P entre 1.47-1.55.

La ultraestructura del precipitado, tras diferentes tiempos de inmersión en SBF (3, 7, 21 días), se analizó por TEM-SAD. La Figura 7 del Artículo 2 (pg. 71) muestra las micrografías obtenidas para cada tiempo. En general se observó la evolución y formación de una fase continua en forma de pequeños cristales individuales. Tras 3 días de inmersión, el patrón SAD indicó una orientación preferencial de los cristales en (002) y (211) similar al apatito biológico [62,63], ver Figura 7B del Artículo 2 (pg. 71). Sin embargo aún son visibles algunos puntos de difracción correspondientes al material cristalino inicial de las matrices. Con el aumento del tiempo de inmersión en SBF los arcos correspondientes a (002) y (211) se definieron cada vez más y el material cristalino inicial ya no fue detectable, ver Figuras 7D y 7F del Artículo 2 (pg. 71).

La capa de precipitado tras 21 días de inmersión en SBF se analizó por ATR-FTIR. Se tomaron dos muestras diferentes, una de la parte superior y otra en el centro de las matrices, para confirmar la presencia en toda la estructura. Los espectros obtenidos se muestran en la Figura 5 del Artículo 2 (pg. 70), también se incluye el espectro de las matrices sin sumergir en SBF con fines comparativos. Tras 21 días de inmersión las matrices muestran diferencias en los espectros con respecto al material sin sumergir en SBF. Los principales cambios son: la pérdida de los picos de absorción correspondientes con grupos SiO_4^{4-} (838 y 870 cm^{-1}), la aparición de picos y bandas característicos de grupos CO_3^{2-} (867 , 866 , 1400 - 1640 , 2907 y 2913 cm^{-1}) y la formación de bandas anchas de absorción a números de onda mayores que se asociaron con grupos OH^- ($\sim 3400\text{ cm}^{-1}$). También se observaron picos de absorción correspondientes a grupos PO_4^{3-} (943 , 938 , 1014 y 1016 cm^{-1}).

Las bandas de absorción de grupos CO_3^{2-} de 1400-1640 cm^{-1} y 2900 cm^{-1} , así como las de grupos PO_4^{3-} de 943 y 938 cm^{-1} , están muy relacionadas con las estructuras de HA carbonatado [64-66].

Las variaciones en las concentraciones iónicas del SBF se determinaron por ICP-OES. En la Figura 6 del Artículo 2 (pg. 71) y la Figura 6 del Artículo 3 (pg. 79) se muestran las variaciones para las concentraciones de calcio, fósforo y silicio. Después de 1 día de inmersión, los iones calcio y silicio aumentaron significativamente en el SBF debido a la disolución de las matrices, lo que indicó que la fase disuelta era rica en silicio. A partir de los 3 días, una vez que comenzaba a formarse el precipitado tipo apatito sobre las matrices, la concentración de iones calcio disminuyó continuamente hasta los 21 días. En consecuencia, la concentración de iones fósforo también disminuyó de forma continua en el SBF durante todo el ensayo. Por otra parte, la concentración de iones silicio alcanzó su máximo tras los 14 días. Posteriormente, a los 21 días, se observó que la concentración de silicio disminuyó con respecto a los 14 días. Esto se relacionó con que una parte de los iones silicio del SBF se incorporaron al nuevo precipitado tipo apatito sobre la superficie de las matrices.

El análisis de los procesos de disolución/precipitación en la interfase de reacción matriz-SBF en función del tiempo de inmersión se encuentra detallado en el Artículo 3 (pg. 75).

4.4. Ensayos de biocompatibilidad *in vitro*

Los ensayos de biocompatibilidad *in vitro* mostraron que las ah-MSCs fueron capaces de adherirse y proliferar sobre las matrices formando una densa capa tras 21 y 28 días de cultivo.

La Figura 8 del Artículo 2 (pg. 72) y la Figura 5 del Artículo 4 (pg. 89) muestran micrografías del estudio por SEM de la evolución de las ah-MSCs para los diferentes tiempos de cultivo en GM (7, 14, 21 y 28 días).

Tras 7 días se observaron células individuales adheridas a las matrices mediante extensas proyecciones citoplasmáticas, ver las Figuras 8A-8C del Artículo 2 (pg. 72) y las Figuras 5A y 5B del Artículo 4 (pg. 89). También se observó la presencia

de un precipitado globular tipo apatito que se formó en estrecho contacto con las células.

Después de 14 días de incubación, las células establecieron un contacto físico estrecho entre ellas y con las matrices a través de numerosas proyecciones citoplasmáticas, ver Figuras 8D-8F del Artículo 2 (pg. 72) y las Figuras 5C y 5D del Artículo 4 (pg. 89). Se observó la presencia de grupos de células sobre toda la estructura de las matrices, incluso en el tercer nivel de poros hacia el interior de las mismas, como muestra la flecha en la Figura 8D del Artículo 2 (pg. 72). A este tiempo, algunas áreas de las matrices aun libres de células presentaron una morfología en forma de lamelas alternas, como resalta el círculo en la Figura 5C del Artículo 4 (pg. 89). Por último, el precipitado tipo apatito se extendió formando una estructura capa a capa con las células, ver Figuras 5D y 5E del Artículo 4 (pg. 89).

Tras aumentar los tiempos de incubación a 21 y 28 días, la monocapa de células y el precipitado tipo apatito se extendieron formando una capa densa sobre las matrices, ver Figuras 8G-8I del Artículo 2 (pg. 72) y las Figuras 5H-5J del Artículo 4 (pg. 89). La formación de nanofibras tipo colágeno con depósitos minerales de Ca-P, sugirió la formación de matriz extracelular por parte de las células.

Después de 28 días de incubación en GM se identificaron en las matrices tres estructuras consecutivas bien definidas, ver Figura 6C del Artículo 4 (pg. 90):

- Una densa capa de precipitado tipo apatito, cuyo microanálisis EDS indicó una pequeña sustitución de silicio y una relación Ca/P promedio de 1.55.
- Una nanoestructura en lamelas bajo la capa de precipitado, cuyo microanálisis EDS no mostró trazas de silicio y presentó una relación Ca/P promedio de 1.98.
- El material original de las matrices en el interior de la estructura, cuyo microanálisis EDS indicó un mayor contenido de silicio que en el precipitado tipo apatito y una relación Ca/P promedio de 1.64.

La ultraestructura del precipitado tipo apatito, tras diferentes tiempos de incubación en GM (7 y 28 días), se analizó por TEM-SAD. La Figura 7 del Artículo 4 (pg. 91) muestra las micrografías obtenidas para cada tiempo. En general se observó el crecimiento y evolución de cristales que se fusionaron para formar

una capa homogénea con morfología de HA. Los microanálisis EDS confirmaron la presencia de silicio en dicha capa y una relación Ca/P promedio de 1.55.

Por otra parte, la actividad metabólica de las ah-MSCs se monitorizó mediante ensayos de AB. Los resultados de dichos ensayos confirmaron la correcta actividad metabólica y proliferación de las células en las matrices 3D. La Figura 9 del Artículo 2 (pg. 72) y la Figura 8 del Artículo 4 (pg. 92) muestran los resultados de los ensayos de AB sobre las ah-MSCs sembradas en las matrices 3D y en las placas de cultivo 2D (control positivo), para diferentes tiempos de incubación (7,14, 21, 28 días) y medios de cultivo (GM y OM). La actividad metabólica de las células sembradas en las matrices progresó linealmente con el tiempo hasta el final de los ensayos y su valor superó al del control después de 21 y 28 días de cultivo.

Finalmente, una posible diferenciación de las ah-MSCs, inducida por los productos de disolución de las matrices, se estimó en términos de la actividad de la ALP de las células cultivadas en contacto indirecto con las matrices y en el control positivo tras diferentes tiempos de incubación (14 y 28 días) y medios de cultivo (GM y OM). La Figura 9 del Artículo 4 (pg. 92) muestra la cuantificación de la actividad de la ALP para cada test. A los 14 días en GM, la actividad de la ALP fue baja y no se detectaron diferencias significativas entre las células en contacto indirecto con las matrices y el control. Al aumentar el tiempo de incubación a 28 días, tanto en GM como en OM, la actividad de la ALP en las células en contacto indirecto con las matrices fue significativamente superior que en el control.

4.5. Funcionalización con fosfatasa alcalina

La correcta funcionalización de las matrices 3D con la ALP se evaluó midiendo la actividad específica de la enzima por inmersión de las matrices funcionalizadas en una solución de PNPP (50 μ M) a diferentes días (7,14 y 21). La Figura 10 del Artículo 4 (pg. 93) muestra los resultados de la cuantificación de la actividad de la ALP para cada ensayo. Aunque la actividad enzimática aumentó con el tiempo de reacción para cada día, esta disminuyó de un ensayo a otro. Lo que indicó que la estabilidad de unión entre la ALP y las matrices se pudo ver afectada por los procesos de lavado entre un ensayo y otro.

No obstante, la presencia de actividad enzimática en todos los casos indicó que la ALP se incorporó a las matrices 3D manteniendo su estado activo tras 21 días de funcionalización.

4.6. Estudio comparativo con hueso trabecular

El análisis por SEM de la microestructura del hueso trabecular natural de cerdo adulto mostró una porosidad altamente interconectada (86-88%) con distribuciones de tamaño de poro heterogéneas (100-700 μm), ver Figura 1D-1F del Artículo 4 (pg. 86). El microanálisis EDS confirmó una relación Ca/P entre 1.50-1.60.

La nanotopografía de las superficies del hueso trabecular natural mostró una morfología en forma de lamelas alternas orientadas al azar. Esto se corresponde con el patrón de los haces de fibras de colágeno previamente removidos por el proceso de limpieza de las muestras. La micro-/nano-estructura de las matrices 3D cerámicas obtenidas se acerca a la micro-/nano-estructura del hueso trabecular natural examinado, tal y como se puede observar en la Figura 1A-1F del Artículo 4 (pg. 86).

5. Discusión

En los últimos años, las investigaciones en biomateriales con aplicaciones en ITO han aumentado significativamente. Las líneas actuales de desarrollo de nuevas matrices 3D buscan proporcionar un entorno de soporte similar al hueso natural para la correcta regeneración del tejido [7,9]. Por tanto, una matriz 3D para ITO no solo debe imitar la composición química y estructura jerárquica del hueso natural, sino que también debe considerar la biología celular y molecular.

En la presente Tesis Doctoral se desarrollaron matrices 3D bifásicas de silicocarnotita y α -TCP que imitaron la composición química y la macro-/micro-/nano-estructura del hueso trabecular natural, así como el proceso de mineralización que tiene lugar a través de la nucleación y crecimiento de cristales de HA. Las mismas proporcionaron un entorno favorable *in vitro* para el desarrollo de las ah-MSCs y la actividad de la enzima ALP.

Las matrices 3D se obtuvieron mediante el método de réplica sobre esponja polimérica, a partir de una barbotina de polvos cerámicos con composición eutectoide muy cercana al punto invariante E3 (Figura 3) del subsistema Silicocarnotita – α -TCP.

Los polvos utilizados para la preparación de la barbotina se sintetizaron por reacción en estado sólido. A continuación, se molieron en molino planetario para obtener un tamaño de partícula lo más fino posible y facilitar así la total impregnación de las plantillas de poliuretano. Algunos autores sugieren que la reducción mecánica del tamaño de partícula de los polvos de TCP afecta el grado de cristalinidad del mismo [67]. Sin embargo, el análisis por XRD de los polvos cerámicos a diferentes tiempos de molienda no mostró diferencias significativas en el grado de cristalinidad de sus fases constituyentes: silicocarnotita y α -TCP (Figura 2B del Artículo 1 (pg. 57)).

El uso del método de réplica sobre esponja polimérica permitió obtener estructuras altamente porosas, con tamaños de poros heterogéneos y elevada interconexión entre ellos (Figura 4C y 4E del Artículo 1 (pg. 58)), así como controlar las características de la red de poros y la geometría en función de la

plantilla de poliuretano seleccionada [68]. Esto facilita el diseño de matrices 3D ajustables a los requerimientos de cada defecto óseo.

Del estudio de la macro-/micro-estructura se obtuvieron varios resultados destacables. Los valores de porosidad obtenidos en todos los casos (83-96%) se acercaron a los valores de porosidad reportados para el hueso trabecular natural (50-90%) [10] y a los obtenidos para el hueso trabecular de cerdo adulto analizado (86-88%). El estudio por SEM mostró valores de diámetros de puentes en las matrices (70-310 μm) muy similares a los valores de diámetros de trabéculas para el hueso natural (50-300 μm) [10].

Los análisis por SEM y porosimetría de mercurio confirmaron una distribución de tamaño de poro heterogénea (1-1500 μm) (Figura 5, Tabla 1, Figura 6 y Tabla 2 del Artículo 1 (pg. 59-60)). Aunque existen algunas discrepancias en cuanto a si es necesaria o no una distribución heterogénea del tamaño de los poros [69-71], están bien establecidas por la literatura las funciones que desempeña cada tipo de poro en el proceso de regeneración del tejido óseo. Los poros inferiores a 10 μm proporcionan mayor área superficial, lo que favorece el intercambio iónico con el medio, la precipitación de apatito biológico y la adsorción de proteínas [72]. Por otra parte, los poros entre 100-150 μm favorecen la adhesión, proliferación y migración de las células en las matrices [73,74]. Finalmente, los poros mayores de 300 μm son necesarios para permitir la correcta vascularización y el crecimiento interno del nuevo tejido (osteoconducción) [75]. Por todo esto, podemos concluir que una distribución heterogénea de tamaños de poro consideraría, a la vez, todos los factores necesarios para la correcta regeneración del tejido óseo.

El análisis detallado de la nanoestructura de las matrices por SEM y TEM, mostró una organización en forma de lamelas alternas de silicocarnotita y α -TCP. No se observaron defectos en la interfase entre lamelas, ni la presencia de fases intermedias (Figura 2 del Artículo 4 (pg. 87)). Fue posible controlar el grosor de las lamelas variando la velocidad de enfriamiento a través de la temperatura eutectoide durante el tratamiento térmico de conformación de las matrices. Esto se debió a la estrecha relación que existe entre la velocidad de enfriamiento y la forma en que ocurre la nucleación y crecimiento de las lamelas [76].

También fue posible controlar la resistencia a la compresión axial de las matrices variando la velocidad de enfriamiento a través de la temperatura eutectoide. La resistencia a la compresión aumentó a medida que disminuyó la velocidad de enfriamiento. Se ha demostrado que la evolución de la nanoestructura durante el proceso de sinterización tiene un efecto significativo sobre el comportamiento mecánico de algunas cerámicas de CaPs sustituidas con silicio [77]. Las velocidades de enfriamiento más bajas proporcionan más tiempo para la consolidación de la nanoestructura y reducen la aparición de grietas debidas a la contracción térmica brusca [78].

Los ensayos de bioactividad *in vitro* mostraron que las matrices 3D presentaron un fuerte comportamiento bioactivo y de degradabilidad en SBF. Las mismas reaccionaron provocando la disolución selectiva de una de sus fases y la posterior transformación pseudomórfica de la fase restante.

Las variaciones en las concentraciones iónicas en el SBF (Figura 6 del Artículo 3 (pg. 79)) mostraron que las matrices liberaron iones calcio y silicio tras 1 día de inmersión. Hasta los 14 días la concentración de iones silicio aumentó considerablemente en el medio a una razón de ~0.19 mg/día, lo que demostró que la fase disuelta contenía una gran cantidad de silicio. En consecuencia, se puede afirmar que dicha fase era la silicocarnotita. La disolución de la silicocarnotita en SBF está respaldada por el diagrama de fases P₂O₅-SiO₂-CaO-H₂O, en el que la silicocarnotita es inestable en presencia de agua [79-81]. La degradación de la fase de silicocarnotita creó una zona de reacción porosa sobre las superficies de las matrices en forma de lamelas alternas, cuya relación Ca/P fue muy cercana a la del apatito (Figura 3F del Artículo 3 (pg. 77)).

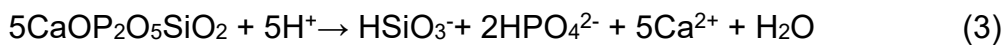
Por tanto, se puede afirmar que, en primer lugar, las matrices reaccionaron en SBF produciendo la disolución selectiva de la silicocarnotita y la posterior transformación pseudomórfica de las lamelas de α -TCP en apatito. En segundo lugar, ocurrió la formación de un precipitado tipo apatito sobre las lamelas previamente transformadas (Figura 4B del Artículo 3 (pg. 78)), que creció gradualmente hasta formar una capa densa y compacta hacia el final de la reacción (Figura 5A del Artículo 3 (pg. 78)). La formación del precipitado se vio favorecida por el incremento de la concentración de iones calcio tras 1 día de

inmersión. La posterior formación de una capa densa de precipitado provocó la disminución de dicha concentración a partir de los 3 días de inmersión y hasta el final de la reacción (Figura 6 del Artículo 3 (pg. 82)).

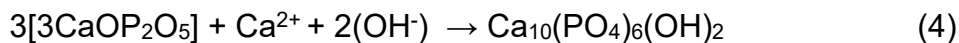
La disminución constante de la concentración de iones fósforo en el SBF, hasta los 21 días, se asoció con los dos procesos mencionados anteriormente.

El análisis general de los resultados de SEM, EDS, ATR-FTIR y TEM permitió clasificar a la capa de precipitado como un HA carbonatado y deficiente en calcio, similar a la fase mineral ósea [62-64]. También se detectó por microanálisis EDS una pequeña sustitución de iones silicio a los 21 días. Esto último, unido a una posible difusión más lenta de los iones Si a través de la densa capa de precipitado (desde el material y hacia el SBF), podría justificar la disminución en la concentración de iones silicio observada en la última semana.

Los resultados hasta aquí analizados pueden explicarse, en principio, por un mecanismo complejo que se describe a continuación (Figura 7 del Artículo 3 (pg. 79)). Al inicio del ensayo de bioactividad *in vitro* ocurrieron dos reacciones prácticamente simultáneas. En primer lugar, la fase de silicocarnotita reaccionó mediante un intercambio de iones Ca^{2+} de su red con iones H_3O^+ del SBF según la ecuación 3.

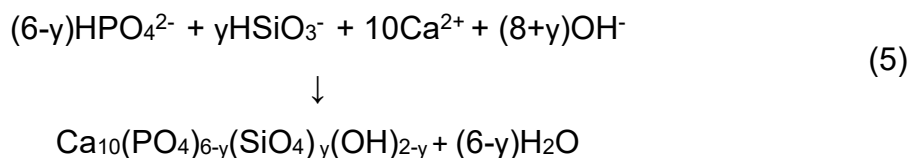


La reacción continuó hacia el interior a través de los canales estrechos formados por la disolución de la silicocarnotita entre las lamelas de α -TCP (Figura 7A del Artículo 3 (pg. 79)). Inmediatamente las lamelas de α -TCP comenzaron a reaccionar con los iones Ca^{2+} y $2(\text{OH}^-)$ que penetraron en los canales (Figura 7B del Artículo 3 (pg. 79)). En consecuencia, ocurrió la transformación pseudomórfica de dichas lamelas según la ecuación 4.



Los iones calcio y silicio disueltos, que no estuvieron implicados en la reacción de la ecuación 4, fueron los responsables del incremento de sus respectivas concentraciones en SBF. La posterior disminución de los iones calcio indicó que gran parte de éstos reaccionaron con el fósforo del SBF para producir la capa de

HA precipitado (Figura 7C del Artículo 3 (pg. 79)) según la reacción descrita por la ecuación 5.



El precipitado tuvo lugar sobre las lamelas previamente transformadas (Figura 4D del Artículo 3 (pg. 78)) y en algunas áreas se introdujo en los espacios creados por la disolución de la silicocarnotita (Figura 4B del Artículo 3 (pg. 78)). Finalmente el precipitado de HA cubrió todas las superficies de las matrices, pero no fue suficiente para llenar en su totalidad los espacios entre lamelas (Figura 7D del Artículo 3 (pg. 79)).

Resultados similares se encuentran en un material de composición eutéctica dentro del sistema TCP-Wollastonita, que reacciona en SBF transformando pseudomórficamente el TCP en HA [82]. Además, otros autores han sugerido la transformación *in vivo* de las cerámicas de TCP en HA [42,83] mediante procesos de disolución/precipitación semejantes [84,85].

De los resultados de los ensayos de bioactividad podemos concluir que la capacidad de las matrices 3D, de inducir la formación de HA *in vitro*, puede favorecer la unión química estable con el tejido óseo *in vivo*. Las dos fases (silicocarnotita y α -TCP) presentan propiedades químicas y tasas de degradación diferentes. La fase más soluble (silicocarnotita) reaccionaría mediante un rápido intercambio iónico con el medio circundante favoreciendo la bioactividad. Por otro lado, la fase más estable (α -TCP) permanecería como un soporte 3D para apoyar la formación de nuevo tejido.

Los ensayos de biocompatibilidad *in vitro* con ah-MSCs mostraron que estas fueron capaces de adherirse y proliferar sobre las matrices, formando una extensa monocapa tras 21 y 28 días de incubación (Figuras 8G-8I del Artículo 2 (pg. 72) y las Figuras 5H-5J del Artículo 4 (pg. 89)). No se encontraron evidencias de citotoxicidad o alteraciones morfológicas inducidas por el material a ninguno de los tiempos ensayados.

Los tests de viabilidad AB confirmaron una correcta función metabólica de las ah-MSCs en las matrices durante todos los ensayos, superando al control tras 21 y 28 días de incubación tanto en GM como en OM (Figura 9 del Artículo 2 (pg. 72) y Figura 8 del Artículo 4 (pg. 92)). Esto último puede deberse a varios factores individuales o relacionados entre sí. Por una parte, los productos de disolución de las matrices pudieran estar estimulando a las células para proliferar y diferenciarse. Segundo, las estructuras 3D altamente porosas de las matrices proporcionan mayor área superficial para la proliferación celular y el intercambio eficiente de oxígeno y nutrientes con el medio. Finalmente, la actividad metabólica significativamente superior en condiciones osteogénicas puede estar influenciada también por la presencia de β -glicerofosfato en el OM. El β -glicerofosfato es una molécula de señalización con una influencia significativa sobre los procesos de proliferación celular [86].

La actividad de la ALP en las ah-MSCs incubadas en contacto indirecto con las matrices fue significativamente superior que en el control a los 28 días, tanto en GM como en OM. Ya que la ALP es un marcador temprano de diferenciación osteogénica, los productos de disolución de las matrices pudieron haber influenciado a las ah-MSCs para diferenciar en fenotipo osteoblástico.

La formación de nanofibras tipo colágeno con depósitos de Ca-P tras los 28 días de incubación, sugirió la formación de matriz extracelular (Figura 5J del Artículo 4 (pg. 89)). El colágeno se encuentra en el tejido óseo en forma de nanofibras con orientaciones aleatorias y es en estas nanofibras donde crecen los primeros cristales de HA durante el proceso de biomineralización ósea [9,87]. Como son los osteoblastos las células encargadas de producir fibras de colágeno, se refuerza la idea de una posible diferenciación de las ah-MSCs por la acción del material de las matrices 3D. Sin embargo, se necesitan estudios más detallados para corroborar estas observaciones.

Tras los ensayos de biocompatibilidad *in vitro*, se observaron cambios importantes sobre las matrices 3D. En la interfase matriz-GM ocurrieron diferentes procesos como se detalla a continuación. Al inicio algunas células individuales se adhirieron directamente a las superficies de las matrices sin transformar. Simultáneamente, las áreas no cubiertas por las células

reaccionaron con el GM circundante para desarrollar una nanoestructura de lamelas alternas. Según el microanálisis EDS dichas lamelas tenían una relación Ca/P promedio de 1.98 y no presentaron trazas de silicio (Figura 6C del Artículo 4 (pg. 90)). A continuación tuvo lugar la formación de un precipitado tipo HA sobre las superficies previamente transformadas, que evolucionó en una estructura tipo “capa por capa” estrechamente relacionada con las membranas celulares (Figura 5I del Artículo 4 (pg. 89)). Todo esto sugirió un proceso de disolución/precipitación similar al descrito para los ensayos en SBF, donde se disolvió la silicocarnotita creando una zona de reacción nanoporosa en la superficie de las matrices y la subsecuente formación de una capa densa de HA sustituida con silicio. Esta vez dicha capa creció en contacto estrecho con las membranas celulares. La presencia de la HA se confirmó mediante análisis de TEM-SAD (Figura 7 del Artículo 4 (pg. 91)).

Los ensayos en SBF se han utilizado ampliamente para evaluar la bioactividad de los biomateriales y poder predecir su comportamiento *in vivo*. No obstante, algunos autores cuestionan la validez de esto, alegando que el SBF es un fluido inorgánico y que difiere de las condiciones reales de aplicación de los biomateriales [88]. Algunos estudios han desarrollado comparaciones de la bioactividad *in vitro*, de varias cerámicas y vidrios, utilizando SBF y medios de cultivo celular con concentraciones iónicas también similares a las del plasma sanguíneo humano, pero incluyendo factores de crecimiento y proteínas presentes en la sangre [89,90]. Aunque los ensayos en medios de cultivo celular retrasaron la precipitación de la HA, esta fue muy similar a la formada en SBF. Los ensayos de biocompatibilidad de las matrices 3D cerámicas con ah-MSCs en GM aquí discutidos, mostraron la precipitación de una capa de HA en un medio orgánico muy similar a la observada tras los ensayos en SBF.

La funcionalización de los biomateriales con diferentes moléculas y factores de señalización mejora la interacción con el tejido circundante. En este estudio, se eligió la ALP como modelo de proteína para la funcionalización de las matrices 3D, porque su actividad juega un papel fundamental en el proceso de mineralización del tejido óseo. La ALP se injertó con éxito en las matrices sin la necesidad de un tratamiento de superficie previo y su estado activo permaneció tras los 21 días de funcionalización (Figura 10 del Artículo 4 (pg. 93)). No

obstante, se necesitan estudios complementarios para comprender la naturaleza de la interacción de la ALP con las matrices 3D.

Finalmente, el examen por SEM del hueso trabecular natural de cerdo adulto confirmó las semejanzas físico-químicas y macro-/micro-/nano-estructurales entre este y las matrices 3D desarrolladas (Figura 1A-1F del Artículo 4 (pg. 86). Resaltar que la topografía de las superficies del hueso trabecular natural mostró una morfología en forma de lamelas alternas orientadas al azar, formadas por la extracción de las nanofibras de colágeno durante la preparación de las muestras. La nanoestructura en lamelas alternas que se forma sobre las superficies de las matrices al reaccionar en SBF y GM se asemeja a la estructura observada sobre las superficies del hueso trabecular natural. El desarrollo de nanoestructuras superficiales proporciona porosidad adicional a los materiales, favoreciendo la biactividad y la adhesión celular.

6. Conclusiones

A continuación se exponen, de forma general, las conclusiones más relevantes de la presente memoria de Tesis Doctoral.

- Se sintetizaron polvos cerámicos de composición eutectoide cercana al punto invariante del subsistema Silicocarnotita-TCP contenido en el sistema Silicato dicálcico-TCP.
- Se obtuvieron matrices 3D cerámicas por el método de réplica sobre esponja polimérica, con una composición mineralógica (53.6% en peso de silicocarnotita y 46.4% en peso de α -TCP) muy próxima a la del punto invariante eutectoide del subsistema Silicocarnotita - TCP (53.4/46.6).
- La macro-/micro-/nano-estructura conseguida y la composición química de las matrices, se correspondieron con las del hueso trabecular natural.
- La nanoestructura se compuso de lamelas alternas bien definidas de silicocarnotita y α -TCP.
- Se controló la nanoestructura de lamelas y la resistencia a la compresión axial de las matrices mediante la velocidad de enfriamiento a través de la temperatura eutectoide.
- Las matrices reaccionaron en SBF disolviendo la fase de silicocarnotita y transformando pseudomórficamente el α -TCP en HA. Posteriormente ocurrió la precipitación de una capa de HA sustituido con silicio similar a la fase mineral ósea.
- Las matrices permitieron la adhesión y proliferación de las ah-MSCs que formaron una extensa capa sobre toda la estructura tras 28 días de cultivo.
- La ALP se incorporó en la estructura de las matrices de manera efectiva conservando su actividad enzimática tras 21 días de funcionalización.
- Las matrices 3D desarrolladas resultan de interés para aplicaciones en ITO.

7. Proyecciones Futuras

- Los ensayos de bioactividad y biocompatibilidad *in vitro*, realizados durante el desarrollo de la presente Tesis Doctoral, difieren de las condiciones reales de aplicación de los biomateriales dentro del cuerpo humano. Los fluidos corporales son dinámicos y renuevan constantemente las concentraciones iónicas y de nutrientes. Sería adecuado llevar a cabo ensayos dinámicos donde un flujo controlado recree las condiciones del interior del organismo, mediante el uso de bombas peristálticas o biorreactores.
- Los ensayos de biocompatibilidad mostraron indicios de una posible diferenciación osteogénica de las ah-MSCs mediante el incremento de la actividad de la ALP y la formación de nanofibras tipo colágeno con depósitos minerales en forma de matriz extracelular. Serían necesarios estudios complementarios que refuerzen esta hipótesis, como pueden ser la detección de otros marcadores específicos de diferenciación osteogénica (sialoproteína y osteocalcina) y tinciones para la detección de nódulos de mineralización.
- Finalmente serían necesarios estudios del comportamiento *in vivo* de las matrices 3D en modelos animales.

8. Referencias

1. <https://www.who.int/es/news-room/fact-sheets/detail/musculoskeletal-conditions/> 02/10/2020.
2. A. del Valle, D. Hautcoeur, A. Leriche, et al., Microstructural design of ceramics for bone regeneration, *J. Eur. Ceram. Soc.* 40 (2020) 2555-2565.
3. R.B. Heimann, H.D. Lehmann, *Bioceramic Coatings for Medical Implants: Trends and Techniques* (1), Wiley-VCH, Weinheim, 2015.
4. T.M. De Witte, L.E. Fratila-Apachitei, A.A. Zadpoor, et al., Bone tissue engineering via growth factor delivery: from scaffolds to complex matrices, *Regen. Biomater.* 5 (2018) 197-211.
5. M. Parent, H. Baradari, E. Champion, et al., Design of calcium phosphate ceramics for drug delivery applications in bone diseases: a review of the parameters affecting the loading and release of the therapeutic substance, *J. Contr. Release.* 252 (2017) 1–17.
6. J.M. Bouler, P. Pilet, O. Gauthier, et al., Biphasic calcium phosphate ceramics for bone reconstruction: a review of biological response, *Acta Biomater.* 53 (2017) 1–12.
7. L. Roseti, V. Parisi, M. Petretta, et al., Scaffolds for bone tissue engineering: state of the art and new perspectives, *Mater. Sci. Eng. C.* 78 (2017) 1246-1262.
8. R. Agarwal, A.J. García, Biomaterial strategies for engineering implants for enhanced osseointegration and bone repair, *Adv. Drug Deliv. Rev.* 94 (2015) 53-62.
9. S. Wu, X. Liu, K.W.K. Yeung, et al., Biomimetic porous scaffolds for bone tissue engineering, *Mat. Sci. Eng. R.* 80 (2014) 1-36.
10. J. Henkel, M.A. Woodruff, D.R. Epari, et al., Bone Regeneration Based on Tissue Engineering Conceptions – A 21st Century Perspective, *Bone Res.* 3 (2013) 216-248.
11. I. Fernández-Tresguerres-Hernández-Gil, M.A. Alobera-Gracia, M. del Canto-Pingarrón, et al., Physiological bases of bone regeneration I. Histology and physiology of bone tissue. *Med. Oral Patol. Oral Cir. Bucal.* 11 (2006) 47-51.

Referencias

12. S. Ohba, F. Yano, Ch. Ung-il, Tissue engineering of bone and cartilage, *Bone Key.* 6 (2009) 405–419.
13. F.R.A.J. Rose, R.O.C. Oreffo, Bone Tissue Engineering: Hope vs Hype, *Biochem. Bioph. Res. Co.* 292 (2002) 1-7.
14. W. Wang, K.W.K. Yeung, Bone grafts and biomaterials substitutes for bone defect repair: A review, *Biact. Mater.* 2 (2017) 224-247.
15. D.W. Hutmacher, Scaffolds in tissue engineering bone and cartilage, *Biomaterials.* 21 (2000) 2529-2543.
16. J.R. Jones, L.L. Hench, Regeneration of trabecular bone using porous ceramics, *Curr. Opin. Solid St. M.* 7(2003) 301-307.
17. M.T. Frey, I.Y. Tsai, T.P. Russell, et al., Cellular responses to substrate topography: role of myosin II and focal adhesion kinase, *Biophys J.* 90 (2006) 3774–3782.
18. Y. Yang, K. Wang, X. Gu, et al., Biophysical Regulation of Cell Behavior—Cross Talk between Substrate Stiffness and Nanotopography, *Engineering.* 3 (2017) 36-54.
19. X. Li, L. Wang, Y. Fan, et al., Nanostructured scaffolds for bone tissue engineering, *J. Biomed. Mater. Res. Part A.* 101A (2013) 2424–2435.
20. M.J. Dalby, N. Gadegaard, R. Tare, et al., The control of human mesenchymal cell differentiation using nanoscale symmetry and disorder, *Nature Mater.* 6 (2007) 997–1003.
21. L. Gasperini, J.F. Mano, R.L. Reis, Natural polymers for the microencapsulation of cells, *J. R. Soc. Interface.* 11 (2014) 20140817.
22. F. Khan, M. Tanaka, Designing smart biomaterials for tissue engineering, *Int. J. Mol. Sci.* 19 (2018) 17-30.
23. F. Matassi, L. Nistri, D. Paez, et al., New biomaterials for bone regeneration, *Clin. Cases Miner. Bone Metab.* 8 (2011) 21-24.
24. J.C. Liao, C.C. Niu, W.J. Chen, et al., Polyetheretherketone (PEEK) cage filled with cancellous allograft in anterior cervical discectomy and fusion, *Int. Orthop.* 32 (2008) 643–648.
25. S. Ragunathan, G. Govindasamy, D.R. Raghul, et al., Hydroxyapatite reinforced natural polymer scaffold for bone tissue regeneration, *Mater. Today.* 23 (2020) 111-118.

26. C.E. Holy, J.A. Fialkov, J.E. Davies, et al., Use of a biomimetic strategy to engineer bone, *J Biomed. Mater. Res.* 65A (2003) 447-553.
27. O.M. Böstman, O.M. Laitinen, O. Tynniinen, et al., Tissue restoration after resorption of polyglycolide and poly-laevo-lactic acid screws, *J. Bone Joint Surg. Br.* 87B (2005) 1575–1580.
28. U. Sentuerk, P. von Roth, C. Perka, Ceramic on ceramic arthroplasty of the hip, new materials confirm appropriate use in young patients, *Bone Joint J.* 98B (2016) 14-17.
29. J.N. Oliver, Y. Su, X. Lu, et al., Bioactive glass coatings on metallic implants for biomedical applications, *Bioact. Mater.* 4 (2019) 261-270.
30. G.R. Owen, M. Dard, H. Larjava, Hydroxyapatite/beta-tricalcium phosphate biphasic ceramics as regenerative material for the repair of complex bone defects, *J. Biomed. Mater. Res. Part B Appl. Biomater.* 106 (2017) 2493-2512.
31. L.L. Hench, J.M. Polak, Third generation biomedical materials, *Science.* 295 (2002) 1014-1017.
32. P. Ducheyne, Q. Qiu, Bioactive ceramics: the effect of surface reactivity on bone formation and bone cell function, *Biomaterials.* 20 (1999) 2287–2303.
33. S.V. Dorozhkin, Bioceramics of calcium orthophosphates, *Biomaterials.* 31 (2010) 1465–1485.
34. R. Fujita, A. Yokoyama, T. Kawasaki, et al., Bone augmentation osteogenesis using hydroxyapatite and β-tricalcium phosphate blocks, *J. Oral Maxillofac. Surg.* 9 (2003) 1045-1053.
35. K. Hayashi, R. Kishida, A. Tsuchiya, et al., Honeycomb blocks composed of carbonate apatite, β-tricalcium phosphate, and hydroxyapatite for bone regeneration: effects of composition on biological responses, *Materials Today Bio.* 4 (2019) 100031.
36. R.G. Carrodeguas, S. De Aza, α-Tricalcium phosphate: Synthesis, properties and biomedical applications, *Acta Biomater.* 7 (2011) 3536-3546.
37. N. Patel, S.M. Best, W. Bonfield, et al., A comparative study on the *in vivo* behavior of hydroxyapatite and silicon substituted hydroxyapatite granules, *J. Mater. Sci.: Mater. Med.* 13 (2002) 1199–1206.

38. I.D. Xynos, A.J. Edgar, L.D.K. Butterly, et al., Ionic products of bioactive glass dissolution increase proliferation of human osteoblasts and induce insulin-like growth factor II mRNA expression and protein synthesis, *Biochem. Bioph. Res. Co.* 276 (2000) 461–465.
39. I.D. Xynos, A.J. Edgar, L.D.K. Butterly, et al., Gene-expression profiling of human osteoblasts following treatment with the ionic products of Bioglass 45S5 dissolution, *J. Biomed. Mater. Res.* 155 (2000) 151–157.
40. A.M. Pietak, J.W. Reid, M.J. Stott, et al., Silicon substitution in the calcium phosphate bioceramics, *Biomaterials.* 28 (2007) 4023-4032.
41. G. Fielding, J. Feuerstein, A. Bandyopadhyay, et al., SiO₂ and SrO Doped β -TCP: Influence of Dopants on Mechanical and Biological Properties. *Biomaterials Science: Processing, Properties and Applications II: Ceram. Trans.* 237 (2012) 171-181.
42. A.K. Gaharwar, S.M. Mihaila, A. Swami, et al., Khademhosseini, Bioactive silicate nanoplates for osteogenic differentiation of human mesenchymal stem cells, *Adv. Mater.* 25 (2013) 3329-3336.
43. E.M. Carlisle, Silicon: a possible factor in bone calcification, *Science* 167 (1970) 279 -280.
44. C.D. Seaborn, F.H. Nielsen, Effects of germanium and silicon on bone mineralization, *Biol. Trace Elem. Res.* 42 (1994) 151–164.
45. J. Reid, L. Tuck, M. Sayer, et al., Synthesis and characterization of single-phase silicon-substituted alpha-tricalcium phosphate, *Biomaterials.* 27 (2006) 2916–2925.
46. J.E. Mate-Sanchez de Val, J.L. Calvo-Guirado, R.A. Delgado-Ruiz, M.P. RamirezFernandez, I.M. Martinez, J.M. Granero-Marin, et al., New block graft of α -TCP with silicon in critical size defects in rabbits: chemical characterization, histological, histomorphometric and micro-CT study, *Ceram. Int.* 38 (2012) 1563–1570.
47. P. Velasquez, Z.B. Luklinska, L. Meseguer-Olmo, et al., α -TCP ceramic doped with dicalcium silicate for bone regeneration applications prepared by powder metallurgy method: *in vitro* and *in vivo* studies, *J. Biomed. Mater. Res. A*, 2012, pp. 1943–1954.

48. R.W. Nurse, J.H. Welch, W. Gutt, High-Temperature Equilibria in the System Dicalcium Silicate-Tricalcium Phosphate, *J. Am. Chem. Soc.* (1959) 1077-1083.
49. W. Fix, H. Heymann, R. Heinke, Subsolidus relations in System $2\text{CaO}\cdot\text{SiO}_2\text{-}3\text{CaO}\cdot\text{P}_2\text{O}_5$, *J. Am. Ceram. Soc.* 52 (1969) 346-347.
50. V. Rubio, M.A de la Casa-Lillo, S. De Aza, et al., The System $\text{Ca}_3(\text{PO}_4)_2\text{-Ca}_2\text{SiO}_4$: The Sub-System $\text{Ca}_2\text{SiO}_4\text{-}7\text{CaOP}_2\text{O}_5\text{SiO}_2$, *J. Am. Ceram. Soc.* 94(2011) 4459-4462.
51. P. Ros-Tárraga, P. Mazón, L. Meseguer-Olmo, et al., Revising the Subsystem Nurse's A-Phase-Silicocarnotite within the System $\text{Ca}_3(\text{PO}_4)_2\text{-Ca}_2\text{SiO}_4$, *Materials.* 9 (2016) 322.
52. I.M. Martinez, P. Velasquez, P.N. De Aza, The Sub-System $\alpha\text{-TCPss-Silicocarnotite}$ Within the Binary System $\text{Ca}_3(\text{PO}_4)_2\text{-Ca}_2\text{SiO}_4$, *J. Am. Ceram. Soc.* 95(2012) 1112-1117.
53. B. Dickens, W.E. Brown, The crystal structure of $\text{Ca}_5(\text{PO}_4)_2\text{SiO}_4$ (silico-carnotite), *Tschermaks Mineral. Petrogr. Mitt.* 16 (1971) 1–27.
54. J.A. Rincón-López, J.A. Hermann-Muñoz, N. Cinca-Luis, et al., Apatite Mineralization Process from Silicocarnotite Bioceramics: Mechanism of Crystal Growth and Maturation, *Cryst. Growth Des.* 20 (2020) 4030-4045.
55. W. Lu, W. Duan, Y. Guo, et al., Mechanical properties and *in vitro* bioactivity of $\text{Ca}_5(\text{PO}_4)_2\text{SiO}_4$ bioceramic, *J. Biomater. Appl.* 26 (2012) 637-650.
56. S. Zhao, L. Peng, G. Xie, et al., Effect of the interposition of calcium phosphate materials on tendon-bone healing during repair of chronic rotator cuff tear, *Am. J. Sports Med.* 42 (2014) 1920-1929.
57. T. Kokubo, H. Takadama, How useful is SBF in predicting *in vivo* bone bioactivity?, *Biomaterials.* 27 (2006) 2907-2915.
58. ISO/FDIS 23317, Implants for Surgery- *In Vitro* Evaluation for Apatite-Forming Ability of Implant Materials.
59. S. N. Rampersad, Multiple applications of Alamar Blue as an indicator of metabolic function and cellular health in cell viability bioassays, *Sensors (Basel).* 12 (2012) 12347-12360.

60. E.E. Golub, K. Boesze-Battaglia, The role of alkaline phosphatase in mineralization, *Curr. Opin. Orthop.* 18 (2007) 444–448.
61. E. Verné, S. Ferraris, C. Vitale-Brovarone, et al., Bioactive glass functionalized with alkaline phosphatase stimulates bone extracellular matrix deposition and calcification *in vitro*, *Appl. Surf. Sci.* 313 (2014) 372–381.
62. X. Su, K. Sun, F.Z. Cui, et al., Organization of apatite crystals in human woven bone, *Bone*. 32 (2003) 150–162.
63. B. Kerebel, G. Daculsi, A. Verbaere, High-resolution electron microscopy and crystallographic study of some biological apatites, *J. Ultrastruct. Res.* 57 (1976) 266–275.
64. A. Antonakos, E. Liarokapis, T. Leventouri, Micro-Raman and FTIR studies of synthetic and natural apatites, *Biomaterials* 28 (2007) 3043–3054.
65. I. Rehman, W. Bonfield, Characterization of hydroxyapatite and carbonated apatite by photo acoustic FTIR spectroscopy, *J. Mater. Sci. Mater. Med.* 8 (1997) 1–4.
66. R. Yilmén, U. Jäglid, Carbonation of portland cement studied by diffuse reflection fourier transform infrared spectroscopy, *Int. J. Concr. Struct. Mater.* 7 (2013) 119–125.
67. C. Ruiz-Aguilar, U. Olivares-Pinto, E.A. Aguilar-Reyes et al., Characterization of β-tricalcium phosphate powders synthesized by sol-gel and mechanochemical synthesis, *Bol. Soc. Esp. Ceram. V.* 57 (2018) 213–20.
68. H. Rehman, M. Zhang, Preparation of porous hydroxyapatite scaffolds by combination of the gel-casting and polymer sponge methods, *Biomaterials*. 24 (2003) 3293–3302.
69. J.M. Cordell, M.L. Vogl, A.J. Waganer-Johnson, The influence of micropore size on the mechanical properties of bulk hydroxyapatite and hydroxyapatite scaffolds, *J. Mech. Behavior of Biomed. Mat.* 2 (2009) 560–570.
70. S.W. Choi, Y. Zhang, Y. Xia, Three-dimensional scaffolds for tissue engineering: the importance of uniformity in pore size and structure, *Langmuir*. 26 (2010) 19001–19006.

71. R.A. Pérez, G. Mestres, Role of pore size and morphology in musculo-skeletal tissue regeneration, *Mat. Sci. Eng. C.* 61 (2016) 922–939.
72. J. Zhang, X. Luo, D. Barbieri, et al., The size of surface microstructures as an osteogenic factor in calcium phosphate ceramics, *Acta Biomat.* 10 (2014) 3254–3263.
73. J.M Sobral, S.G. Caridade, R.A. Sousa, et al., Three dimensional plotted scaffolds with controlled pore size gradients: effect of scaffold geometry on mechanical performance and cell seeding efficiency, *Acta Biomater.* 7 (2011) 1009–1018.
74. C.M. Murphy, M.G. Haugh, F.J. O'Brien, The effect of mean pore size on cell attachment, proliferation and migration in collagen-glycosaminoglycan scaffolds for bone tissue engineering, *Biomaterials* 31 (2010) 461–466.
75. V. Karageorgiou, D. Kaplan, Porosity of 3D biomaterial scaffolds and osteogenesis, *Biomaterials*. 26 (2005) 5475–5491.
76. D.M. Stefanescu, Science and Engineering of Casting Solidification, 3rd ed.; Springer International Publishing: Cham, Switzerland, 2015.
77. L.T. Bang, K. Ishikawa, R. Othman Effect of silicon and heat-treatment temperature on the morphology and mechanical properties of silicon—Substituted hydroxyapatite, *Ceram. Int.* 37 (2011) 3637–3642.
78. Y.U. Kim, B.H. Lee, M.C. Kim, et al., Effect of Cooling Rate and Particle Size on Compressive Strength of Macroporous Hydroxyapatite, *Key Eng. Mater.* 309–311 (2006) 1047–1050.
79. J. Hu, D.K. Agrawal, R. Roy, Investigation of hydration phases in the system CaO–SiO₂–P₂O₅–H₂O, *J. Mater. Res.* 3 (1988) 772–780.
80. P. Vanis, I. Odler, Hydration reactions in the system CaO–P₂O₅–SiO₂–(H₂O), *J. Am. Ceram. Soc.* 79 (1996) 1124–1126.
81. M.W. Barnes, M. Klimkiewicz, P.W. Brown, Hydration in the system Ca₂SiO₄–Ca₃(PO₄), at 90°C, *J. Am. Ceram. Soc.* 75 (1992) 1423–1429.
82. A.H. De Aza, P. Velasquez, M.I. Alemany, et al., *In situ* bone-like apatite formation from a Bioeutectic® ceramic in SBF dynamic flow, *J. Am. Ceram. Soc.* 90(2007) 1200–1207.
83. R.Z. LeGeros, A.M. Gatti, R. Kijkowska, et al., Mg-substituted tricalcium phosphates: formation and properties, *Key Eng. Mater.* 254–256 (2004) 127–130.

84. A.K. Rajasekharan, M. Andersson, Role of nanoscale confinement on calcium phosphate formation at high supersaturation, *Cryst. Growth Des.* 15 (2015) 2775–2780.
85. A. Lotsari, A.K. Rajasekharan, M. Halvarsson, et al., Transformation of amorphous calcium phosphate to bone-like apatite, *Nat. Commun.* 9 (2018) 4170.
86. M. Kanatani, T. Sugimoto, J. Kano, et al., IGF-I mediates the stimulatory effect of high phosphate concentration on osteoblastic cell proliferation, *J. Cell. Phys.* 190 (2002) 306–312.
87. J.A. Buckwalter, M.J. Glimcher, R.R. Cooper, et al., Bone Biology. Part I: Structure, Blood Supply, Cells, Matrix, and Mineralization, *J. Bone Jt. Surg. Am.* 77 (1995) 1256–1275.
88. M. Bohner, J. Lemaitre, Can bioactivity be tested *in vitro* with SBF solution?, *Biomaterials.* 30 (2009) 2175–2179.
89. G. Lutisanova, M.T. Palou, J. Kozankova, Comparison of bioactivity *in vitro* of glass and glass ceramic materials during soaking in SBF and DMEM medium, *Ceram. Silik.* 55 (2011) 199–207.
90. G. Theodorou, O.M. Goudouri, E. Kontonasaki, Et al., Comparative Bioactivity Study of 45S5 and 58S Bioglasses in Organic and Inorganic Environment, *Bioceram. Dev. Appl.* 1 (2011) 1–4.

9. Anexos: Compendio de Artículos

9.1. Artículo 1

Thank you for your order with RightsLink / John Wiley and Sons

12 de marzo de 2021, 13:10



Thank you for your order!

Dear Prof. Piedad de Aza,

Thank you for placing your order through Copyright Clearance Center's RightsLink® service.

Order Summary

Licensee:	Universidad Miguel Henandez de Elche
Order Date:	Mar 12, 2021
Order Number:	5026450987347
Publication:	Journal of the American Ceramic Society
Title:	Eutectoid scaffold as a potential tissue engineer guide
Type of Use:	Dissertation/Thesis
Order Ref:	1
Order Total:	0.00 EUR

View or print complete [details](#) of your order and the publisher's terms and conditions.

Sincerely,

Copyright Clearance Center

Tel: +1-855-239-3415 / +1-978-646-2777
customercare@copyright.com
<https://myaccount.copyright.com>



Eutectoid scaffold as a potential tissue engineer guide

Anabel Díaz-Arca¹  | Patricia Mazón²  | Piedad N. De Aza¹ 

¹Instituto de Bioingeniería, Universidad Miguel Hernández, Elche, Alicante, Spain

²Departamento de Materiales, Óptica y Tecnología Electrónica, Universidad Miguel Hernández, Elche, Alicante, Spain

Correspondence

Patricia Mazón, Departamento de Materiales, Óptica y Tecnología Electrónica, Universidad Miguel Hernández, Avda. Universidad s/n, Elche, Alicante 03202, Spain.
Email: pmazon@umh.es

Abstract

Biphasic scaffolds were prepared according to the eutectoid composition from subsystem silicocarnotite-tricalcium phosphate by the polymeric replica method. Two polyurethane templates were used to explore the possibility of fabricating the scaffold on demand. The obtained scaffolds were characterized mineralogically by X-Ray Diffraction (XRD), the chemical groups analyzed by Attenuated Total Reflectance-Fourier Transformed Infrared Spectroscopy (ATR-FTIR), microstructurally by Scanning Electron Microscopy (SEM) fitted with Energy Dispersive X-Ray Spectroscopy (EDS), and additionally by field emission SEM (FESEM) for the topography study. Finally, the mercury porosimetry analysis was performed for the microporosity study. The obtained results confirmed the possibility of controlling macro- and microporosity on the scaffold, which allowed their synthesis for specific needs.

KEY WORDS

bioceramics, microstructure, scaffols

1 | INTRODUCTION

Increasing life expectancy, which has caused aging-related diseases such as osteoporosis, together with injuries and traumas, have drawn many attention to bone tissue research. Despite the best bone substitute being bone itself by either using autografts or allografts, these options have their drawbacks, such as poor availability and health risks. Hence considerable interest is shown in synthetic bone replacement materials which in some cases, have proven even superior to autografts.¹ Although different materials have been used as potential scaffolds, for example, metallic, polymeric, and ceramic materials, bioceramics based on calcium phosphates have given the best results because their composition comes close to the mineral part of bone, together with their biocompatibility, osteoconduction and osteoinductive capability.^{2,3}

Natural bone is described as a gradient structure that includes a dense wall (cortical bone) and a porous core (trabecular bone). Trabecular bone is composed of a strut and a network of pore. Tissue engineering aims to mimic this natural composite assemble by bone biomimetic scaffolds.

Porous ceramic structures have been fabricated according to different techniques such as use of porogen, 3D printing, or polymeric replication.^{4–6}

In order to obtain the ideal scaffold, research has focused on obtain an interconnected high porous structure for uniform cell seeding and spreading, diffusion of nutrients, and bone ingrowth. Pore size^{7–9} and the option between a homogeneous¹⁰ or heterogeneous distribution,¹¹ change the scaffold's behavior. The influence of surface topography on the scaffold as being key for the good adhesion and proliferation of cells and biological metabolites is as well accepted.¹² In summary, interconnectivity, pore size, pore distribution, and porosity level need to be balanced to guide proper tissue ingrowth, and an equilibrium must be achieved with scaffold degradation as it must provide mechanical support during regeneration.

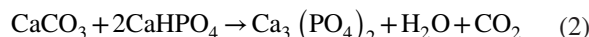
Several researchers have explored the use of biphasic scaffolds for tissue engineering, based on hydroxyapatite:tricalcium phosphate,^{13–15} or diopside:calcium phosphate mixtures.¹⁶ With this background, the present study aimed to develop a bioceramic with a composition according to the eutectoid point from subsystem $5\text{CaO}\cdot\text{P}_2\text{O}_5\cdot\text{SiO}_2$ (Silicocarnotite)- $\text{Ca}_3(\text{PO}_4)_2$ (Tricalcium phosphate)¹⁷ with

a porous structure obtained by the polymer replica method to get a biphasic porous lamellar structure that can act as a guide in tissue regeneration. Lamellar microstructure is expected to favored an additional porosity generated by different degradation rate of both phases present, allowing at the same time the mechanical support by the remaining phase. It would be a novel approach from previous granular biphasic scaffold.

2 | MATERIALS AND METHODS

2.1 | Ceramic synthesis

The eutectoid ceramic was prepared from the corresponding oxides, all of commercial grade: CaHPO₄ (Panreac, Castellar del Vallès, Spain), CaCO₃ (>99 wt% Fluka, St. Louis, MO), and SiO₂ (>99.7 wt% Strem Chemical, Inc., Newburyport, MA, USA), according to the stoichiometric reaction from the individual equilibrium (Equations 1 and 2) in agreement with subsystem 5CaO·P₂O₅·SiO₂-Ca₃(PO₄) revised by Martínez et al.¹⁷ and corresponding to 83:17 wt% of Ca₂SiO₄-Ca₃(PO₄)₂ (C₂S-TCP), respectively.



The desired proportions from the raw materials were weighed and homogenized in an agate mortar with acetone, and were isostatically pressed into bars at 200 MPa. Bars were heated up to 1500°C for 3 hours. Liquid nitrogen quenching of ceramic bars by rapidly removed from the furnace, was done before being ground and homogenized with isopropyl alcohol in a mixing miller (Retsch MM301) using PSZ-zirconia balls as a grinding media. Thermal treatment was then performed in a platinum crucible at 1550°C for 3 hours, including 1100°C for 24 hours, followed by slow cooling inside the furnace. The sintering and annealing temperatures were selected based on preliminary studies of this phase equilibrium diagram revised in our laboratory.

In order to achieve marked particle size reduction, additional grinding was done in a planetary miller (Retsch PM100) using PSZ-zirconia balls as grinding media. Several grinding periods were studied (from 30 minutes to 4 hours).

2.2 | Characterization of raw material

The mineralogical characterization of the raw material obtained by a solid-state reaction was made by XRD. XRD patterns were obtained in a Bruker AXS D8-Advance X-ray diffractometer (Karlsruhe, Germany) using λCuKα1 radiation (0.15418 nm) and a secondary curved graphite

monochromator. The database from the Joint Committee on Powder Diffraction Standards (JCPDS) was used as a reference.

Particle size was analyzed in Mastersize 2000 equipment (APA2000; Malvern Instruments Ltd., Malvern, PA) followed by scanning electron microscopy (SEM-Hitachi S-3500N, Ibaraki, Japan) for their morphology analysis.

2.3 | Preparing scaffolds by the polymer replica method

The powder that resulted from grinding was mixed with H₂O, Optapix PAF 35 (Zschimmer & Schwarz, Chemische Fabriken, Lahnstein, Germany) as a binder, and with Dolapix CE 64 (Zschimmer & Schwarz, Chemische Fabriken) as a dispersant, to obtain the appropriate ceramic slurry for polyurethane (PU) sponge's uniformly and complete impregnation. The PU templates had a diameter of 8 mm and height 7 mm (ratio ~1). Two different templates were selected to study how different pore size and distribution could influence the mechanical properties and the future bioactivity rate and osteointegration, referenced as small template (ST), ppi 40, and large template (LT) ppi 25.

Sponges were immersed in suspension twice to acquire a greater mechanical strength of the final scaffolds. Any excess was removed by squeezing. After the first impregnation and prior to the following one, pores were opened by air pressure. The covered templates were air-dried for 24 hours and were submitted to thermal treatment, including a step at 1550°C and a plateau at 1100°C for ceramic consolidation, which gave the desired scaffolds, which were called small scaffold (SS) and large scaffold (LS). Scaffold shrinkage's percentage was calculated from volume measure before and after thermal treatment.

2.4 | Scaffolds characterization

The samples porosity and pore size distribution for both prepared scaffolds were done by mercury porosimetry in a Poremaster-60 GT (Quantachrome Instruments, Boyton Beach, FL) within the 5.395-410785 KPa pressure range, which corresponds to a pore diameter range between 300 and 0.0035 μm. Three samples (~0.80 g) were analyzed for every scaffold type by this technique. One more sample was also used in each case if the obtained porosity values differed by more than 5%.

The SEM technique was followed for the microstructural study of the scaffolds, followed by field emission SEM (FESEM) (Merlin TM VP Compact, Carl Zeiss Microscopy S.L., Oberkochen, Germany). The chemical composition analysis was performed by fitting SEM with EDS (INCA system by Oxford Instruments Analytical, UK).

The chemical bond analysis of the scaffolds was done by ATR-FTIR. Spectra were obtained in a Thermo SCIENTIFIC Nicolet iS5 equipped with an iDR ATR accessory. All the spectra were collected at room temperature with a resolution of 4 cm^{-1} and the measurement range was $4000\text{-}500\text{ cm}^{-1}$, at 2 cm^{-1} resolution, averaging 64 scans. Pellets were prepared by milling.

3 | RESULTS

3.1 | Ceramic material characterization

The ceramic powder obtained after the corresponding thermal treatment was characterized mineralogically by XRD (Figure 1). The obtained diffraction peaks were compared with references from the JCPDS database, and only the crystalline phases assigned to silicocarnotite (JCPDS card No. 73-1181) and alpha polymorph of TCP ($\alpha\text{-TCP}$) (JCPDS card No. 09-0348) were shown, as it is described below the eutectoid point. Slight displacement was observed from the JCPDS cards in the diffraction peaks because of solid solution.

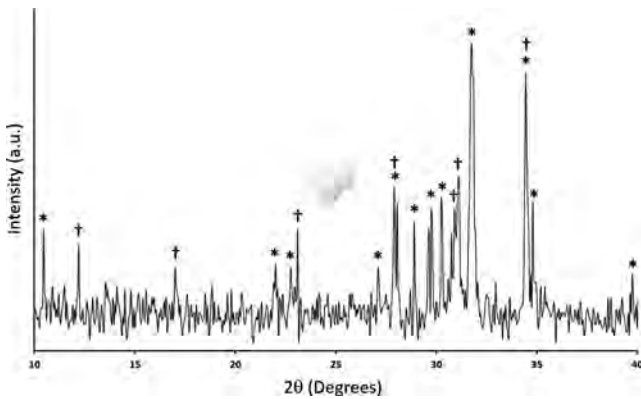


FIGURE 1 XRD pattern of the ceramic-base material for scaffolds, showing the two crystalline phases present (*) Silicocarnotite and (†) $\alpha\text{-TCP}_{ss}$

Preparing scaffolds by the polymer replica technique requires a fine homogeneous powder so that powder was also ground by a planetarium grinder from 30 minutes to 4 hours. Different grinding periods were assayed to achieve the smallest and narrowest particle size distribution. The particle size study is included in Figure 2A. Different milling times were well characterized by XRD for possible amorphization with milling (Figure 2B).

The optimum grinding time was 1.5 hours, because it presents the best combination of smallest and narrowest particle size distribution, which resulted in an average particle size of $12\text{ }\mu\text{m}$, favoring the following slurry preparation. No significant differences in the crystalline degree were observed for milling times and neither in crystalline phases present.

The SEM analysis on powder morphology was also carried out for the different milling times. In all cases, agglomeration of irregular-shaped particles was observed, as seen representatively for the optimum milling time of 1.5 hours. (Figure 3).

3.2 | Scaffold preparation and characterization

Scaffolds were prepared by the polymer replica method. Figure 4 A,B shows a representative image of both templates (ST, LT), where we can see differences in pore sizes for each scaffold, which enables them to reach multiporosity. A relatively high temperature is required to achieve adequate ceramic consolidation. Figure 4 C,E. depicts how the template structure remains after thermal treatment, which allows a scaffold with interconnected porosity that mimics cancellous bone to be obtained. The pore size of templates determines the pore size of the ceramic scaffold after the corresponding shrinkage (34%) linked to the firing step. Despite of this shrinkage, macrostructure were keep without pores closing observed, as it is shown in Figure 4 A,B windows images. XRD analysis of the obtained scaffolds were realized in order to check possible mineralogical changes, as it is shown in

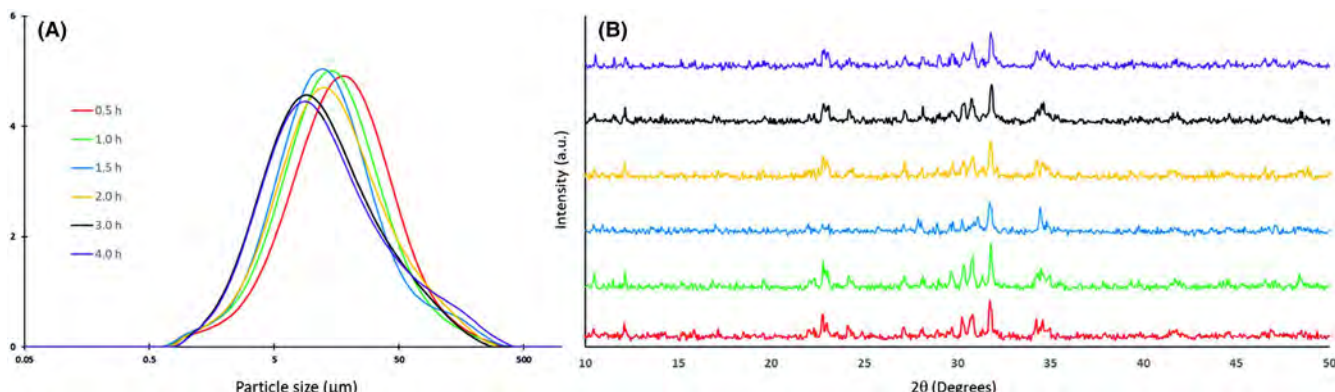


FIGURE 2 (A) Particle size distribution of ceramic powder and (B) the XRD pattern of the different milling times

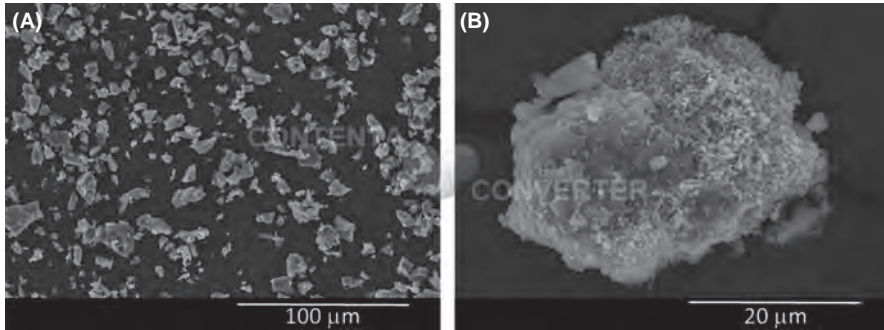


FIGURE 3 Scanning electron microscopy images of the powder material at the 1.5 h. milling time showing (A) a representative image of the set and (B) detail of agglomeration

Figure 4 D for LS as representative one. No extra phases were observed, although a slight crystallinity loss could be observed by increasing noise.

The microstructure of the scaffolds was studied by SEM (Figure 5). Great pore interconnectivity was observed in macroporosity images (Figure 5 A,B) in both cases, and the characteristic hollow nature when the polymer replica method is followed.¹⁸ Struts presented almost full densification after sintering (Figure 5 C,D), which guarantees adequate handling, although some microporosity was observed (Figure 5 E,F) at high magnification.

The SEM measures of the struts and pore sizes of scaffolds were taken by recording 20 measures per sample in triplicate in each scaffold. The obtained results are shown in Table 1.

Struts and pore measures revealed a random distribution in the microstructure. The macropores presented on the scaffolds were grouped in two ranges for the SS and three wider ranges for the large one. The micropores on the macropore surfaces greatly increased the surface area of the graft for an osseous tissue interaction in the microenvironment.

Mercury porosimetry was used to analyze the microporosity level and distribution (see the results in Figure 6). Mercury penetrated the increasingly smaller pores with increasing pressure.

To better comprehend the porosity level on the scaffold, the obtained results are summarized in Table 2. As expected, differences in pore size and distribution were observed between scaffolds (Figure 6), which agreed with the measures taken by SEM and as well related to intra- and interparticle porosity.

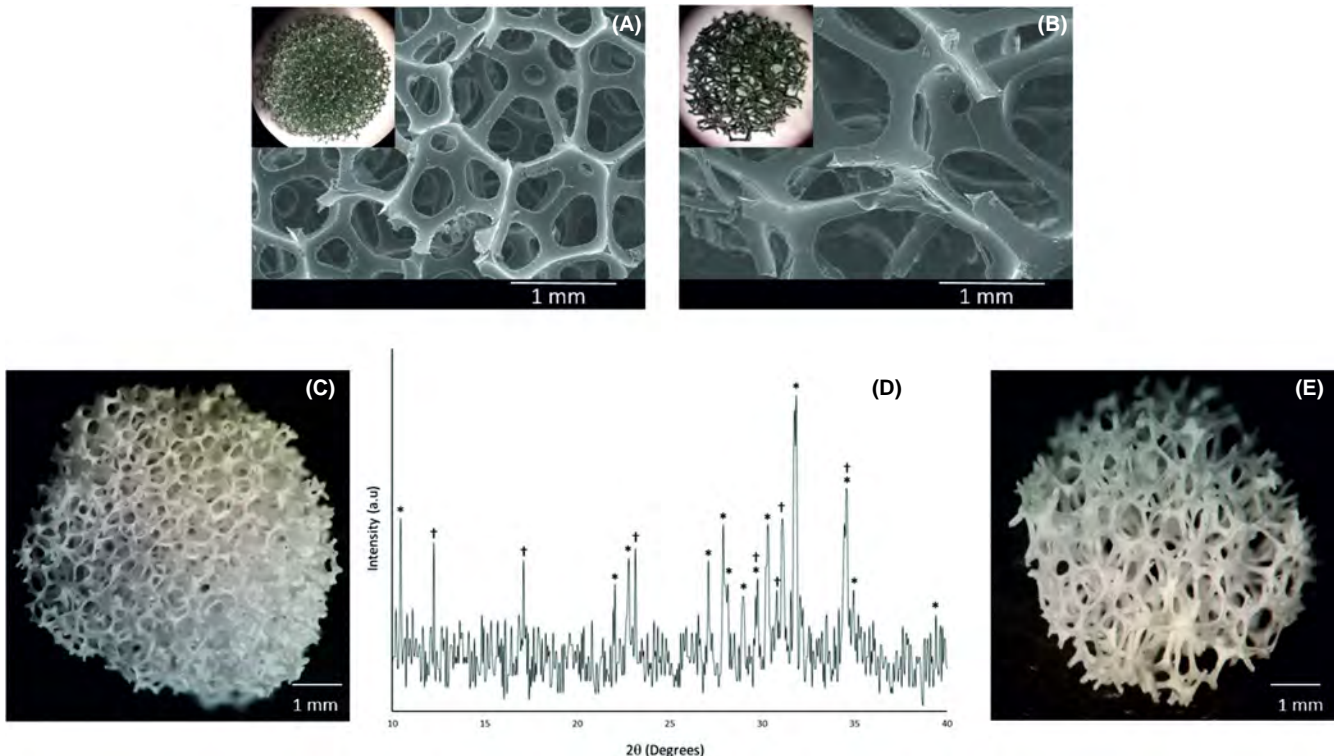


FIGURE 4 SEM micrographs including the corresponding optical images (window) of (A) small template and (B) large template. Optical images after thermal treatment for scaffolds (C) small scaffold (E) large scaffold and (D) XRD pattern for LS scaffold

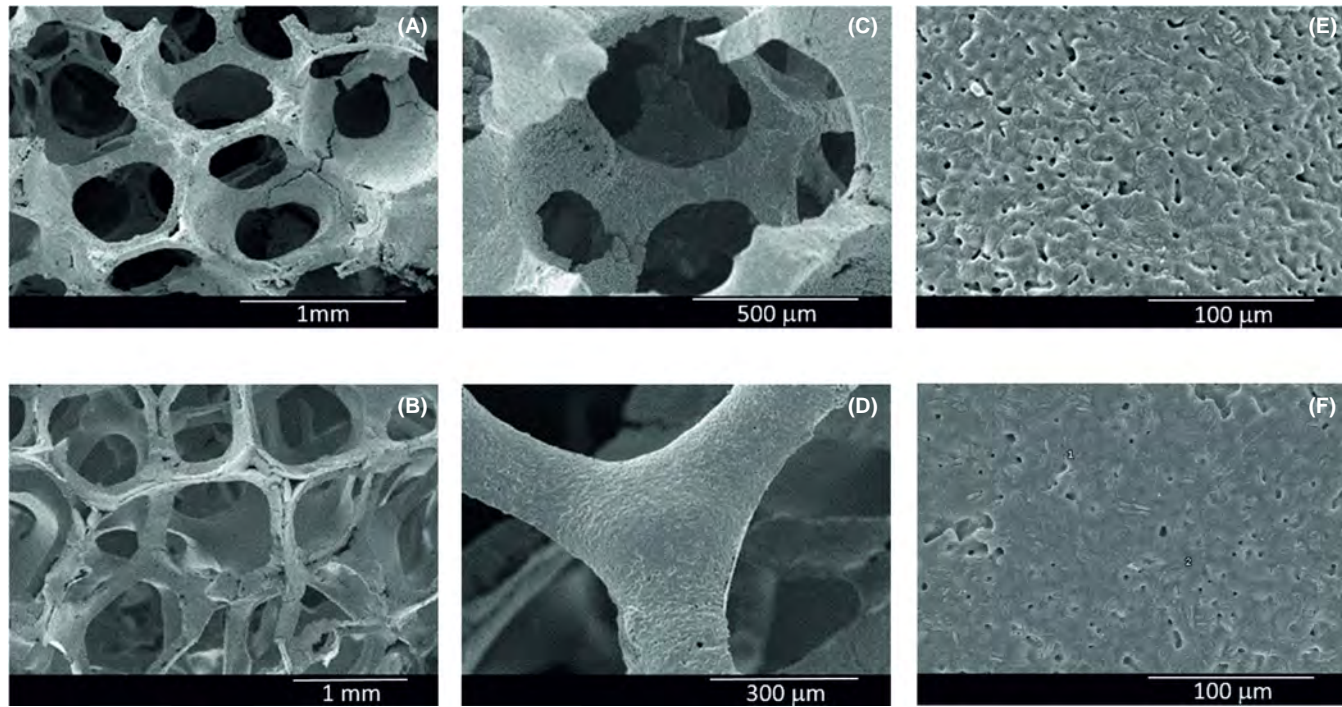


FIGURE 5 SEM images for scaffolds showing small scaffold (A, C, E) and large scaffold (B, D, F); (A, B) macroporosity, detail of struts (C, D) and detail of microporosity (E, F)

TABLE 1 Scanning electron microscopy measures of the struts and pore sizes of the scaffolds

	Small scaffold (μm)	Large scaffold (μm)
Struts	70-170	120-310
Pore size range	140-350	370-600
	350-600	600-850
		850-1500

The chemical bond characterization of the scaffolds was made by FTIR-ATR as seen in Figure 7. FTIR absorption

for the phases they were constituted of was also included to perform a better analysis.

Although both spectra presented striking similarities, the absorption bands of the LS were more defined. Significant absorptions fell within the $1200-500\text{ cm}^{-1}$ range. Accordingly the main bands corresponding to the silicate groups (SiO_4^{4-} tetrahedral) overlapped the vibrational modes for the phosphate groups (PO_4^{3-} tetrahedral), and the infrared spectrum of the phases that our scaffold was constituted of were also performed (Silicocarnotite and α -TCP_{ss}). Although it was not possible to well distinguish the absorptions from the silicate groups, a narrowing of the P–O stretch peak, and a shift in its position to the upper wavenumbers due to them were appreciated.¹⁹

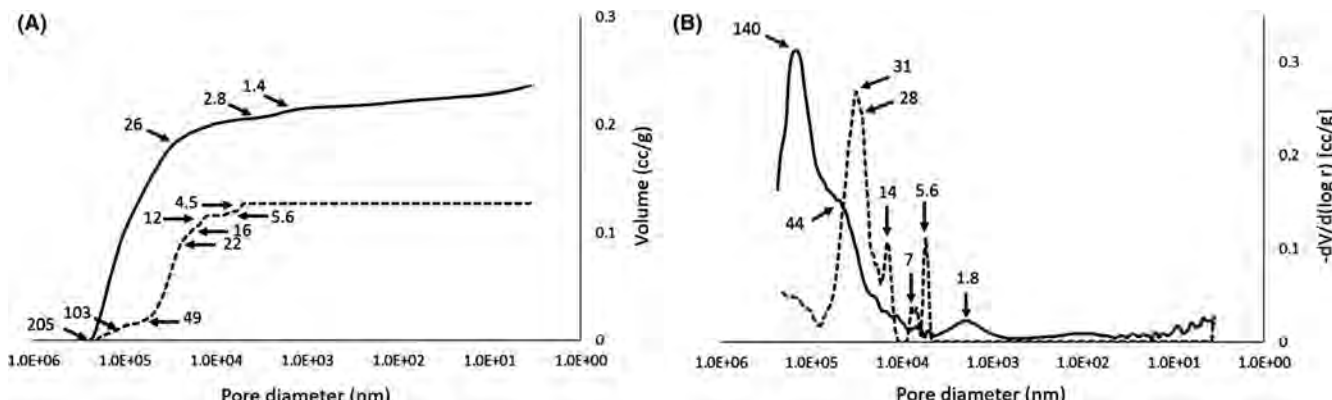


FIGURE 6 (A) Cumulative curve vs pore diameter and (B) differential volume for small scaffold (dotted line) and large scaffold (continuous line)

TABLE 2 Porosity and density results for the scaffolds

Scaffold	Apparent density network (g cc^{-1})	Total porosity network (%)	Intrusion volume (g cc^{-1})	Intraparticle porosity network (%) ^a	Interparticle porosity network (%) ^b	Scaffold porosity (g cc^{-1})
SS	1.9515	30.02	0.1653	0.12	29.90	95
LS	1.7440	41.21	0.2363	5.35	35.86	96

Abbreviations: LS, large scaffold; SS, small scaffold.

^aCorresponding to pores $< 1 \mu\text{m}$.

^bCorresponding to $1 \mu\text{m} < \text{pores} < 300 \mu\text{m}$.

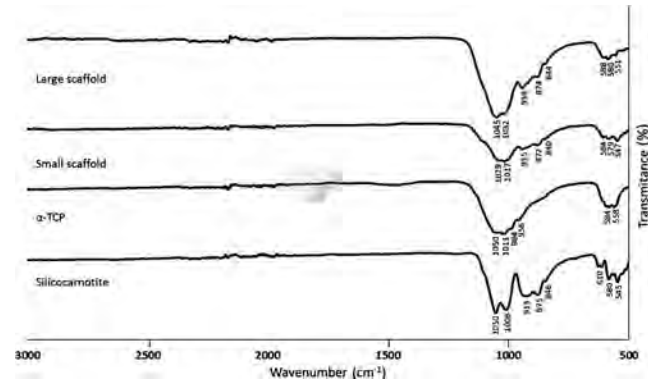


FIGURE 7 Fourier transformed infrared spectroscopy-ATR for both scaffolds and the phases they are constituted of

The ultrastructure of the LS, as the representative one, is shown in Figure 8, after chemical etching with acetic acid (1% concentration) for 4 seconds. The SEM images indicated an irregular morphology of alternating lamellae of α -TCP_{ss} and Silicocarnotite, which corresponded to the eutectoid invariant point. The lamellar structure not only appeared on the surface, but it also penetrated pores (Figure 8A, middle image).

The FESEM-EDS analysis was done to better characterize and identify lamellae. Both surface rough topography and the lamellar structure were observed (Figure 8B). The EDS analysis confirmed that the phase eliminated by chemical etching was α -TCP_{ss} and that observed corresponded to the silicon deficient Silicocarnotite as it was checked by a comparison made with the Silicocarnotite monophasic material (Figure 8C,D).

4 | DISCUSSION

In recent years, biomaterials research has focused on developing porous structures as scaffolds that can act as temporary guides for tissue engineering. These templates must present a large surface area to facilitate ion-exchange, protein absorption, proper vascularization, etc., which are a series of events involved in regeneration processes.^{20,21} Studies have shown

that pores with diameters in the order of hundreds of micrometers favor nutrient and metabolite transport by promoting new bone ingrowth, while those diameters in the order of ten of micrometers allow the exchange of nutrients and the discharge of metabolites.²² No consensus about porosity levels has yet been reached, and different reports can be found on ideal porous size,²³ along with studies proposing what is known as multiporosity.¹¹ The main aim would be to design scaffolds for specific needs.

In this context, our goal was to achieve a scaffold that included different porosity levels that would be capable to adapting it to demand by a simple strategy such as the polymer replication method.⁶ A biphasic composition, Silicocarnotite-TCP_{ss}, was selected based on preliminary studies,¹⁷ which can evolve once implanted into a lamellar morphology, along with a porous structure. In this way, we combined Silicocarnotite, described as a very close structure to HA²⁴ with a good bioactive response,²⁵ and TCP, which is strikingly similar to the mineralogical bone structure and it has been successfully used when doped with silicon.^{26,27} When combined they would form a hierarchical structure that could mimic cancellous bone.

The ceramic base material was prepared by a solid-state reaction, and its mineralogical characterization by XRD (Figure 1) showed a biphasic composition including Silicocarnotite and α -TCP_{ss}, checked by the JCDPS data-base, and was concordant with the phase diagram¹⁷ at a nominal composition of eutectoid point 83 wt% TCP-17 wt% C₂S. The presence of silicon in the high temperature α -TCP polymorph allows it to stabilize at room temperature.^{28,29} This polymorph has been shown to present greater solubility and higher degradability *in vivo*³⁰ compared to β -TCP. Silicon doping has been reported as an osteogenesis promotor and a way to retard α -TCP biodegradation.^{31,32}

Scaffolds were prepared by the polymer replica method. This strategy allowed us to prepare a three-dimensional network from ceramic slurry using a PU foam as a template, which provided the 3D structure.^{6,33,34} In order to obtain adequate covering by ceramic, slurry must be composed of particles with a small and narrow size. Milling in a planetary miller for different periods of time was done (Figure 2A) to

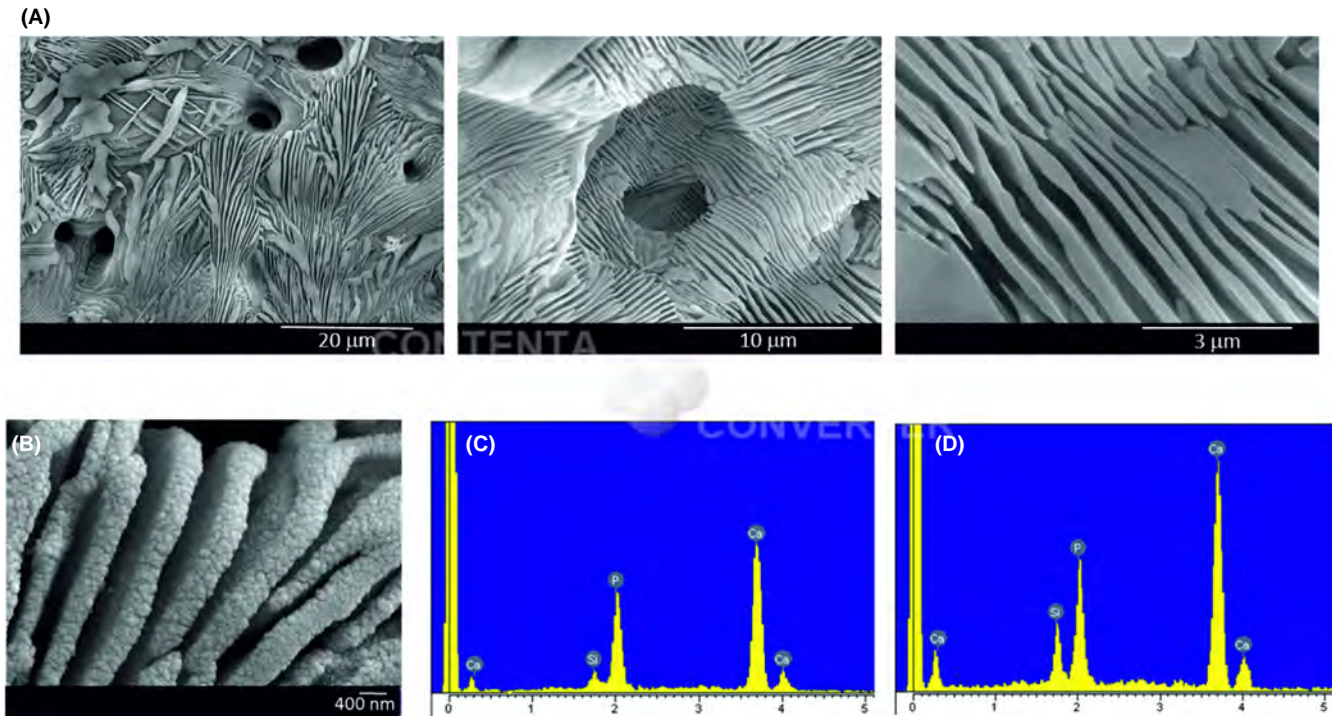


FIGURE 8 (A) SEM images of the lamellar morphology of the large scaffold, (B) FESEM image of the lamellar morphology of large scaffold, (C) the EDS analysis of the lamellae structure and (D) the EDS of Silicocarnotite phase pattern

find that the narrowest distribution took place at a 1.5 hours milling time ($\sim 12 \mu\text{m}$). Some authors have described that this reduction in particle size by milling could influence the crystallinity degree on TCP.³⁵ Thus, the XRD analysis was studied for different milling times (Figure 2B), but no significant differences were found in the diffraction peaks, which revealed possible amorphization in powders.

A morphological analysis by SEM of the different particle sizes was also run. It showed irregular agglomerated particles for all the milling times, as seen in Figure 3 for the 1.5 hours milling time, taken as the representative time.

Prior to impregnation, a morphological analysis of the PU templates was done to check both porosity level and pore size distribution. For both templates, it revealed good interconnectivity and pore size in a random distribution in two orders: a small pore size for that called ST (Figure 4A) and bigger for that called LT (Figure 4B).

Ceramic suspension must be fluid enough to cover the whole PU template, but must also allow structure maintenance. The impregnated templates were air-dried and submitted to thermal treatment to burn out the sponge, and to consolidate the ceramic to confer the scaffold strength. Remarkably, no intermediate polymeric calcination step was necessary³³ and scaffolds were obtained in one step without collapsing and with adequate handling. The XRD analysis of the obtained scaffolds compared to powder material (Figure 4D, XRD pattern for LS as representative

one), presented no extra phases, but a slight crystallinity loss could be observed.

The scaffolds obtained after thermal treatment had a spongy bone appearance that allowed adequate handling. Their optical images (Figure 4C,E) showed an identical 3D structure from the starting PU template.

The SEM microstructural analysis confirmed high interconnected porosity for large and small pore sizes in both scaffolds (Figure 5), which could favor not only uniform cell seeding and distribution, but also nutrient and metabolites diffusion. The random pore distribution was classified into two ranges for the SS and into three for the large one, as shown in Table 1. Densified struts were measured in the 70-170 μm range for the SS and within the 120-310 μm range for the large one. Microporosity was observed inside the morphology, as was the typical hollow defect associated with this strategy.^{33,36} The large pore surface area obtained by means of interconnected porosity will allow a better bone-scaffold interaction.

Apart from the macroporosity information, mercury porosimetry was performed to collect information about the microporosity on the scaffolds (Figure 6). The micropores on the macropore surface considerably increased the surface area of the potential implant. This study offers information about inter- and intraparticle pores by mercury penetration with increasing pressure. Minor differences were observed for the scaffolds. For the large one, one main absorption

on the cumulative curve was observed, from 205 to 26 μm , which corresponded to an intense peak in the differential volume centered around 140 μm , while two main absorptions appeared (204–49 μm , 49–22 μm) for the small one, which corresponded to the peaks centered at 30 and 14 μm . Afterward, minor absorptions in both scaffolds were observed for the pores within the 1–10 μm range. The first absorptions correlated with the filling of interparticle spaces, whereas the later ones correlated with the filling of intraparticle spaces.

Despite some discrepancies about an ideal pore size, it is well established that pores below 10 μm provide a larger surface area for the implant–natural bone interaction that contributes to protein adsorption, ion exchange and bone-like apatite formation,³⁷ and pores around 100 μm favor osteoblast initial adhesion and allowing their migration to the implant.^{38–40} However, bigger pores (>300 μm) are needed to also enhance new bone formation.⁸ Depending on specific needs, a balanced combination of macro- and micropores should be tailored for cell penetration and protein adsorption.^{11,21,23}

The obtained summary results (Table 2) confirmed a network porosity of ~30% for the SS and one of ~41% for the large one, as well as some differences related to intra- and interparticle porosity. These differences reinforce our idea of manufacturing them for a specific aim. However, it is important to note that the mercury porosimetry technique is more adequate for intraparticle pores analyses, especially with pores below 300 μm ; indeed, part of the porosity observed by SEM is not herein presented. Macroporosity was studied by the Archimedes method in H₂O, from five samples, with high porosity up to 96% found in both scaffolds.

Both scaffolds presented FTIR-absorptions between 1200–500 cm^{-1} , with high intensity for the large one (Figure 7). The double band observed at 1000–1050 cm^{-1} corresponded to the overlapping for the phosphate and silicate stretching vibrations.^{41,42} The absorptions at 870 and 920 cm^{-1} , which corresponded to the symmetric stretching (ν_1) of silicate groups, were weakly observed for the scaffolds due to the Silicocarnotite phase, as observed intensively for the corresponding monophasic spectrum. At 550–600 cm^{-1} the bands corresponding to the O–P–O symmetric vibrations (ν_4) appeared.⁴³

The lamellae microstructure of the LS as the representative one was studied by chemical etching with acetic acid (1%) for 4 seconds. As expected, both a lamellar morphology¹⁷ and porous structure were observed (Figure 8A) and it extended to the pores. It could be observed how lamellar morphology appeared as well at the third level of pores (Figure 8A, middle image), with a medium lamellar size between 200–350 nm. The ultrastructural analysis was done by FESEM to obtain a better resolution (Figure 8B), where these lamellae also presented a roughness topography due to grain sintering. Surface textures, additionally to porosity favor adhesion and

the spreading of cells, which improve bioactivity and tissue regeneration.⁴⁴ The lamellae structure was assumed to be composed of alternative lamellae of Silicocarnotite and α -TCP_{SS}. Although several chemical etching times and dissolutions were studied, only one lamellae was identified. The EDS composition analysis of this lamellae confirmed that it did not correspond to any of the phases initially present in the material. The TCP phase degraded because of acid etching and Silicocarnotite appeared as a silicon deficient Silicocarnotite, as seen in the EDS analysis by a comparison with that corresponding to the Silicocarnotite phase (Figure 8 C,D).

Further bioactivity and mechanical studies are currently underway to completely evaluate the scaffolds.

5 | CONCLUSION

By the polymeric replica method, preparing scaffolds with an interconnected macroporous structure that includes multiporosity to favor cell proliferation, nutrient diffusion, and ion exchange by ensuring healthy bone tissue growth and maintaining adequate handling for tissue engineering purposes is possible. Scaffolds present a biphasic composition that develop a lamellar structure, as well as surface topography at a high interconnected porosity level (up to 96%). The adopted strategy allowed us to fabricate scaffolds on demand by controlling their macroporosity (given by different templates) and as well we could explore microporosity level by means of sintering temperature and time.

ORCID

Anabel Díaz-Arca  <https://orcid.org/0000-0001-7925-9258>

Patricia Mazón  <https://orcid.org/0000-0001-7704-7577>

Piedad N. De Aza  <https://orcid.org/0000-0001-9316-4407>

REFERENCES

1. Russell TA, Leighton RK. Comparison of autogenous bone graft and endothermic calcium phosphate cement for defect augmentation in tibial plateau fractures. *J Bone Joint Surg Am.* 2008;90(10):2057–61.
2. LeGeros RZ. Calcium phosphate-based osteoinductive materials. *Chem Rev.* 2008;108(11):4742–53.
3. Jingyi L, Huijun Y, Chuanzhong C. Biological properties of calcium phosphate biomaterials for bone repair: a review. *RSC Adv.* 2018;8:2015–33.
4. Mazón P, De Aza PN. Porous scaffold prepared from α'_L -dicalcium silicate doped with phosphorus for bone grafts. *Ceram Int.* 2018;44(1):537–45.
5. Wu C, Luo Y, Cuniberti G, Xiao Y, Gelinsky M. Three-dimensional printing of hierarchical and tough mesoporous bioactive glass scaffolds with a controllable pore architecture, excellent

- mechanical strength and mineralization ability. *Acta Biomater.* 2011;7:2644–50.
6. Ros-Tárraga P, Murciano A, Mazón P, Gehrke S, De Aza PN. New 3D stratified Si-Ca-P porous scaffolds obtained by sol-gel and polymer replica method: microstructural, mineralogical and chemical characterization. *Ceram Int.* 2017;43(14):6548–53.
 7. Itala AI, Ylanen HO, Ekholm C, Karlsson KH, Aro HT. Pore diameter of more than 100 μm is not requisite for bone ingrowth in rabbits. *J Biomed Mat Res.* 2001;58(6):679–83.
 8. Karageorgiou V, Kaplan D. Porosity of 3D biomaterial scaffolds and osteogenesis. *Biomaterials.* 2005;26:5475–91.
 9. Pérez RA, Mestres G. Role of pore size and morphology in musculo-skeletal tissue regeneration. *Mat Sci Eng C.* 2016;61:922–39.
 10. Choi SW, Zhang Y, Xia Y. Three-dimensional scaffolds for tissue engineering: the importance of uniformity in pore size and structure. *Langmuir.* 2010;26(24):19001–6.
 11. Cordell JM, Vogl ML, Waganer-Johnson AJ. The influence of micropore size on the mechanical properties of bulk hydroxyapatite and hydroxyapatite scaffolds. *J Mech Behavior of Biomed Mat.* 2009;2:560–70.
 12. Hench LL. Sol-gel materials for bioceramic applications. *Curr Op. Sol St M.* 1997;2(5):604–10.
 13. Gauthier O, Bouler JM, Aguado E, Pilet P, Daculsi G. Macroporous biphasic calcium phosphate ceramics: influence of macropore diameter and macroporosity percentage on bone ingrowth. *Biomaterials.* 1998;19:133–9.
 14. Habibovic P, Yuan H, Van der Valk CM, Meijer G, Van Blitterswijk CA, De Groot K. 3D microenvironment as essential element for osteoinduction by biomaterials. *Biomaterials.* 2005;26:3565–75.
 15. Schopper C, Ziya-Ghazvini F, Goriwoda W, Moser D, Wanschitz F, Spassova E, et al. HA/TCP compounding of a porous CaP biomaterial improves bone formation and scaffold degradation—a long-term histological study. *J Biomed Mater Res Part B: Appl Biomater.* 2005;74B:458–67.
 16. Ramezani S, Emadi R, Kharaziha M, Tavangarian F. Synthesis, characterization and in vitro behavior of nanostructured diopside/biphasic calcium phosphate scaffolds. *Mat Chem Phys.* 2017;186:415–25.
 17. Martínez I, Velásquez P, De Aza PN. The subsystem α -TCP_{ss}-Silicocarnotite within the binary system Ca₃(PO₄)₂–Ca₂SiO₄. *J Am Ceram Soc.* 2012;95(3):1112–7.
 18. Tulliani JM, Montanaro L, Bell TJ, Swain MV. Semiclosed-cell mullite foams: preparation and macro and micromechanical characterization. *J Am Ceram Soc.* 1999;82(4):961–8.
 19. Ning CK, Mehta J, El-Ghannam A. Effects of silica on the bioactivity of calcium phosphate composites in vitro. *J Mater Sci Mater in Med.* 2005;16(4):355–60.
 20. Fernandez-Yague MA, Abbah SA, McNamara L, Zeugolis DI, Pandit A, Biggs MJ. Biomimetic approaches in bone tissue engineering: integrating biological and physicomechanical strategies. *Adv Drug Deliv Rev.* 2015;85:1–29.
 21. Bobbert F, Zadpoor AA. Effects of bone substitute architecture and surface properties on cell response, angiogenesis, and structure of new bone. *J Mater Chem B.* 2017;5(31):6175–92.
 22. Gao C, Deng Y, Feng P, Mao Z, Li P, Yang B, et al. Current progress in bioactive ceramic scaffolds for bone and regeneration. *Int J Mol Sci.* 2014;15:4714–32.
 23. Bruzauskaitė I, Bironaitė D, Bagdonas E, Bernotienė E. Scaffolds and cells for tissue regeneration: different scaffold pore sizes-different cell effects. *Cytotechnology.* 2016;68:355–69.
 24. Dickens B, Brown WE. The crystal structure of Ca₅(PO₄)₂SiO₄ (silico-carnotite). *Tschermaks Min Petr Mitt.* 1971;16:1–27.
 25. Duan W, Ning C, Tang T. Cytocompatibility and osteogenic activity of a novel calcium phosphate silicate bioceramic: silicocarnotite. *J Biomed Mater Res Part A.* 2013;101A:1955–61.
 26. Carrodeguas RG, De Aza S. α -Tricalcium phosphate: synthesis, properties and biomedical applications. *Acta Biomater.* 2011;7(10):3536–46.
 27. Lu J, Yu H, Chen Ch. Biological properties of calcium phosphate materials for bone repair: a review. *RSC Adv.* 2018;8(4):2015–33.
 28. Martínez I, Velásquez P, Meseguer-Olmo L, De Aza PN. Production and study of in vitro behavior of monolithic α -tricalcium phosphate based ceramics in the system Ca₃(PO₄)₂–Ca₂SiO₄. *Ceram Int.* 2011;37(7):2527–35.
 29. Velásquez P, Luklinska ZB, Meseguer-Olmo L, Mate-Sánchez de Val JE, Delgado-Ruiz RA, Calvo-Guirado JL, et al. α -TCP ceramic doped with dicalcium silicate for bone regeneration applications prepared by powder metallurgy method: in vitro and in vivo studies. *J Biomed Mater Res Part A.* 2013;101(7):1943–54.
 30. Wakae H, Takeuchi A, Udo K, Matsuya S, Munar MI, LeGeros RZ, et al. Fabrication of macroporous carbonate apatite foam by hydrothermal conversion of α -tricalcium phosphate in carbonate solutions. *J Biomed Mater Res.* 2008;87A(4):957–63.
 31. Maté-Sánchez de Val JE, Calvo-Guirado JL, Delgado-Ruiz RA, Ramírez-Fernández MP, Negri B, Abboud M, et al. Physical properties, mechanical behavior, and electron microscopy study of a new α -TCP block graft with silicon in an animal model. *J Biomed Mater Res A.* 2012;100A(12):3446–54.
 32. Mate-Sánchez de Val JE, Calvo-Guirado JL, Delgado-Ruiz RA, Ramírez-Fernández MP, Martínez IM, Granero-Marín JM, et al. New block graft of α -TCP with silicon in critical size defects in rabbits: chemical characterization, histological, histomorphometric and micro-CT study. *Ceram Int.* 2012;38(2):1563–70.
 33. Montanaro L, Jorand Y, Fantozzi G, Negro A. Ceramic foams by powder processing. *J Europ Ceram Soc.* 1998;18:1339–50.
 34. Vitale-Brovarone C, Verné E, Robiglio L, Appendino P, Bassi F, Martinasso G, et al. Development of glass-ceramic scaffolds for bone tissue engineering: characterisation proliferation of human osteoblasts and nodule formation. *Acta Biomater.* 2007;3:199–208.
 35. Ruiz-Aguilar C, Olivares-Pinto U, Aguilar-Reyes EA, López-Juarez R, Alfonso I. Characterization of β -tricalcium phosphate powders synthesized by sol-gel and mechanosynthesis. *Bol Soc Esp Ceram V.* 2018;57(5):213–20.
 36. Chen QZ, Thomson ID, Boccachini AR. 45S5 Bioglass®-derived glass-ceramic scaffolds for bone tissue engineering. *Biomaterials.* 2006;27:2414–25.
 37. Zhang J, Luo X, Barbieri D, Barradas A, de Brujin JD, van Blitterswijk CA, et al. The size of surface microstructures as an osteogenic factor in calcium phosphate ceramics. *Acta Biomater.* 2014;10(7):3254–63.
 38. Murphy CM, Haugh MG, O'Brien FJ. The effect of mean pore size on cell attachment, proliferation and migration in collagen-glycosaminoglycan scaffolds for bone tissue engineering. *Biomaterials.* 2010;31:461–6.
 39. Sobral JM, Caridade SG, Sousa RA, Mano JF, Reis RL. Three dimensional plotted scaffolds with controlled pore size gradients: effect of scaffold geometry on mechanical performance and cell seeding efficiency. *Acta Biomater.* 2011;7(3):1009–18. <https://doi.org/10.1016/j.actbio.2010.11.003>

40. Teixeira LN, Crippa GE, Lefebvre LP, De Oliveira PT, Rosa AL, Beloti MM. The influence of pore size on osteoblast phenotype expression in cultures grown on porous titanium. *Int J Oral Maxillofac Surg.* 2012;41(9):1097–101.
41. Szumera M, Waclawska I. Spectroscopic and thermal studies of silicate-phosphate glass. *J Therm Anal Calorim.* 2007;88(1):151–6.
42. Jillavenkatesa A, Condrate RA. The infrared and raman spectra of β and α -tricalcium phosphate $\text{Ca}_3(\text{PO}_4)_2$. *Spectrosc Lett.* 1998;31(8):1619–31.
43. Słosarczyk A, Paluszkievicz C, Gawlicki M, Paszkiewicz Z. The FTIR spectroscopy and QXRD studies of calcium phosphate based materials produced from the powder precursors with different Ca/P ratios. *Ceram Int.* 1997;23(4):297–304.
44. Niu H, Lin D, Tang W, Ma Y, Duan B, Yuan Y, et al. Surface topography regulates osteogenic differentiation of MSCs via crosstalk between FAK/MAPK and ILK/ β -catenin pathways in a hierarchically porous environment. *ACS Biomater Sci Eng.* 2017;3:3161–75.

How to cite this article: Díaz-Arca A, Mazón P, De Aza PN. Eutectoid scaffold as a potential tissue engineer guide. *J Am Ceram Soc.* 2019;00:1–10.
<https://doi.org/10.1111/jace.16639>

9.2. Artículo 2

Rightslink® by Copyright Clearance Center



RightsLink®



Home



Help



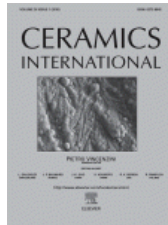
Email Support



Sign in



Create Account



In vitro characterization of new biphasic scaffolds in the sub-system Ca₃(PO₄)₂-Ca₅SiP₂O₁₂

Author: Anabel Díaz-Arca, Patricia Ros-Tárraga, Patricia Mazón, Piedad N. De Aza

Publication: Ceramics International

Publisher: Elsevier

Date: 1 August 2020

© 2020 Elsevier Ltd and Techna Group S.r.l. All rights reserved.

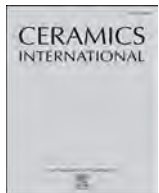
Journal Author Rights

Please note that, as the author of this Elsevier article, you retain the right to include it in a thesis or dissertation, provided it is not published commercially. Permission is not required, but please ensure that you reference the journal as the original source. For more information on this and on your other retained rights, please visit: <https://www.elsevier.com/about/our-business/policies/copyright#Author-rights>

BACK

CLOSE WINDOW

© 2021 Copyright - All Rights Reserved | [Copyright Clearance Center, Inc.](#) | [Privacy statement](#) | [Terms and Conditions](#)
Comments? We would like to hear from you. E-mail us at customercare@copyright.com



In vitro characterization of new biphasic scaffolds in the sub-system $\text{Ca}_3(\text{PO}_4)_2\text{--Ca}_5\text{SiP}_2\text{O}_{12}$



Anabel Díaz-Arca^{a,*}, Patricia Ros-Tárraga^b, Patricia Mazón^c, Piedad N. De Aza^a

^a Instituto de Bioingeniería, Universidad Miguel Hernández, Avda. de la Universidad s/n, 03202, Elche, Alicante, Spain

^b Grupo de Investigación en Regeneración y Reparación de Tejidos, UCAM Universidad Católica San Antonio de Murcia, 30107, Guadalupe, Murcia, Spain

^c Departamento de Ciencia de Materiales, Óptica y Tecnología Electrónica, Universidad Miguel Hernández, Edificio Torreviallo, Avda. de la Universidad s/n, 03202, Elche, Alicante, Spain

ARTICLE INFO

Keywords:

Powders
Solid state reaction
Interfaces
Apatite
Silicate
Biomedical applications

ABSTRACT

This work examines the *in vitro* bioactivity and biocompatibility of new biphasic scaffolds from eutectoid ceramic composition corresponding to the sub-system $\text{Ca}_3(\text{PO}_4)_2\text{--Ca}_5\text{SiP}_2\text{O}_{12}$, to evaluate their possible approach in bone tissue engineering. Scaffolds were synthesized by polymer replica method. Polyurethane sponges with desired pore size and geometry were used as templates, which were impregnated in barbotine and sintered by heat treatment. *In vitro* bioactivity was evaluated by different soaking times in simulated body fluid (SBF), according to Kokubo's method. Biocompatibility of adult human mesenchymal stem cells (ah-MSCs), in terms of adhesion and proliferation, were studied *in vitro* on the scaffolds' surface. Samples were characterized from mineralogical, chemical and microstructural point of view. Results showed that the bioactivity raised with increasing soaking time in SBF, giving place to a bone-like apatite surface transformation within 21 days. The ah-MSCs adhered and proliferated on the scaffolds' surface, establishing a close contact between them and forming an extensive monolayer to 21 days. Scaffolds presented a good *in vitro* bioactivity and biocompatibility then, they might be effective in future applications for bone tissue engineering.

1. Introduction

As a consequence of the increasing aging of world population and traumatic injuries, the number of patients needing treatment for bone diseases and trauma has significantly raised in the last few years. In that sense, bone defects reconstruction after suffering osteoporosis, fractures, tumor resections or trauma are still an important challenge in orthopedic surgery. Usual therapies involve bone autografts or allografts and prosthetic implant devices, which imply major restrictions such as lack of tissue availability, immune response, risk of disease transmission and non osseointegration [1–3]. Therefore, there is a clear medical need and it is necessary new strategies to address bone defects reconstruction.

Bone tissue engineering is a scientific discipline looking for new ways to regenerate bone defects combining cells, growth factors and three-dimensional scaffolds. The scaffolds can be defined as a temporal porous matrix with suitable chemical, biological, and structural properties to allow cell proliferation and support tissue ingrowth during bone regeneration process [4]. The ideal scaffold should have a highly interconnected porous network that mimics natural bone tissue

architecture. Furthermore, in order to establish a functional osseointegration, the scaffold should be biocompatible, bioactive and biodegradable.

Calcium phosphates have a chemical composition similar to bone mineral phase, therefore, they are biocompatible and integrate very well with natural bone tissue. Some authors propose that Si ion substitutions in calcium phosphates crystalline structures improve their biological properties. Si is an essential ion in bone regeneration process stimulating cells differentiation and proliferation [5–7].

Silicon-substituted calcium phosphates (Si-Ca-P) have demonstrated a good bioactivity and biocompatibility both *in vitro* and *in vivo* conditions [8–11], so these ceramics are promising candidates to develop new scaffolds for bone tissue engineering.

There are a lot of manufacturing techniques for scaffolds design such as gas foaming [12], sol-gel [13,14], polymer replica method [15,16], electrospinning [17,18] and rapid prototyping [19,20]. Polymer replica method is a widely used methodology to produce highly porous scaffolds from a barbotine. Using this technique, it is easy to obtain structures with a desired pore size and geometry adjustable to the bone defect shape.

* Corresponding author.

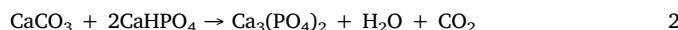
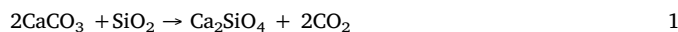
E-mail address: a.diaza@umh.es (A. Díaz-Arca).

Therefore, the aim of this work is to evaluate a new material with potential applications in bone tissue engineering. Si–Ca–P scaffolds were synthesized by polymer replica method from eutectoid ceramic composition of 46.6 wt% α -Ca₃(PO₄)₂ (α -TCP) and 53.4 wt% Ca₅SiP₂O₁₂ (Silicocarnotite), corresponding to the sub-system Ca₃(PO₄)₂–Ca₅SiP₂O₁₂ [21]. Also their bioactivity and biocompatibility were examined *in vitro*.

2. Materials and methods

2.1. Synthesis of ceramic powders

Taking into account the phases equilibrium in the sub-system Ca₃(PO₄)₂–Ca₅SiP₂O₁₂, ceramic powders with 46.6 wt% α -TCP and 53.4 wt% Silicocarnotite was synthesized by solid-state reaction from a stoichiometric mixture (equations (1) and (2)) of commercial oxides: SiO₂ (> 99.7 wt% Strem Chemical, Inc., Newburyport, MA, USA), CaCO₃ (> 99 wt% Fluka, St. Louis, MO, USA) and CaHPO₄ (Panreac, Castellar del Vallès, Spain).



Reagents were homogenized with acetone and heated in a platinum crucible at 1500 °C for 3 h followed by a liquid nitrogen quenching. Resulting material was wet ground in a mixing miller (MM30-Retsch) and heat treated according to the following sintering cycle: heating up to 1550 °C for 3 h followed by a cooling to 1100 °C for 24 h plateau and finally slow cooling into the furnace. Reduction of particle size was performed in a planetary miller (PM100-Retsch) with isopropyl alcohol and PSZ-zirconia balls ($\varnothing = 20$ mm) for 1.5 h at 300 rpm. Average particle size of the resulting ceramic powder was 12 μm . Sintering cycle and ceramic powder characterization were deep specified on a previous work developed in our laboratory [22].

2.2. Synthesis of porous scaffolds

Scaffolds were produced by polymer replica method using polyurethane sponge templates and a barbotine of pre-synthesized ceramic powders. Two different pore size distribution templates were selected: small template (ST) (ppi 40) and large template (LT) (ppi 25). Powder was mixed with deionized water, Dolapix CE 64 dispersant (Zschimmer & Schwarz, Chemische Fabriken, Lahnstein, Germany) and Optapix PAF 35 binder (Zschimmer & Schwarz, Chemische Fabriken, Lahnstein, Germany) to obtain the barbotine. Templates with cylinder-shape (8 mm of diameter and 7 mm of height) were immersed into the barbotine to get a complete impregnation and slightly squeezed to remove slurry excess. Pores were opened by air pressure to ensure a fully open porosity and the coated template were air-dried for 24 h. Finally, green structures were heat treated according to the following sintering cycle: heating at 1550 °C for 4 h; cooling to 1100 °C for 24 h plateau and finally slow cooling into the furnace [22]. Two kind of scaffolds were obtained with different pore size distribution according to the selected template: small scaffold (SS) and large scaffold (LS).

2.3. Scaffolds characterization

Mineralogical composition of scaffolds was examined by X-Ray Diffraction (XRD). Pattern was obtained in a Bruker AXS D8-Advance X-Ray Diffractometer (Karksruhe, Germany) using Bragg-Brentano ($\theta/2\theta$) vertical geometry, $\lambda_{\text{CuK}\alpha 1}$ radiation (0.15418 nm) and a secondary curved graphite monochromator. Information provided by XRD patterns was compared with data collected in the Crystallography Open Database (COD) to evaluate the constituent phases.

Microstructural examination was made by Scanning Electron Microscopy (SEM-Hitachi S-3500 N) (20 kV) and qualitative chemical

characterization was achieved by Energy Dispersive Spectroscopy (EDS) of INCA system by Oxford Instruments Analytical, UK. Each sample was palladium coated before SEM examination. A more detailed description of mineralogical, structural and chemical characterization of both scaffolds was developed in a previous work [22].

2.4. In vitro bioactivity test

In vitro bioactivity was evaluated by different soaking times in SBF, according to the protocol established by Kokubo and Takadama [23]. Both scaffolds were placed into falcon test tubes with 50 ml of SBF at 37 °C. After 3, 7, 14 and 21 days of soaking samples were withdrawn, dried at room temperature and palladium coated for SEM-EDS examination. Changes in calcium (Ca), phosphorus (P) and silicon (Si) concentrations were monitored at different soaking time by Inductively Coupled Plasma Optical Emission Spectrometry (ICP-OES) in PerkinElmer Optima 2000™. Product formed on the scaffolds' surface was mechanical removed by scalpel blade and analyzed by Attenuated Total Reflectance Fourier-Transform Infrared Spectroscopy (ATR-FTIR) between 4000 and 500 cm^{-1} at 2 cm^{-1} resolution in a Thermo Scientific Nicolet iS5 Spectrometer. The ultrastructure was evaluated by Transmission Electron Microscopy (TEM-HRTEM) (JEM-2010 JEOL) (200 keV). The 80 cm camera length condition and electron beam transparent particles were selected for area diffraction patterns (SAD) examination.

2.5. The ah-MSCs: isolation, expansion and characterization

The ah-MSCs were isolated from bone marrow of healthy human volunteers by percutaneous aspiration from iliac crest according to previous work [10]. The volunteers accepted and signed previously informed consent. The ah-MSCs were characterized in correspondence to the minimal criteria established by Mesenchymal and Tissue Stem Cell Committee of the International Society for Cellular Therapy [24]. The Institutional Ethics Committee of the University Hospital V. Arrixaca (Murcia, Spain) approved this protocol.

The ah-MSCs were seeded at a density of 5×10^3 cells/cm² in 75 cm² flasks with 10 ml of basal growth medium (GM). The GM was composed by Dulbecco's Modified Eagle Medium (DMEM) with 10% of inactivated fetal bovine serum (FBS) and 1% antibiotics (penicillin/streptomycin 100 U/ml and 100 $\mu\text{g}/\text{ml}$ respectively), all from Sigma-Aldrich, St. Louis, MO, USA. Cell culture was incubated at 37 °C in a 5% CO₂ atmosphere with a 95% of relative humidity, changing GM every 3 days. The expanded cells, passage 3 (P3), were collected for the *in vitro* test.

2.6. In vitro cell test

In vitro adhesion and proliferation of ah-MSCs were assayed on the LS' surface to evaluate material's biocompatibility. Scaffolds were sterilized at 121 °C for 20 min in an autoclave and pre-incubated with 800 μL of FBS for 24 h.

The collected cells (P3) were seeded at a density of 5×10^3 cells/cm² on the scaffolds' surface in 48-well culture plates and incubated at the same conditions described above with 800 μL of GM for 7, 14 and 21 days.

Cell viability and metabolic function of ah-MSCs with the scaffolds were evaluated by Alamar Blue assay (Invitrogen, Carlsbad, CA, USA). After each study period, GM was removed and seeded samples were washed twice with Phosphate Buffer Saline 1x (PBS 1x). Then, they were supplied with 800 μL of new GM containing 10% of Alamar Blue and incubated at 37 °C for 4 h in darkness. After this, 200 μL of the GM with 10% of Alamar Blue reactant were placed into a 96-well plate to fluorescence analysis in Synergy MX ultraviolet visible (UV-Vis) reader (BioTeK Instruments Inc, Winooski, VT, USA). The excitation-emission wavelengths were 560–590 nm respectively.

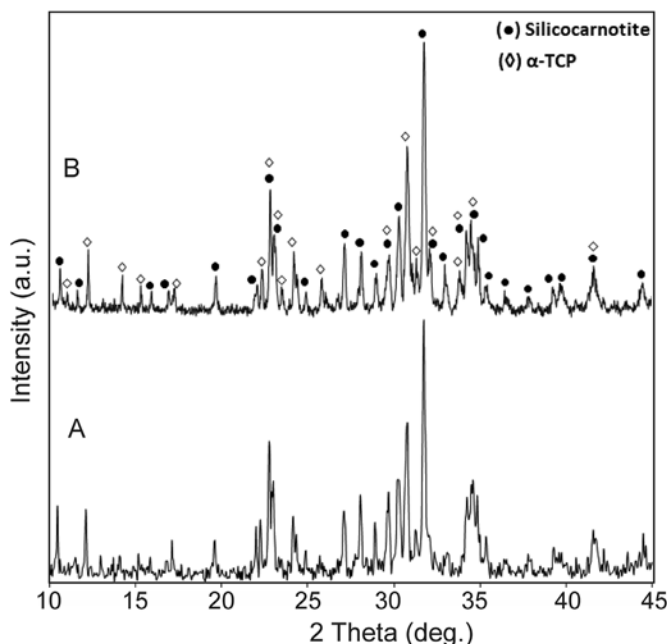


Fig. 1. XRD pattern of (A) the ceramic raw material and (B) LS as a representative one. All peaks correspond to Silicocarnotite (●) and α -TCP (◊).

After each incubation time, cell cultured scaffolds were rinsed with PBS 1x for 10 min and fixed with 3% glutaraldehyde for 1 h. Until post fixation with 1% osmium tetroxide, samples were preserved in a cacodylate buffer at 0.1 M. They were rinsed with PBS and dehydrated in a gradient serie of ethanol solutions (30%, 50%, 70%, 90% and 100% v/v) for critical point drying with liquid CO_2 . Finally, samples were examined by SEM at the same conditions described above.

3. Results

3.1. Scaffolds characterization

The XRD analysis of sintered scaffolds (SS and LS) was performed to determine possible changes in the raw material constituent phases induced by the sintering process. Fig. 1 shows the XRD pattern obtained from LS as a representative one, as well as the XRD pattern of the ceramic raw material for scaffolds processing.

Only two phases were identified in both scaffolds. All diffraction peaks correspond to α -TCP (COD no. 96-210-6195) and Silicocarnotite (COD no.00-073-1181) according to the invariant eutectoid composition of the sub-system $\text{Ca}_3(\text{PO}_4)_2\text{-Ca}_5\text{SiP}_2\text{O}_{12}$ within $\text{Ca}_3(\text{PO}_4)_2\text{-Ca}_2\text{SiO}_4$ system. Furthermore, no changes in the phase relationship of raw material was occurred during sintering process of scaffolds (Fig. 1).

Fig. 2 shows representative SEM micrographs of scaffolds' microstructure at different magnifications before immersion in SBF. Both, SS (Fig. 2A) and LS (Fig. 2B) present a highly interconnected porous network and heterogeneous distributions of macro and micropores. In SS, macropores are in the wide range of 140 to 600 μm and in LS between 370 and 1500 μm .

Fig. 2C shows the surface morphology and the result of EDS corresponding to LS as a representative one. After etching with acetic acid (1%) for 4s, surfaces of both scaffolds showed alternating layers that correspond to an irregular lamellar eutectoid microstructure (Fig. 2D, LS as a representative one).

3.2. In vitro bioactivity test

After *in vitro* bioactivity test of both scaffolds for each soaking time

in SBF, changes in the surface morphology were examined by SEM. Results showed a similar structural change for both: SS (Fig. 3) and LS (Fig. 4). The deposition of first apatite-like spheres was observed at 3 days. EDS compositional analysis confirmed that they were composed by P and Ca. Figs. 3A and 4A show these calcium phosphate spheres on struts surface for both scaffolds, with higher magnifications in Figs. 3E and 4E, where the apatite-like morphology can be observed. At the same time, lamellae corresponding to an irregular eutectoid microstructure start to be distinguished on struts and pore wall surfaces. Lamellar structure formation is due to material reaction in SBF that produces a selective dissolution of one phase. At 7 days spheres increase in number, covering the whole surface of both scaffolds and lamellar structure get more remarkable (Fig. 3B, F and Fig. 4B, F). Areas with a large amount of spheres correspond to those in which the lamellar structure is better defined.

At 14 days (Fig. 3C, G and Fig. 4C, G), the coalescence of spheres formed apatite-like precipitate that grew gradually forming a compact and continuous layer on struts and pore wall surface up to 21 days (Figs. 3D and 4D). Beyond this time, the eutectoid microstructure is no longer visible. Surface microcracks were observed indicating a thick deposition layer (Figs. 3H and 4H). The EDS microanalysis showed that this precipitate was rich in Ca and P without silicon traces. The Ca/P ratio was ~1.54 in average, lower than stoichiometric hydroxyapatite suggesting formation of calcium-deficient hydroxyapatite (CDHA). Due probably to its weight, in some areas this layer detached revealing a porous lamellar microstructure beneath. In the EDS microanalysis of these lamellae, silicon was not detected and Ca/P ratio varied between 1.49 and 1.52.

Fresh fracture from upper and middle part of struts of both scaffolds after 21 days of immersion in SBF were analyzed by ATR-FTIR. Fig. 5 shows the LS' spectra as a representative of all ceramics before and after 21 days in SBF.

Fresh fracture of upper (Fig. 5B) and middle part (Fig. 5C) show some differences compared to the spectrum before immersion in SBF (Fig. 5A) [22]. The absorption peaks at 838 and 870 cm^{-1} , corresponding to ν_1 vibration mode of SiO_4 groups [25,26], were replaced by ν_2 vibration mode of CO_3 groups at 867 and 866 cm^{-1} . Also, new absorption bands of ν_3 vibrational mode of CO_3 groups emerged between 1400 and 1640 cm^{-1} , and $2\nu_3$ band at 2900 cm^{-1} which can be assigned to carbonated hydroxyapatite (CHA) structures [26–29]. Furthermore, new broad bands were observed at a higher wavenumber of the spectra, around 3400 cm^{-1} , corresponds to OH^- groups. One strong band corresponding to ν_3 stretching mode of PO_4 groups were identified at 1015 cm^{-1} , approximately [27]. Other peaks associated to ν_1 stretching mode of PO_4 groups were observed at 943 and 938 cm^{-1} , characteristic of CHA [27].

Changes in Ca, P and Si concentration in SBF after different soaking times were similar for both scaffolds (Fig. 6). Due to material degradation, Ca ions were released from scaffolds to SBF changing the initial concentration of 66.23 mg/L until reaching the maximum at 1 day (72.78 mg/L and 69.83 mg/L for SS and LS respectively). Once apatite begins to precipitate on the scaffolds' surface (from 3 days), Ca concentration decreased in SBF up to 21 days achieving its minimum value (62.73 mg/L and 59.23 mg/L for SS and LS respectively). Consequently, P ions were continually removed from medium changing the initial concentration of 25.98 mg/L until reaching the minimum at 21 days (13.23 mg/L and 17.83 mg/L for SS and LS respectively).

At the same time, Si ions were continuously released from scaffolds to SBF reaching the maximum at 14 days (6.39 mg/L and 3.10 mg/L for SS and LS respectively). This would be due to Silicocarnotite phase dissolution. Subsequently (at 21 days), Si concentration decreased with respect to 14 days. This may be due to part of the Si ions have produced silicon substitutions in the new hydroxyapatite layer lattice. It was impossible to confirm this fact because the quantity of silicon substitution must be below the detection limit of the equipment.

The ultrastructure of product formed on scaffolds surface after

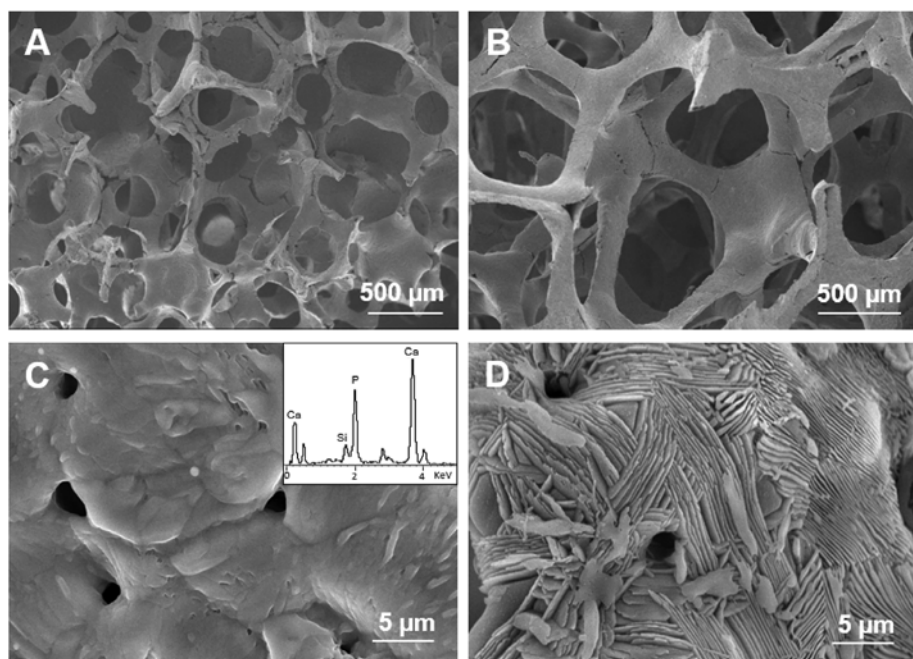


Fig. 2. SEM micrographs of scaffolds' microstructure at different magnification before immersion in SBF: (A) SS, (B) LS, (C) LS' surface morphology and EDS analysis as a representative one and (D) LS' surface morphology after etching with acetic acid (1%).

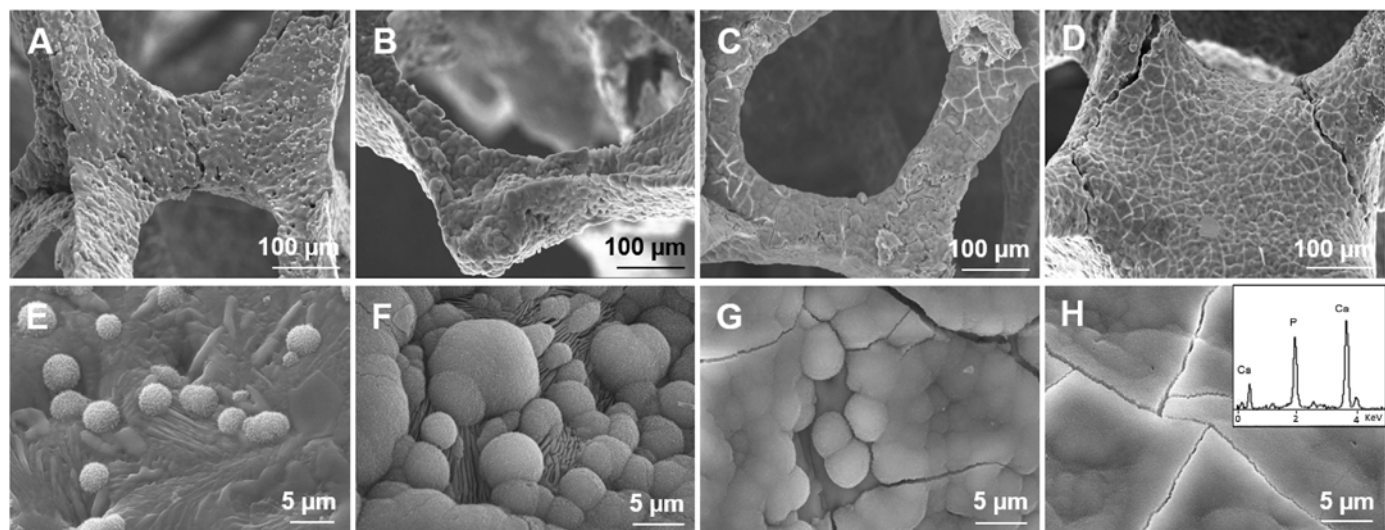


Fig. 3. SEM micrographs at different magnification of SS surface after different soaking times in SBF: (A, E) 3, (B, F) 7, (C, G) 14 and (D, H) 21 days. Surface EDS microanalysis.

different soaking time in SBF was examined by TEM-SAD. Fig. 7 shows TEM-SAD micrographs of removed product from LS surface as a representative of all. SAD at 3 days (Fig. 7B) indicated preferential orientation of hydroxyapatite crystals in (211) and (002) similar to biological apatites [30,31].

However, some diffraction spots corresponding to initial crystalline material are still visible. (211) and (002) arcs become more defined with increase soaking time until 21 days and spots due to starting crystalline material are no more detectable (Fig. 7F). Small individual crystals were observed forming a continuous phase in HRTEM (Fig. 7E). Measured lattice spacing of 0.281 nm and 0.344 nm closely matched with values of CHA reported by previously works [8,9,32].

3.3. In vitro cell test

Material biocompatibility was evaluated through the adhesion and

proliferation capacity of ah-MSCs on the LS' surface. Fig. 8 shows SEM micrographs of the evolution of ah-MSCs seeded on LS' surface after different incubation times in GM.

After 7 days (Fig. 8A-C), individual cells were observed attached by cytoplasmic projections (filopodia). Furthermore, a globular Ca-P-like precipitate appeared and it did not obstruct cell adhesion and proliferation.

After 14 days from cell seeding (Fig. 8D-F), elongated cells were found forming isolated groups, mainly through pores walls and they were establishing close physical contact between them. Even cells were observed throughout the pores of the scaffolds, completely adhered and spreaded out (Fig. 8D).

When incubating time increased to 21 days, cells were covering the whole scaffolds' surface (Fig. 8G-I). The numerous cytoplasmic projections suggest a close contact between cells and scaffolds' surface. In some areas, cells were forming a dense monolayer partially covering the

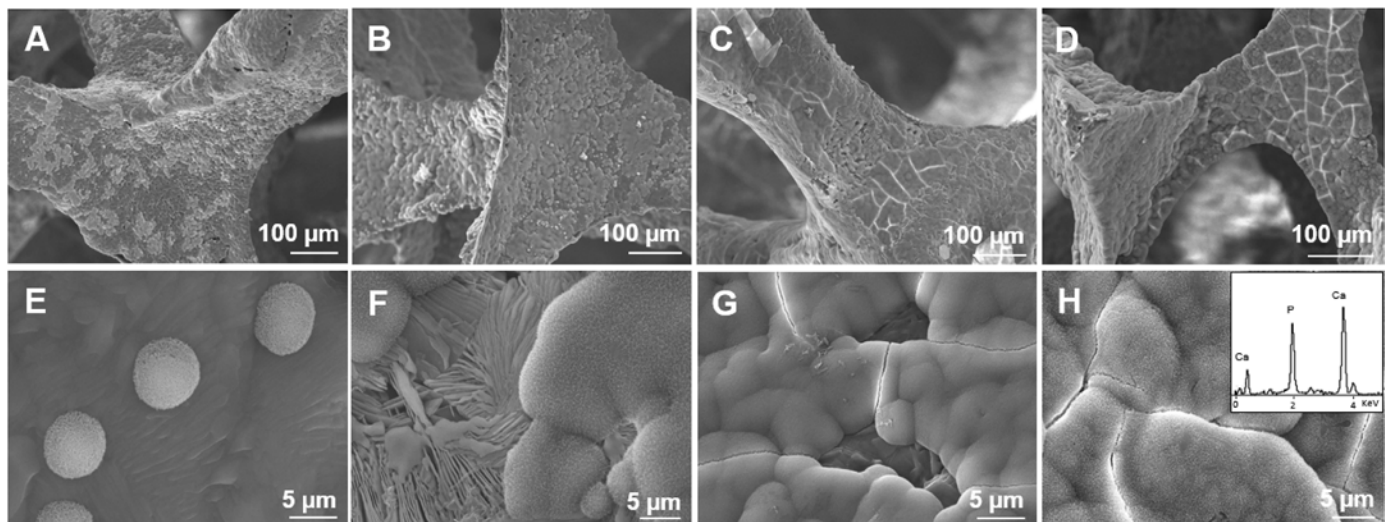


Fig. 4. SEM micrographs at different magnification of LS surface after different soaking times in SBF: (A, E) 3, (B, F) 7, (C, G) 14 and (D, H) 21 days. Surface EDS microanalysis.

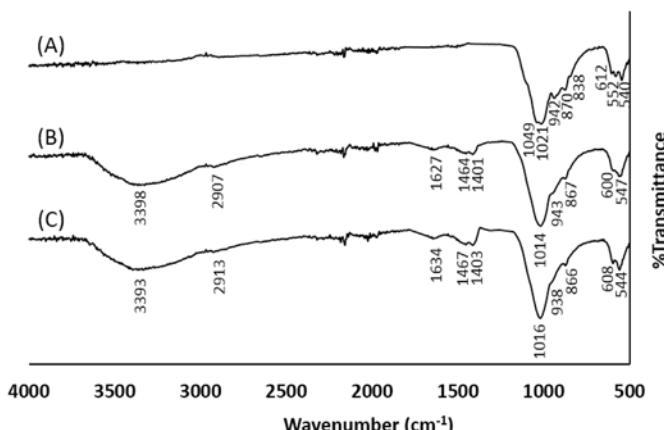


Fig. 5. ATR-FTIR spectra of LS as a representative of all: (A) Before immersion in SBF, (B) fresh fracture of upper and (C) middle part of struts after 21 days of immersion in SBF.

structure. Fig. 8H shows cells crossing a pore through cytoplasmic projections, establishing a wall-to-wall connection.

The number of cells on the scaffolds' surface increased as a function of culture time. Moreover, a fibrillary material together with mineral deposits were observed in some intercellular gaps at 21 days, which suggests the formation of extracellular matrix. Results of Alamar Blue assay confirmed SEM observations. Fig. 9 shows metabolic activity of the ah-MSCs seeded on the scaffolds' surface and on the TCPS (cells positive control).

In both cases, fluorescence tends to increase with the incubation time, which corresponds with an increment in the cellular metabolic activity. Although no significant differences between material and control cells were observed at 14 and 21 days, material cells showed a slightly higher metabolic activity at all study times.

4. Discussion

Researches in bone tissue engineering have increased significantly in the last few years due to a clinical need to find the ideal bone substitute. Main efforts are aimed to development of three-dimensional scaffolds able to induce and support new tissue ingrowth. Currently, biphasic calcium phosphates ceramics are considered as the new gold standard, with properties even superior to autologous bone grafts [3]. A

biphasic material is composed by two phases with different chemical properties and, therefore, different degradation rate. The most soluble phase reacts by rapid ion exchanged with the biological medium, increasing bioactivity and osteoinduction. On the other hand, the most stable phase can act as a guide and three-dimensional support during bone regeneration process.

From this perspective, the aim of this research was to evaluate *in vitro* bioactivity and biocompatibility of new biphasic scaffolds composed by two well defined phases: α -TCP and Silicocarnotite. α -TCP have a similar composition to bone mineral phase, and some authors propose that Si ion substitutions in crystalline structures of TCP improve their biological properties [5–7].

Scaffolds were obtained by polymer replica method from ceramic powders according to the eutectoid invariant point of the corresponding sub-system [21]. Mineralogical analysis by XRD (Fig. 1) confirmed that both scaffolds were only composed of two phases. This means that no change in the raw material constituent was performed during the sintering process.

Fig. 2A y B show a highly interconnected porous network that mimic cancellous bone structure for both scaffolds. One of the most important advantage of polymer replica method is that allows to obtain highly open porous structures with a desire pore size and geometry, allowing the implant adjustment to bone defects requirements. For both scaffolds, macropore size distributions are in the well-defined range compatible with biological requirements for new bone formation and development [33–35]. Surface microporosity (Fig. 2C) can improve ion exchange between scaffolds and the surrounding media due to the increment in the contact surface area. It has also proved that the surface roughness enhances cell adhesion and scaffold osteoinductive properties [36,37].

After etching with acetic acid (Fig. 2D) scaffolds' surface showed a typical irregular eutectoid morphology conformed by alternating lamellae of α -TCP and Silicocarnotite. SEM micrographs looks like lamellar structure of human bone surface reported by others authors [38,39]. This morphology provides additional porosity to scaffolds and allows cells adhesion and bone matrix deposition, with the subsequent new bone formation.

It is well known that ceramics able to induce *in vitro* apatite formation on its surface can bond to living bone without fibrous tissue formation once implanted in a body. In order to estimate the bone-bonding capacity of scaffolds, different soaking times were tested in SBF. Both scaffolds reacted in a similar way by selective dissolution of one phase forming a lamellar microstructure and the subsequent

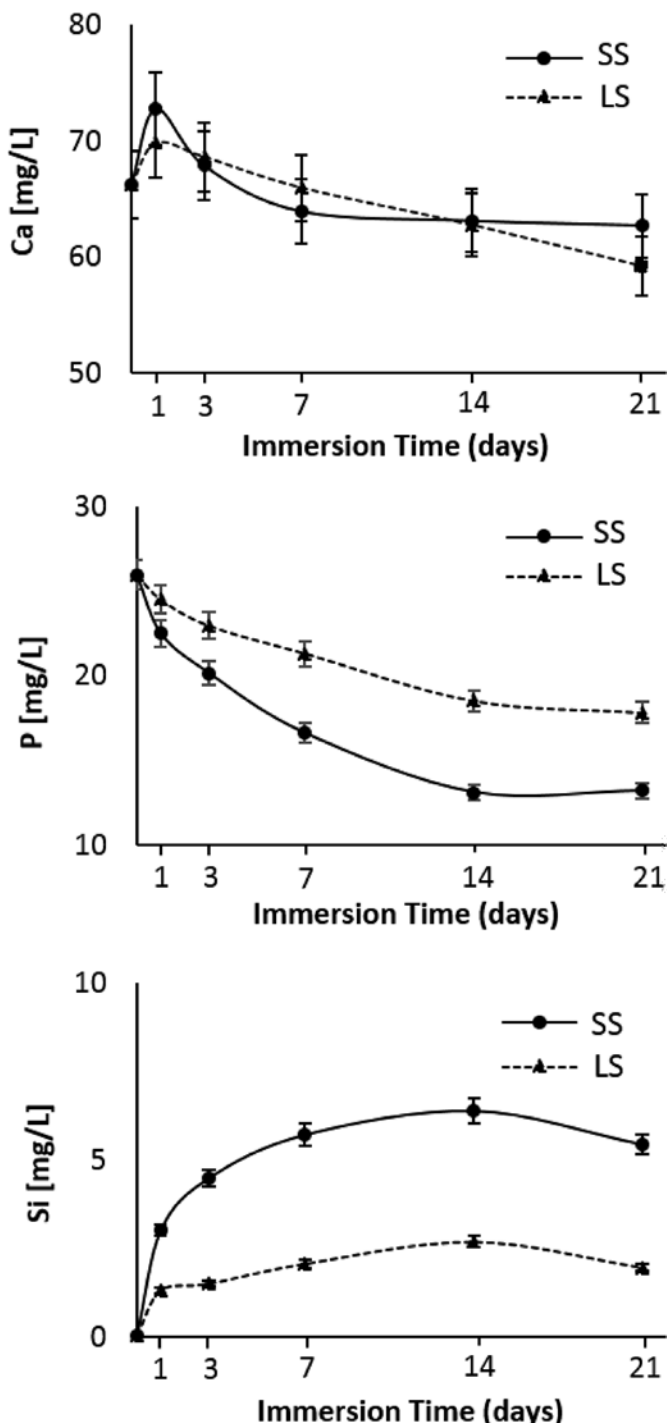


Fig. 6. Changes in Ca, P and Si concentration as a function of SBF immersion time for both scaffolds: SS and LS.

deposition of hydroxyapatite-like layer with a morphology and a Ca/P rate similar to biological hydroxyapatite (Figs. 3 and 4) [40–42]. No significant differences were observed between LS and SS *in vitro* behavior.

Changes observed in the peaks at 838 and 870 cm⁻¹ in FTIR spectra of ceramics after 21 days in SBF, which correspond to silica network (Fig. 5), as well as the continuously Si ions released from samples to SBF (Fig. 6) indicate that Silicocarnotite is the phase that was dissolving. This fact was also confirmed with the analysis of lamellae observed beneath the thick hydroxyapatite layer after 21 days of immersion in SBF. The EDS microanalysis supported that the remaining phase in the

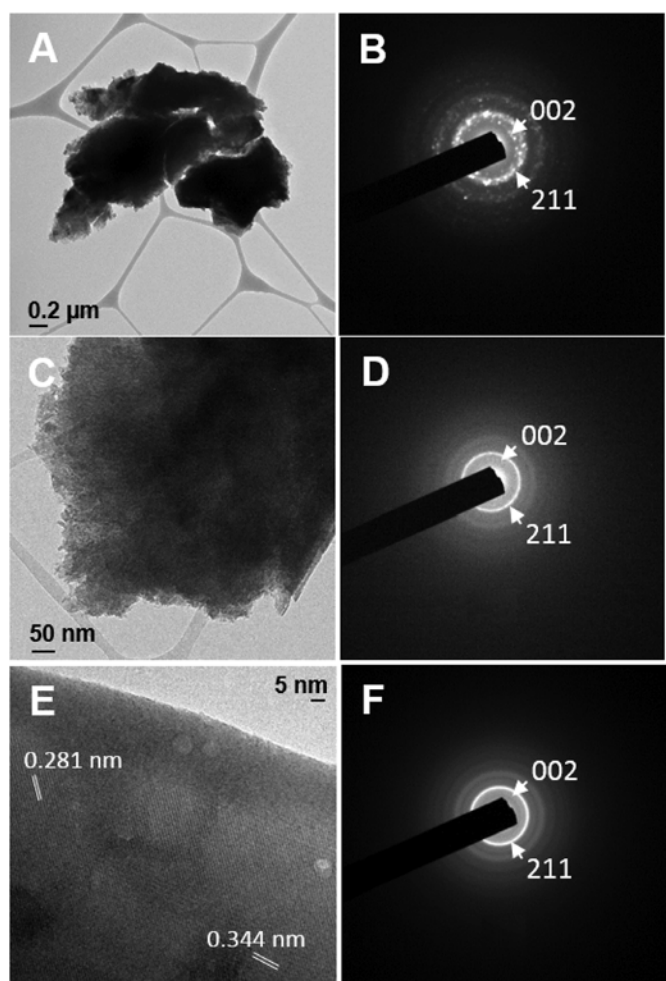


Fig. 7. TEM-SAD micrographs of surface product that formed on scaffolds after different soaking time in SBF: (A, B) 3, (C, D) 7 and (E, F) 21 days.

structure was α -TCP ($1.49 < \text{Ca}/\text{P} < 1.52$ and Si was not detected).

Si ions promote apatite nucleation and crystallization in SBF [41,43] and enhance osteogenic differentiation of stem cells [44]. Therefore the Silicocarnotite phase degradation is capable to induce hydroxyapatite precipitation and stimulate cell response of bone tissue cells, while the most stable phase, α -TCP, can act as three-dimensional support during bone regeneration processes. Deposition of apatite-like precipitate grew gradually with immersion time, forming a compact and continuous layer covering the whole surface.

Overall results of morphological and compositional analysis match with theoretical data for calcium-deficient carbonated hydroxyapatite, similar to bone mineral phase [30,31]. This hydroxyapatite layer will allow a chemical bonding between the implant and the living bone tissue.

The ah-MSCs were able to adhere and proliferate on the LS' surface. High cell colonization was achieved in the whole structure even, inside the scaffolds, forming an extensive monolayer with abundant filopodia. Cells flattened shape indicated no cytotoxicity or morphological alterations induced by the material. Alamar Blue assay confirmed a good cell biological response and metabolic function of ah-MSCs seeded on the top of the material. The fibrillary network and mineral deposits observed at 21 days in the intercellular gaps suggest the formation of extracellular matrix and mineralization nodules.

5. Conclusion

Using a polymer replica method, biphasic scaffolds were obtained

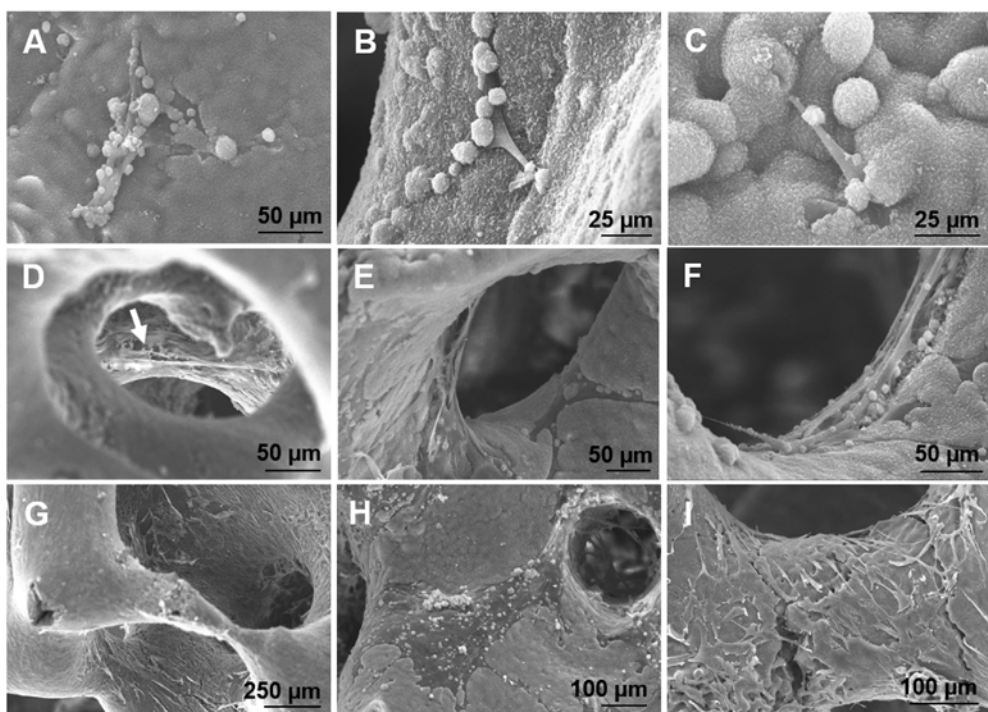


Fig. 8. SEM micrographs of scaffolds' surface seeded with ah-MSCs in GM for: (A–C) 7, (D–F) 14 and (G, I) 21 days.

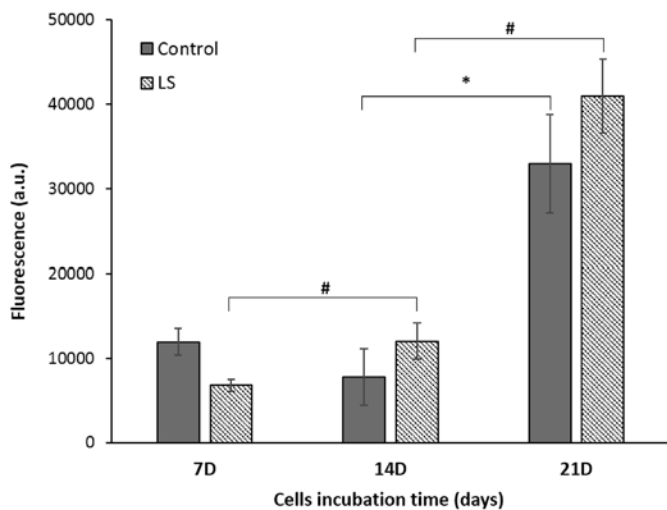


Fig. 9. Results obtained by the Alamar Blue assay of the ah-MSCs seeded on the scaffolds' surface compared to the control cells. # Means significant differences ($p < 0.05$) between the cells seeded on the scaffolds' surface at different study times; and * means significant differences between control cells at different study times.

with macro and microstructure similar to a hierarchical architecture of cancellous bone. Pore size distribution and shape were controlled by polyurethane templates selection. *In vitro*, eutectoid scaffolds reacted dissolving Silicocarnotite phase and forming a bone-like apatite layer on the surface of remain phase within 21 days. Results showed that the bioactivity increases with increasing soaking time in SBF. *In vitro* cell test showed that the scaffolds support ah-MSCs adhesion and proliferation, forming an extensive monolayer at 21 days after cell seeding. The overall results suggest that the scaffolds developed are attractive materials with potential application in bone tissue engineering. Although, more specific cells and *in vivo* studies are needed to prove its potential applicability.

References

- [1] J. Henkel, M.A. Woodruff, D.R. Epari, et al., Bone regeneration based on tissue engineering conceptions—a 21st century perspective, *Bone Res.* 1 (2013) 216–248.
- [2] M. Parent, H. Baradari, E. Champion, et al., Design of calcium phosphate ceramics for drug delivery applications in bone diseases: a review of the parameters affecting the loading and release of the therapeutic substance, *J. Contr. Release* 252 (2017) 1–17.
- [3] J.M. Bouler, P. Pilet, O. Gauthier, et al., Biphasic calcium phosphate ceramics for bone reconstruction: a review of biological response, *Acta Biomater.* 53 (53) (2017) 1–12.
- [4] L. Roseti, V. Parisi, M. Petretta, et al., Scaffolds for bone tissue engineering: state of the art and new perspectives, *Mater. Sci. Eng. C* 78 (2017) 1246–1262.
- [5] A.M. Pietak, M. Sayer, Functional atomic force microscopy investigation of osteopontin affinity for silicon stabilized tricalcium phosphate bioceramic surfaces, *Biomaterials* 27 (2006) 3–14.
- [6] A.M. Pietak, J.W. Reid, M.J. Stott, et al., Silicon substitution in the calcium phosphate bioceramics, *Biomaterials* 28 (2007) 4023–4032.
- [7] G. Fielding, J. Feuerstein, A. Bandyopadhyay, et al., SiO_2 and SrO doped β -TCP: influence of dopants on mechanical and biological properties, *Biomater. Sci.* 237 (2012) 171–181.
- [8] I.M. Martínez, L. Meseguer-Olmo, A. Bernabeu-Eslapez, et al., In vitro behavior of α -tricalcium phosphate doped with dicalcium silicate in the system $\text{Ca}_2\text{SiO}_4\text{-Ca}_3(\text{PO}_4)_2$, *Mater. Char.* 63 (2012) 47–55.
- [9] I.M. Martínez, P. Velásquez, L. Meseguer-Olmo, et al., Preparation and characterization of novel bioactive α -Tricalcium Phosphate doped with Dicalcium Silicate ceramics, *Mater. Sci. Eng. C* 32 (2012) 878–886.
- [10] L. Meseguer-Olmo, S. Aznar-Cervantes, P. Mazón, et al., “In vitro” behavior of adult mesenchymal stem cells of human bone marrow origin seeded on a novel bioactive ceramic in the $\text{Ca}_2\text{SiO}_4\text{-Ca}_3(\text{PO}_4)_2$ system, *J. Mater. Sci. Mater. Med.* 23 (2012) 3003–3014.
- [11] P. Ros-Tárraga, P. Mazón, M.A. Rodríguez, et al., Novel resorbable and osteoconductive calcium silicophosphate scaffold induced bone formation, *Materials* 9 (2016) 785.
- [12] S.M. Giannitelli, F. Basoli, P. Mozetic, et al., Graded porous polyurethane foam: a potential scaffold for oro-maxillary bone regeneration, *Mater. Sci. Eng. C* 51 (2015) 329–335.
- [13] P. Ros-Tárraga, A. Murciano, P. Mazón, et al., New 3D stratified Si-Ca-P porous scaffolds obtained by sol-gel and polymer replica method: microstructural, mineralogical and chemical characterization, *Ceram. Int.* 43 (2017) 6548–6553.
- [14] P. Ros-Tárraga, A. Murciano, P. Mazón, et al., In vitro behavior of sol-gel interconnected porous scaffolds of doped wollastonite, *Ceram. Int.* 43 (2017) 11034–11038.
- [15] I. Sopyan, J. Kaur, Preparation and characterization of porous hydroxyapatite through polymeric sponge method, *Ceram. Int.* 35 (2009) 3161–3168.
- [16] C. Wang, H. Chen, X. Zhu, et al., An improved polymeric sponge replication method for biomedical porous titanium scaffolds, *Mater. Sci. Eng. C* 70 (2017) 1192–1199.
- [17] C. Dhand, S.T. Ong, N. Dwivedi, et al., Bio-inspired in situ crosslinking and

- mineralization of electrospun collagen scaffolds for bone tissue engineering, *Biomaterials* 104 (2016) 323–338.
- [18] K.M. Sajesh, K. Kiran, S.V. Nair, et al., Sequential layer-by-layer electrospinning of nano SrCO₃/PRP loaded PHBV fibrous scaffold for bone tissue engineering, *Compos. B Eng.* 99 (2016) 445–452.
- [19] N.J. Castro, J. O'Brien, L.G. Zhang, Integrating biologically inspired nanomaterials and table-top stereolithography for 3D printed biomimetic osteochondral scaffolds, *Nanoscale* 7 (2015) 14010–14022.
- [20] W. Xiao, M.A. Zaeem, B.S. Bal, et al., Creation of bioactive glass (13–93) scaffolds for structural bone repair using a combined finite element modeling and rapid prototyping approach, *Mater. Sci. Eng. C* 68 (2016) 651–662.
- [21] I.M. Martínez, P.A. Velásquez, P.N. De Aza, The sub-system a-TCPss-silicocarnotite within the binary system Ca₃(PO₄)₂–Ca₂SiO₄, *J. Am. Ceram. Soc.* 95 (2012) 1112–1117.
- [22] A. Díaz-Arca, P. Mazón, P.N. De Aza, Eutectoid scaffold as potential tissue engineer guide, *J. Am. Ceram. Soc.* 102 (2019) 7168–7177.
- [23] T. Kokubo, H. Takadama, How useful is SBF in predicting *in vivo* bone bioactivity? *Biomaterials* 27 (2006) 2907–2915.
- [24] M. Domínguez, K. Le Blanc, I. Mueller, et al., Minimal criteria for defining multipotent mesenchymal stromal cells. The international society for cellular therapy position statement, *Cytotherapy* 8 (2006) 315–317.
- [25] S. Serena, M.A. Sainz, A. Caballero, Single-phase silicocarnotite synthesis in the subsystem Ca₃(PO₄)₂–Ca₂SiO₄, *Ceram. Int.* 40 (2014) 8245–8252.
- [26] S. Serena, A. Caballero, P.N. De Aza, et al., New evaluation of the *in vitro* response of silicocarnotite monophasic material, *Ceram. Int.* 41 (2015) 9411–9419.
- [27] A. Antonakos, E. Liarokapis, T. Leventouri, Micro-Raman and FTIR studies of synthetic and natural apatites, *Biomaterials* 28 (2007) 3043–3054.
- [28] I. Rehman, W. Bonfield, Characterization of hydroxyapatite and carbonated apatite by photo acoustic FTIR spectroscopy, *J. Mater. Sci. Mater. Med.* 8 (1997) 1–4.
- [29] R. Yilmén, U. Jäglid, Carbonation of portland cement studied by diffuse reflection fourier transform infrared spectroscopy, *Int. J. Concr. Struct. Mater.* 7 (2013) 119–125.
- [30] X. Su, K. Sun, F.Z. Cui, et al., Organization of apatite crystals in human woven bone, *Bone* 32 (2003) 150–162.
- [31] B. Kerebel, G. Daculsi, A. Verbaere, High-resolution electron microscopy and crystallographic study of some biological apatites, *J. Ultrastruct. Res.* 57 (1976) 266–275.
- [32] V. Rubio, P. Mazón, M.A. De la Casa Lillo, et al., Preparation, characterization and *in vitro* behavior of a new eutectoid bioceramic, *J. Eur. Ceram. Soc.* 35 (2015) 317–328.
- [33] H. Rehman, Z. Miqin, Preparation of porous hydroxyapatite scaffolds by combination of the gel-casting and polymer sponge methods, *Biomaterials* 24 (2003) 3293–3302.
- [34] S.F. Hulbert, S.J. Morrison, J.J. Klawitter, Tissue reaction to three ceramics of porous and non-porous structures, *J. Biomed. Mater. Res.* 6 (1972) 347–374.
- [35] T.J. Flatley, K.L. Lynch, M. Benson, Tissue response to implant of calcium phosphate ceramic in the rabbit spine, *Clin. Orthop. Relat. Res.* 179 (1983) 246–252.
- [36] J.A. Sanz-Herrera, M. Doblaré, J.M. García-Aznar, Scaffold microarchitecture determines internal bone directional growth structure: a numerical study, *J. Biomech.* 43 (2010) 2480–2486.
- [37] U. Rüdrich, M. Lasgorceix, E. Champion, et al., Pre-osteoblast cell colonization of porous silicon substituted hydroxyapatite bioceramics: influence of microporosity and macropore design, *Mater. Sci. Eng. C* 97 (2019) 510–528.
- [38] A. Boyde, M.H. Hobdell, Scanning electron microscopy of lamellar bone, *Z. Zellforsch. Microsk. Anat. Histochem.* 93 (1968) 213–231.
- [39] A. Boyde, M.H. Hobdell, Scanning electron microscopy of primary membrane bone, *Z. Zellforsch. Microsk. Anat. Histochem.* 99 (1969) 98–108.
- [40] T. Kokubo, S. Ito, T. Huang, et al., Ca, P-rich layer formed on high-strength bioactive glass-ceramic A–W, *J. Biomed. Mater. Res.* 24 (1990) 331–343.
- [41] P. Li, K. Nakanishi, T. Kokubo, et al., Induction and morphology of hydroxyapatite, precipitated from metastable simulated body fluids on sol-gel prepared silica, *Biomaterials* 14 (1993) 963–968.
- [42] I.M. Martínez, P. Velásquez, L. Messeguer-Olmo, et al., Production and study of *in vitro* behavior of monolithic α-tricalcium phosphate based ceramics in the system Ca₃(PO₄)₂–Ca₂SiO₄, *Ceram. Int.* 37 (2011) 2527–2535.
- [43] P. Li, C. Ohtsuki, T. Kokubo, et al., Apatite formation induced by silica gel in a simulated body fluid, *J. Am. Ceram. Soc.* 75 (1992) 2094–2097.
- [44] P. Han, C. Wu, Y. Xiao, The effect of silicate ions on proliferation, osteogenic differentiation and cell signaling pathways (WNT and SHH) of bone marrow stromal cells, *Biomater. Sci.* 1 (2003) 379–392.

9.3. Artículo 3

Rightslink® by Copyright Clearance Center



RightsLink®

Home

Help

Email Support

Sign in

Create Account



Mechanism of in vitro reaction of a new scaffold ceramic similar to porous bone

Author: A. Díaz-Arca, P. Velasquez, P. Mazón, P.N. De Aza

Publication: Journal of the European Ceramic Society

Publisher: Elsevier

Date: May 2020

© 2020 Elsevier Ltd. All rights reserved.

Journal Author Rights

Please note that, as the author of this Elsevier article, you retain the right to include it in a thesis or dissertation, provided it is not published commercially. Permission is not required, but please ensure that you reference the journal as the original source. For more information on this and on your other retained rights, please visit: <https://www.elsevier.com/about/our-business/policies/copyright#Author-rights>

BACK

CLOSE WINDOW

© 2021 Copyright - All Rights Reserved | [Copyright Clearance Center, Inc.](#) | [Privacy statement](#) | [Terms and Conditions](#)
Comments? We would like to hear from you. E-mail us at customercare@copyright.com



Journal of the European Ceramic Society

journal homepage: www.elsevier.com/locate/jeurceramsoc



Original Article

Mechanism of *in vitro* reaction of a new scaffold ceramic similar to porous bone

A. Díaz-Arca, P. Velasquez, P. Mazón, P.N. De Aza*

Instituto de Bioingeniería, Universidad Miguel Hernández, 03202, Elche, Alicante, Spain

ARTICLE INFO

Keywords:
Bioceramics
Tricalcium phosphate
Silicocarnotite
Bioactivity
In vitro mechanism
Biomedical applications

ABSTRACT

A new way of obtaining bioactive and biodegradable 3D scaffold ceramics is presented with possible bone tissue engineering requests. This implies achieving eutectoid structures from certain systems by considering the different conduct of phases. In this study, the silicocarnotite-tricalcium phosphate subsystem was selected because silicocarnotite is bioactive and tricalcium phosphate is biodegradable. A biphasic porous calcium silicophosphate scaffold with high porosity and an interconnected macro- and micropores structure is presented. The scaffold's morphology shows a eutectoid lamellae-type microstructure formed of alternating silicocarnotite and α -tricalcium phosphate layers. The eutectoid scaffold material, when placed in simulated body fluid, responds firstly by dissolving the silicocarnotite phase and then developing a hydroxyapatite microporous structure by pseudomorphic transformation of α -tricalcium phosphate lamellae. The achieved microstructure is like that of porous bone. Afterwards, Si-hydroxyapatite precipitation formed a layer on the scaffold surface by plugging the microporous structure and maintaining the scaffold's 3D structure intact.

1. Introduction

Today's bioceramics tendency is to substitute replacement tissues for regenerating tissues, also called as third-generation biomaterials [1,2]. This category involves the bioactive and resorbable material behaviours to converge in order to stimulate specific cellular responses in molecular terms [3,4]. Tricalcium phosphate (C3P) and hydroxyapatite (HAp) are the well-known calcium phosphates (CaP) that are biologically active and osteoconductive [5,6]. It has been evidenced that adding ions to CaP, e.g. magnesium, silicates, carbonates, sodium, among others, improves the mechanical and biological performance of these new materials with which to develop third-generation ceramics [7,8]. According to some authors, the fact that these ions are present in the physiological environment allows cellular responses to be stimulated, which enhances calcification, metabolism and bone mineralisation processes [9–11].

Phosphate-based materials like HA and β -TCP offer excellent osteoconductivity and biocompatibility. On the one hand, low mechanical properties and unsuitable degradation rates, like low fracture toughness, or no capabilities to improve *in vitro* cell differentiation and to stimulate *in vivo* bone regeneration, restrict further clinical applications with them [12,13]. On the other hand, silicate-based materials can offer good mechanical strength, excellent bioactivity, apt degradation rates

and acceptable durability [14,15].

Ceramics, glasses and glass-ceramics made from combinations of $\text{SiO}_2\text{-CaO-P}_2\text{O}_5$ have been demonstrated to improve cell infiltration, apatite formation and osteogenic differentiation, and also in Si-HA and Si-TCP and silicate-based biomaterials [16–19].

The biomaterials to be used in tissue engineering must strike an optimum balance between bioactivity and biodegradability. If, on the one hand, the material degrades too soon, it does not allow time for the new tissue to regenerate. If, on the other hand, it takes too long to degrade, the tissue is already regenerated and the biomaterial no longer needs to be present.

The bioactive ceramics displaying apatite mineralisation imply a better integration of biomaterials with host bone tissue and enhance osteoblastic activity [20,21]. Sufficient bonding at the tissue-biomaterial interface should also be ensured [22,23]. Neovascularisation is another main factor required for bone regeneration, thus the biomaterial should result in quick vascular ingrowth for better bone integration [24,25]. This is achieved with adequate porosity, and both macro- and microporosity are necessary. However, the main problem in this case is low mechanical properties.

To meet all the above-mentioned needs, the material should be formed with at least two phases: a bioactive one and a biodegradable one. By bearing in mind the bone tissue structure, the most suitable

* Corresponding author.

E-mail addresses: anabel.diaz@goumh.umh.es (A. Díaz-Arca), pavelasquez@umh.es (P. Velasquez), pamazon@umh.es (P. Mazón), piedad@umh.es (P.N. De Aza).

microstructure to be conceived is an irregular lamellar eutectoid microstructure because it becomes comparable to porous bone when one of the phases dissolves [26].

After considering all these points and seeking all the potential binary systems that can fulfil the previously referred conditions, the silicocarnotite-tricalcium phosphate subsystem was selected and investigated [27]. Silicocarnotite, a simple-chain calcium silicate ($5\text{CaOP}_2\text{O}_5\text{SiO}_2$), is bioactive [28] and tricalcium phosphate ($3\text{CaOP}_2\text{O}_5$) is biodegradable [29,30]. In order to produce a 3D scaffold with a microstructure similar to bone, the composition belonging to the invariant point was selected because it presents a lamellae-type eutectoid microstructure composed of alternating silicocarnotite and α -TCP layers. A mechanism of *in vitro* bioactivity is proposed.

2. Materials and methods

The silicocarnotite and α -tricalcium phosphate ceramic powders prepared at the Bioengineering Institute (Spain) were used to manufacture the 3D scaffold. An explanation of the preparation and characterisation of these ceramic powders has been submitted elsewhere [31,32]. Based on the processing parameters established in a previous publication [33], polyurethane sponges with the desired pore size and geometry (5 mm diameter, 3 mm long) were used as templates, which were impregnated with ceramic slurry: 60 % solid content of 53.4 wt% Silicocarnotite and 46.6 wt% α -tricalcium phosphate.

The micro- and macrostructure of scaffolds were characterised by Scanning Electron Microscopy in a SEM-Hitachi S-3500 N device with an Energy-Dispersive X-Ray Spectroscopy (EDX-INCA, Oxford Instruments Analytical, UK) to coat specimens with palladium using a JEOL JEE-400 vacuum evaporator.

In order to qualitatively establish the different crystalline phases formed after applying heat treatment to the scaffold, an X-Ray Diffraction (XRD) analysis was run. The 3D ceramic scaffolds were crushed down to 65 μm , and an X-Ray Bruker-AXS D8 Advance automated diffractometer was used with monochromatic $\text{CuK}_{\alpha}1.2$ radiation (1.541874 Å). Data were obtained by the Bragg-Brentano ($0/20$) vertical geometry from 10° to 60° (20) and in 0.02° steps by counting 20 s/step. The X-ray tube ran at both 40 kV and 30 mA. The Rietveld analysis of the XRD patterns was executed by employing the Power Diffraction Match! 3 version 33.6.2.121 software and the database supplied by the Crystallography Open Database (COD).

The *in vitro* bioactivity of the 3D ceramic scaffolds, reflected by their capability to induce calcium phosphate formation, was investigated by immersion in an acellular simulated body fluid SBF, according to Standard ISO/FDIS 23317:2007 for ceramics and powder samples [34]. The sintered 3D ceramic scaffolds were submerged in 50 ml of SBF with ion composition shown in Table 1, in polyethylene bottles at the human body temperature (37°C), pH 7.4 and atmospheric pressure. The submerged cycles changed from 1 day to 21 days. Changes in ionic concentration were determined by inductively coupled plasma atomic emission spectroscopy (ICP-OES Perkin-Elmer Optima 2000). At regular time points, scaffolds were extracted from SBF and studied by SEM-EDX

3. Results

Fig. 1A shows a highly porous (pore size ~ 140 – $600\text{ }\mu\text{m}$ and porosity $\sim 96\text{ \%}$) scaffold with some broken struts. The microstructure of

the chemical-etched scaffold (etched with 1 % dilute acetic acid for 4 s) is shown in Fig. 1B and C. The rampart microstructure topography comprises homogeneous micropores (medium size of 5 μm) and a laminar feature. If examined close up (Fig. 1C), it is possible to see a lamellar feature made up of alternating lamellae with a characteristic irregular lamellar eutectoid structure. The EDS microanalysis indicated that the phase eliminated by chemical etching was α -C3P, and that detected corresponded to silicocarnotite (with an Si/P ratio of 0.12 and a Ca/P ratio of 2.38), and to the stoichiometric ratios of silicocarnotite (0.5 and 2.5, respectively) and the Ca/P ratio of the stoichiometric C3P of 1.50.

Fig. 2 shows the XRD analysis of the manufactured 3D ceramic scaffolds, which was performed to determine possible mineralogical changes after applying the raw materials to heat treatment. Silicocarnotite was identified as the main phase in scaffolds (53.6 wt%) and α -C3P was identified as the secondary phase (46.4 wt%), which came very close to the eutectoid 53.4/46.6 invariant point [19]. No additional phases were observed.

Fig. 3 shows the surface morphologies of the scaffold before (Fig. 3A-B) and after 1 and 3 soaking days in SBF (Fig. 3C-D and E-F). The surface topography of the walls of the scaffold struts before and after 1 day of soaking is similar, and open micropores cover the whole surface. The lamellar microstructure of scaffolds was sensed after 1 day of soaking (Fig. 3C-D), which was fully revealed after 3 days of soaking (Fig. 3 E-F). This was probably due to the reaction of the scaffold surface with SBF causing the selective dissolution of one of the phases forming the lamellae of the eutectoid scaffold, as well as the subsequent apatite lamellae development by a pseudomorphic conversion of silicocarnotite or the α -C3P phase. This was established by SEM-EDX microanalyses, which displayed a microporous lamellae morphology after 3 days of soaking with an average composition of 61.81 atm% Ca, 38.19 atm% P, and Si was not detected.

As the assay continued, the scaffold's lamellar microstructure was not totally coated by the Ca-P globose particles, whose average size was smaller than 5 μm (Fig. 4A and B). These globular particles are formed by a vast quantity of small worm-like crystals with crystallite dimensions of about 400–500 nm long and 150 nm in diameter (Fig. 4B) which, in some areas, were introduced into the gaps left by the dissolution of one of the scaffold phases (see the arrow in Fig. 4B). The SEM-EDX microanalysis determined that the small globular particles were constituted by phosphorus calcium and silica, while in the porous lamella silica was not detected (Table 2).

This morphology did not further change with soaking times, but did after extended soaking periods (14 and 21 days). The Ca-P globose became bigger, with a final average diameter of $\sim 30\text{ }\mu\text{m}$, and was linked as a compact and larger dense layer (Fig. 4C-E). Consequently, the initial scaffold microstructure was entirely transformed (Fig. 1). Some microcracks were also detected on the scaffold surfaces triggered by the shrinkage of the air-dried samples, implying the development of a thick deposition layer. In some areas, the layer was so thick that it fell down, probably due to its weight (Fig. 4C and D). A detail of the crystalline nature of the new Ca-P precipitate layer is shown in Fig. 4E. Thus struts revealed a lamellar microstructure below the Ca-P precipitate layer, as shown in Fig. 4D. However, the observed lamellar morphology was not the same as the original one. EDX determined that silicon was not present in the lamellar morphology. EDX indicated minor silicon substitution on the new apatite layer (Table 2).

A broken scaffold strut after 21 soaking days in SBF is shown in Fig. 5. The microstructural study indicated the development of two clear consecutive structures at the interface. The creation of a new dense apatite layer was detected on the SBF-scaffold boundary. On average, the layer (about $7 \pm 0.05\text{ }\mu\text{m}$ thick) consisted of 57.72 atm% Ca, 39.60 atm% P, 2.69 atm% Si, and presented less silicon and calcium than the original sample ($\text{Ca}/(\text{P} + \text{Si}) = 1.36$). A porous apatite of a lamellar microstructure lay beneath the dense precipitated apatite layer, which lay in parallel to the scaffold's boundary, constituted by

Table 1
SBF ion concentration.

Ion concentration of SBF in 10^{-3} mol							
Na ⁺	K ⁺	Mg ²⁺	Ca ²⁺	Cl ⁻	HCO ₃ ⁻	HPO ₄ ²⁻	SO ₄ ²⁻
142	5.0	1.5	2.5	147.8	4.2	1.0	0.5

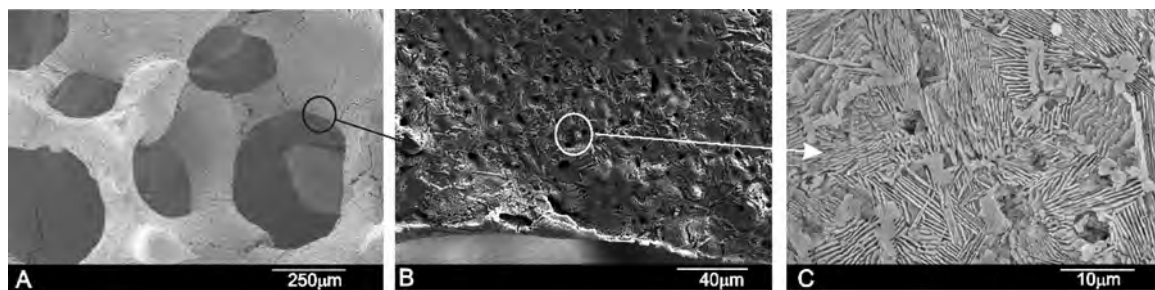


Fig. 1. SEM micrographs of the (A) ceramic scaffold; (B) detail of the strut; (C) irregular lamellar microstructure.

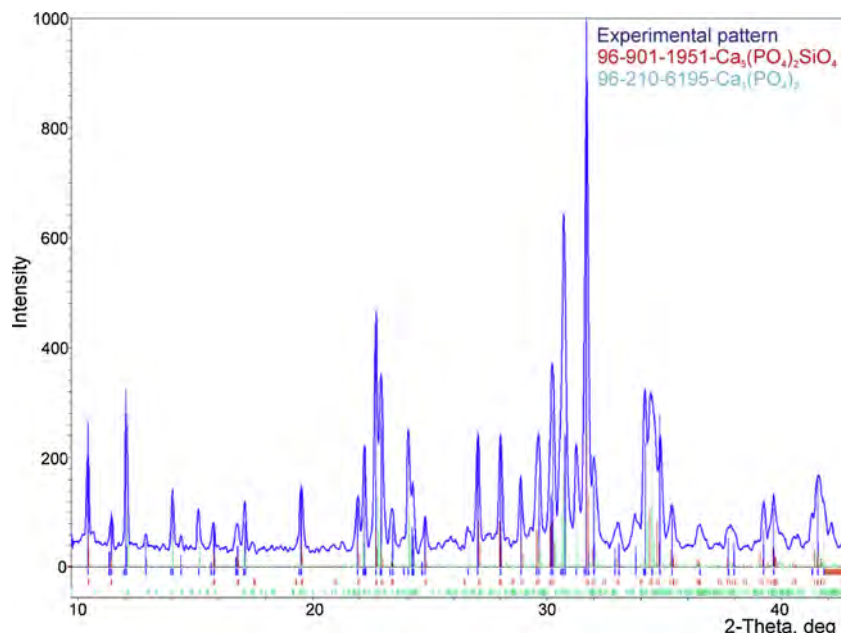


Fig. 2. XRD of the 3D scaffold ceramic scaffold after heating and milling.

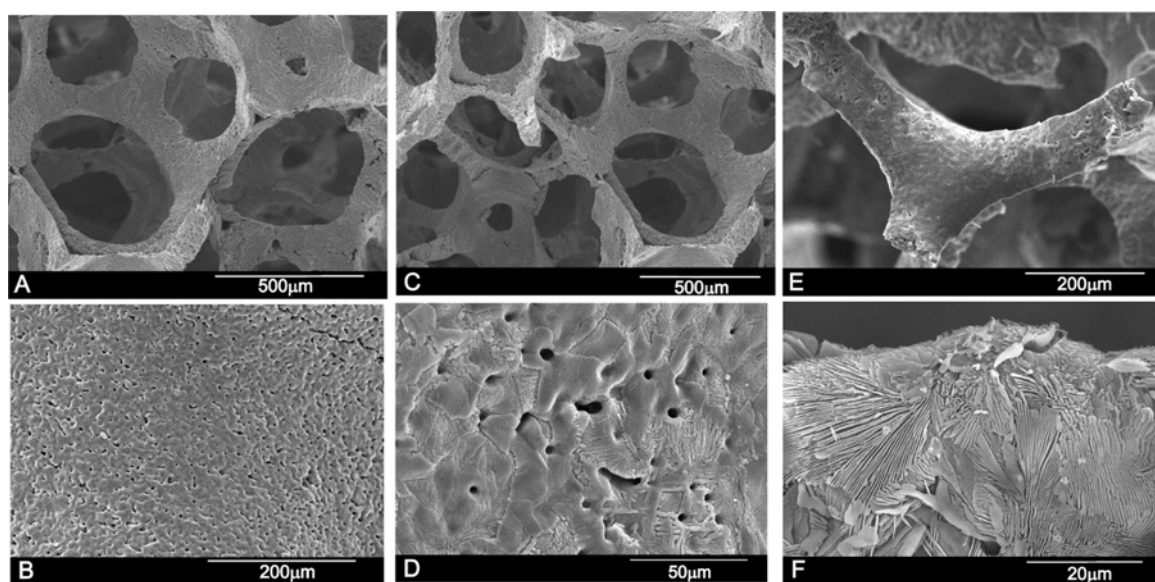


Fig. 3. Low and High SEM micrographs of the ceramic scaffold after (A,B) 0 day, (C,D) 1 day, (E,F) 3 days of soaking in SBF.

dissolution of silicocarnotite or the α -C3P phase, which constituted the original scaffold ($1.74 \leq \text{Ca/P} \leq 2.40$).

The monitoring of the calcium, phosphorous and silicon ion concentrations is presented in Fig. 6. After 1 day of soaking, calcium and

silicon significantly increased (69.83 and 1.32 mg/L, respectively), and then calcium slightly decreased at a constant rate of ~ 0.62 mg/day. The phosphorous ion concentration also constantly diminished at a rate of ~ 0.39 mg/day throughout the assay.

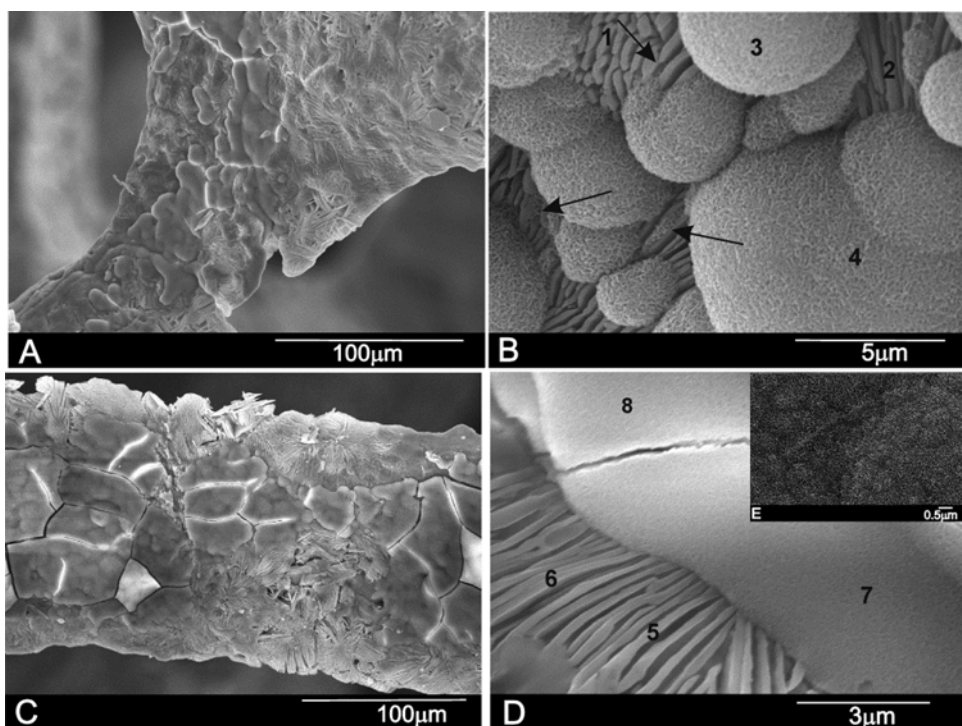


Fig. 4. SEM micrographs of the ceramic scaffold after (A,B) 7 days (arrows indicate the places where the gap left by the dissolution of one of the phases is filled by the new globular precipitate), (C–E) 14 days and the EDS microanalysis taken from points 1–8 and displayed in Table 2.

Table 2
The EDS microanalysis taken from Fig. 4.

EDS microanalysis points								
Atomic %	1	2	3	4	5	6	7	8
Ca	63.55	65.34	60.07	58.99	68.62	70.62	58.84	58.45
P	36.45	34.66	39.15	40.15	31.38	29.38	39.79	39.72
Si	–	–	0.78	0.86	–	–	1.37	1.83

4. Discussion

It is evident from the results in the previous section that the ceramic scaffold showed strong *in vitro* bioactivity and biodegradability behaviour in SBF.

After soaking the eutectoid scaffold in SBF, two different reactions took part on the scaffold surface. The recorded variations in the calcium, phosphorous and silicon ion concentrations (Fig. 6) revealed that the scaffold released Ca and Si ions throughout the first soaking time. A considerable rise in the silicon concentration, at a rate of ~0.19 mg/

day, took place on the first 14 days of soaking. The constant Si ion dissolution from the scaffold resulted in a higher Si ion concentration in SBF. This implies that the dissolving phase contained a large amount of silicon. Consequently, this would be silicocarnotite. Silicocarnotite dissolution in SBF is supported by the P_2O_5 - SiO_2 - CaO - H_2O phase diagram, in which silicocarnotite is unstable in the presence of water [35–37]. Degradation of the silicocarnotite phase controlled the creation of a porous reaction zone of $\sim 50 \pm 1.05 \mu m$ in width after 21 days of soaking (Fig. 5 as being representative of the whole fresh fracture). Thus we can state first of all, SBF reacted with the scaffold to produce silicocarnotite dissolution and the rear formation of apatite lamellae by the pseudomorphic switching of α -C3P (Fig. 3).

In a second step, apatite precipitation took place in globular form on the scaffold surface. Apatite precipitation was less copious at the beginning of the reaction (Fig. 4A), but turned into a heavy dense layer towards the end of the reaction to cover the whole scaffold surface (Figs. 4B and 5). Throughout the second soaking step, approximately as from day 7, the concentration of the Ca ions in SBF lowered to 59.23 ± 0.03 mg, which is attributable to the precipitation of an apatite layer on the scaffold surface (Figs. 4 and 5). The P concentration

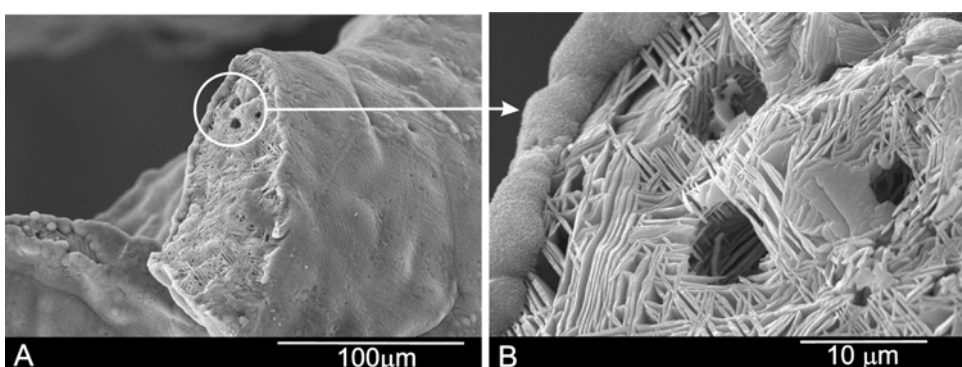


Fig. 5. SEM micrographs of a broken scaffold strut after 21 days of soaking in SBF.

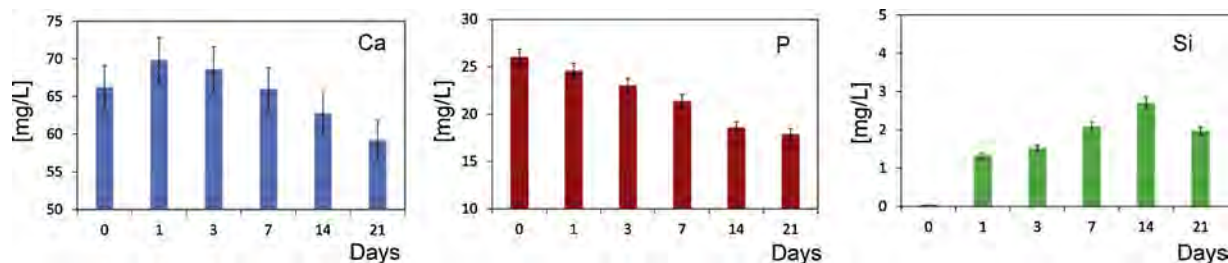
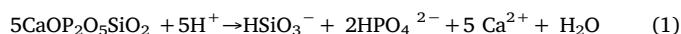


Fig. 6. Changes in the calcium, phosphorous and silicon ion concentrations during the SBF assay.

also lowered (17.83 ± 0.06 mg over 21 days). This reduction that took place up to 21 SBF soaking days was also noticeable due to an apatite layer of about 7 ± 0.05 µm thickness developing (Fig. 5). In the first reaction stages, the elevated Ca concentration in SBF (Fig. 6) improved the subsequent nucleation of the Si co-substituted apatite layer on the scaffold surface. The EDS microanalyses shown in Table 2 provide data on the Ca/P and Ca/(P + Si) ratio calculations for the new Si co-substituted apatite layer, and on the apatite transformation of the scaffold according to soaking times.

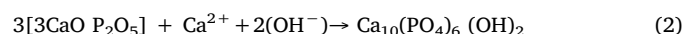
The fact that successive variations occurred in the ion concentrations in SBF suggests that the diffusion process of ions took place via the pores in the porous reaction zone generated through the degradation of the silicocarnotite phase on the scaffold-SBF boundary (Fig. 5). This explains why the Si content in SBF continued to rise after 14 soaking days (Fig. 6). During the last week, Si slightly lowered, which could be due to the diffusion processes of Si ions through the new Si co-substituted apatite layer becoming very hard or because the precipitate employs a considerable amount of Si to develop a very thick Si co-substituted apatite layer.

The evidence herein found can be described by the subsequent multiple mechanism (Fig. 7). In the proposed mechanism, when the *in vitro* assay commenced, two practically synchronised reactions occurred. Firstly, the silicocarnotite phase that was in contact with SBF started reacting by the ionic exchange of the Ca^{2+} contained in the silicocarnotite network for H_3O^+ from SBF (Eq. (1)). This reaction started at the periphery of the scaffold, and released Ca and Si ions into SBF. The reaction continued inwardly through the narrow channels among the $\alpha\text{-C3P}$ lamellae as silicocarnotite was dissolved (Fig. 7A). This reaction generated the subsequent steps:

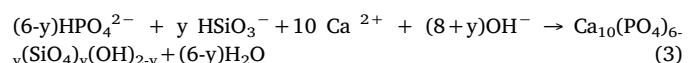


The $\alpha\text{-C3P}$ lamellae immediately started to react with the Ca^{2+} and

$2(\text{OH}^-)$ ions present in the narrow channels. Consequently a pseudomorphic transformation of the $\alpha\text{-C3P}$ lamellae took place through Eq. (2) (Fig. 7B).



The Ca and Si ions dissolved from the silicocarnotite lamellae and not implicated in the reaction moved towards SBF away from the interface and produced a large amount of the Si^{4+} ion concentration in the SBF solution and a small amount of Ca^{2+} (Fig. 6). As no significant increase in Ca ions was detected (Fig. 6 day 3 onwards), most of the Ca^{2+} had to react with the phosphorous of SBF at the scaffold-SBF interface and the precipitation of Si co-substituted HA started in the external scaffold zone (Fig. 7C), which agrees with Eq. (3).



Precipitation took place in the recently formed apatite lamellae (Figs. 3–5), and somewhat penetrated between the pores left by silicocarnotite when it dissolved (Fig. 4A, arrows). Furthermore, as precipitation rose (Figs. 4B and 5), the Si co-substituted HA finally coated the total scaffold surface (Fig. 7D), but was not as high as the precipitation that closed the scaffold macropores (Figs. 4B and 5).

The occurrence of this phenomenon is supported by previously reported results. The eutectic composition of the tricalcium phosphate-wollastonite system in contact with SBF presents a pseudomorphic transformation of C3P into HA-like [26]. Conversely, Carrodeguas et al. [38] and García-Páez et al. [39] have reported that the eutectic composition of the tricalcium phosphate-diopside system presents a preferential dissolution of the $\beta\text{-C3P}$ phase into SBF by leaving behind a porous surface rich in diopside. Moreover in a rabbit model test, Le-Geros et al. [40] and Mate Sanchez et al. [41] have respectively

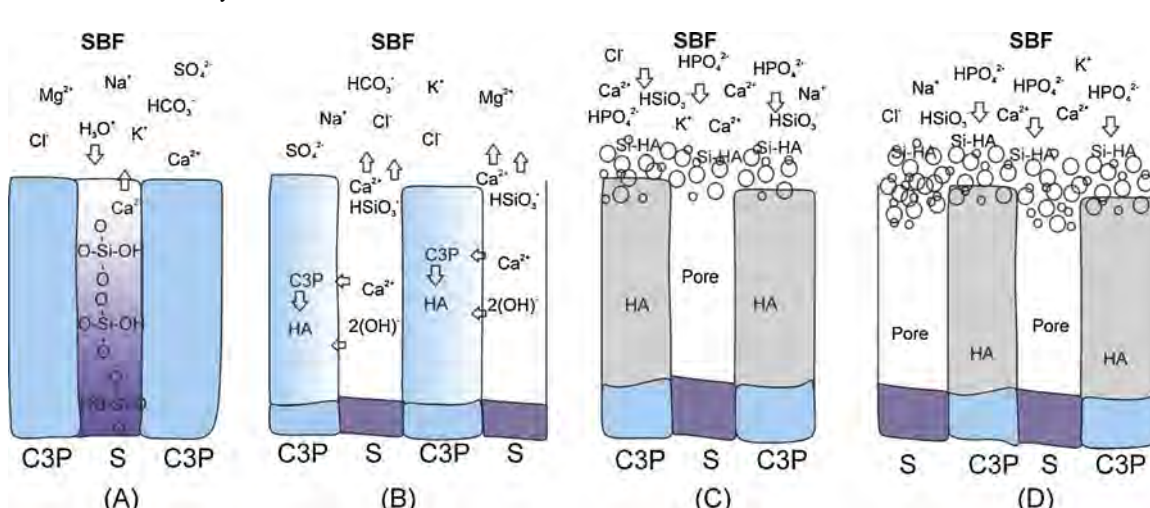


Fig. 7. Schematic mechanism of the biodegradation and bioactivity of the eutectoid scaffold. (A) dissolution of S phase, (B) pseudomorphic transformation of C3P into HA, (C) starting of precipitation of globular Si co-substituted HA, (D) massive precipitation and coating of the surface of the scaffold by Si co-substituted HA layer.

suggested the occurrence of the transformation of Mg-C3P and Si-C3P ceramics into HA, similarly to the mineral phase of bone, which took place by a similar partial dissolution and reprecipitation process to that previously reported for other calcium phosphates [41–44].

Putnis [45] made a series of important remarks on the factors that incited the event of pseudomorphic transformations in mineral systems. This author stated that in order to conserve the external microstructure of the original material, dissolution and precipitation reactions must be strongly joined at the interface that forms between the original and product phases, with a well-defined reaction front, in addition to being well-joined in time. Fluid (SBF in our case) has to conserve the contact made with the reaction front. The product phase must develop intracrystalline porosity and permeability.

The kinetics of the dissolution rate is a step that controls the process, with low activation energy for nucleation. The original phase's dissolution leads to the formation of a solution that is supersaturated compared to the product on the so-called “boundary layer”, which forms at the interface with the fluid.

Depending on the speed of the transport to and from the interface of the species in solution, the dissolution of an original phase monolayer may even oversaturate the boundary layer compared to the product phase. The nucleation of the product phase occurs on the dissolving original phase surface, which means that the new phase's external surfaces and the original crystal correspond. If the original and product phases' solubilities significantly different, even minor dissolution results in a supersaturated fluid, with which nucleation will speed up, even if no crystallographic relation exists between the two solid phases.

Further studies need to be conducted to establish the cell biocompatibility and *in vivo* behaviour of scaffolds in bone tissue engineering applications.

5. Conclusions

Scaffolds with eutectoid microstructures have been achieved from the silicocarnotite-tricalcium phosphate subsystem by the polymer replica method, followed by slow cooling inside a furnace. The scaffold's microstructure is composed of alternating irregular lamellae of silicocarnotide and α -C3P.

When the eutectoid scaffold ceramics are submerged in SBF, they first react by dissolving the silicocarnotite phase and developing a microporous apatite structure by the pseudomorphic transformation of the α -C3P phase.

The silicocarnotite dissolution phase modifies the chemistry and topography of the scaffold, and leads to the *in situ* formation of an interconnected microporous apatite structure. Later a dense Si co-substituted HA coats the entire scaffold surface, which is expected to promote bone growth. The new achieved scaffold microstructure is similar to that of porous bone.

Funding

This research did not receive any specific grant from funding agencies in the public, commercial, or not-for-profit sectors.

References

- [1] L.L. Hench, J.M. Polak, Third-generation biomedical materials, *Science* 295 (2002) 1014–1017, <https://doi.org/10.1126/science.1067404>.
- [2] J. Chevalier, L. Gremillard, Ceramics for medical applications: a picture for the next 20 years, *J. Eur. Ceram. Soc.* 29 (2009) 1245–1255.
- [3] C.J. Bettinger, R. Langer, J.T. Borenstein, Engineering substrate topography at the micro- and nanoscale to control cell function, *Angew. Chem. Int. Ed. Engl.* 48 (2009) 5406–5415.
- [4] B. Paredes, A. Santana, M.I. Arribas, N. Vicente-Salar, P.N. De Aza, E. Roche, J. Such, J.A. Reig, Phenotypic differences during the osteogenic differentiation of single cell-derived clones isolated from human lipoaspirates, *J. Tissue Eng. Regen. Med.* 5 (8) (2011) 589–599, <https://doi.org/10.1002/term.351>.
- [5] M. Okamoto, Y. Dohi, H. Ohgushi, H. Shimaoka, M. Ikeuchi, A. Matsushima, K. Yonemasu, H. Hosoi, Influence of the porosity of hydroxyapatite ceramics on *in vitro* and *in vivo* bone formation by cultured rat bone marrow stromal cells, *J. Mater. Sci. Mater. Med.* 17 (2006) 327–336.
- [6] M.C. von Doernberg, B. von Rechenberg, M. Bohner, S. Grünenfelder, G.H. van Lenthe, R. Müller, B. Gasser, R. Mathys, G. Baroud, J. Auer, In vivo behavior of calcium phosphate scaffolds with four different pore sizes, *Biomaterials* 27 (2006) 5186–5198, <https://doi.org/10.1016/j.biomaterials.2006.05.051>.
- [7] A. Hoppe, N.S. Güldal, A.R. Boccaccini, A review of the biological response to ionic dissolution products from bioactive glasses and glass-ceramics, *Biomaterials* 32 (2011) 2757–2774, <https://doi.org/10.1016/j.biomaterials.2011.01.004>.
- [8] A. Bandyopadhyay, S. Bernard, W. Xue, S. Bose, Calcium phosphate-based resorbable ceramics: influence of MgO, ZnO, and SiO₂ dopants, *J. Am. Ceram. Soc.* 89 (9) (2006) 2675–2688.
- [9] J.E. Mate-Sánchez de Val, J.L. Calvo-Guirado, R.A. Delgado-Ruiz, Ma P. Ramírez-Fernández, I.M. Martínez, J.M. Granero-Marin, B. Negri, F. Chiva-García, J.M. Martínez-González, P.N. de Aza, New block graft of α -TCP with silicon in critical size defects in rabbits: chemical characterization, histological, histomorphometric and micro-CT study, *Ceram. Int.* 38 (2012) 1563–1570, <https://doi.org/10.1016/j.ceramint.2011.09.042>.
- [10] M. Sepantafar, H. Mohammadi, R. Maheronnaghsh, L. Tayebi, H. Baharvand, Single phased silicate-containing calcium phosphate bioceramics: promising biomaterials for periodontal repair, *Ceram. Int.* 44 (2018) 11003–11012, <https://doi.org/10.1016/j.ceramint.2018.03.050>.
- [11] A. Krajewski, M. Mazzocchi, P.L. Baldini, A. Ravaglioli, A. Tinti, P. Taddei, C. Fagnano, Synthesis of carbonated hydroxyapatites: efficiency of the substitution and critical evaluation of analytical methods, *J. Mol. Struct.* 744–747 (2005) 221–228.
- [12] J. Lu, M. Descamps, J. Dejou, G. Koubi, P. Hardouin, J. Lemaitre, J.P. Proust, The biodegradation mechanism of calcium phosphate biomaterials in bone, *J. Biomed. Mater. Res.* 63 (2002) 408–412, <https://doi.org/10.1002/jbm.10259>.
- [13] R. Agarwal, A.J. Garcia, Biomaterial strategies for engineering implants for enhanced osseointegration and bone repair, *Adv. Drug Deliv. Rev.* 94 (2015) 53–62, <https://doi.org/10.1016/j.addr.2015.03.013>.
- [14] S.V. Dorozhkin, *In vitro* mineralization of silicon containing calcium phosphate bioceramics, *J. Am. Ceram. Soc.* 90 (1) (2007) 244–249.
- [15] J.E. Mate-Sánchez de Val, J.L. Calvo-Guirado, R.A. Delgado-Ruiz, Ma P. Ramírez-Fernández, B. Negri, M. Abboud, I.M. Martínez, P.N. de Aza, Physical properties, mechanical behavior, and electron microscopy study of a new α -TCP block graft with silicon in an animal model, *J. Biomed. Mater. Res. A* 100A (12) (2012) 3446–3454, <https://doi.org/10.1002/jbm.a.34259>.
- [16] H. Yu, K. Liu, F. Zhang, W. Wei, C. Chen, Q. Huang, Microstructure and *in vitro* bioactivity of silicon-substituted hydroxyapatite, *Silicon* 9 (2017) 543–553, <https://doi.org/10.1007/s12633-015-9298-3>.
- [17] J.W. Reid, L.K. Tuc, M. Sayer, K. Fargo, J.A. Hendry, Synthesis and characterization of single-phase silicon-substituted -tricalcium phosphate, *Biomaterials* 27 (2006) 2916–2925.
- [18] I.R. Gibson, S. Best, W. Bonfield, Chemical characterization of silicon-substituted hydroxyapatite, *J. Biomed. Mater. Res.* 44 (1999) 422–428.
- [19] S. Gomes, J.M. Nedelec, E. Jallot, D. Sheptyakov, G. Renaudin, Silicon location in silicate-substituted calcium phosphate ceramics determined by neutron diffraction, *Cryst. Growth Des.* 11 (2011) 4017–4026.
- [20] P.N. De Aza, Z.B. Luklinska, J.E. Mate-Sánchez de Val, J.L. Calvo-Guirado, Biodegradation process of α -tricalcium phosphate and α -tricalcium phosphate solid solution bioceramics *in vivo*: a comparative study, *Microsc. Microanal.* 19 (2013) 1350–1357, <https://doi.org/10.1017/S1431927613001864>.
- [21] P.N. De Aza, M.A. Rodríguez, S.A. Gehrke, J.E. Maté-Sánchez de Val, J.L. Calvo-Guirado, A Si- α TCP scaffold for biomedical applications: an experimental study using the rabbit tibia model, *Appl. Sci.-Basel* 7 (7) (2017) 706, <https://doi.org/10.3390/app7070706>.
- [22] M.M. Ferreira, A.F. Brito, C.F. Marques, L.F. Freitas, E. Carrihalo, A.M. Abrantes, A.S. Pires, M.J. Aguiar, L. Carvalho, M.F. Botelho, J.M.F. Ferreira, Can the regenerative potential of an alkali-free bioactive glass composition be enhanced when mixed with resorbable beta-TCP? *Ceram. Int.* 44 (5) (2018) 5025–5031, <https://doi.org/10.1016/j.ceramint.2017.12.099>.
- [23] G. Pezzotti, T. Adachi, F. Boschetto, W.L. Zhu, M. Zanocco, E. Marin, B.S. Bal, B.J. McEntire, Off-stoichiometric reactions at the cell-substrate biomolecular interface of biomaterials: *in situ* and *ex situ* monitoring of cell proliferation, differentiation, and bone tissue formation, *Int. J. Mol. Sci.* 20 (17) (2019), <https://doi.org/10.3390/ijms20174080>.
- [24] J.R. García, A.J. García, Biomaterial mediated strategies targeting vascularization for bone repair, *Drug Deliv. Transl. Res.* 6 (2) (2016) 77–95, <https://doi.org/10.1007/s13346-015-0236-0>.
- [25] S. Bose, D. Banerjee, S. Robertson, S. Vahabzadeh, Enhanced *in vivo* bone and blood vessel formation by iron oxide and silica doped 3D printed tricalcium phosphate scaffolds, *Ann. Biomed. Eng.* 46 (9) (2018) 1241–1253, <https://doi.org/10.1007/s10439-018-2040-8>.
- [26] A.H. De Aza, P. Velasquez, M.I. Alemany, P. Pena, P.N. De Aza, *In situ* bone-like apatite formation from a Bioeutectic® ceramic in SBF dynamic flow, *J. Am. Ceram. Soc.* 90 (4) (2007) 1200–1207, <https://doi.org/10.1016/j.nonrads.2005.04.062>.
- [27] I.M. Martínez, P.A. Velasquez, P.N. De Aza, The sub-system α -TCPss – silico-carnotite within the binary system Ca₃(PO₄)₂ – Ca₂SiO₄, *J. Am. Ceram. Soc.* 95 (3) (2012) 1112–1117, <https://doi.org/10.1111/j.1551-2916.2011.05031.x>.
- [28] S. Serena, A. Caballero, P.N. De Aza, M.A. Sainz, New evaluation of the *in vitro* response of silicocarnotite monophasic material, *Ceram. Int.* 41 (2015) 9412–9419, <https://doi.org/10.1016/j.ceramint.2015.03.319>.
- [29] T. Nakamura, K. Yamashita, M. Neo, Apatite formation behavior on tricalcium

- phosphate (TCP) porous body in a simulated body fluid, *Key Eng. Mater.* 309–311 (2006) 251–254, <https://doi.org/10.4028/www.scientific.net/KEM.309-311.251>.
- [30] I.M. Martinez, L. Meseguer-Olmo, A. Bernabeu-Eslapez, P.A. Velasquez, P.N. De Aza, In vitro behavior of alpha-tricalcium phosphate doped with dicalcium silicate in the system $\text{Ca}_2\text{SiO}_4\text{-Ca}_3(\text{PO}_4)_2$, *J. Miner. Mater. Charact. Eng.* 63 (2012) 47–55, <https://doi.org/10.1016/j.matchar.2011.10.013>.
- [31] S. Serena, M.A. Sainz, A. Caballero, Single-phase silicocarnotite synthesis in the subsystem $\text{Ca}_3(\text{PO}_4)_2\text{-Ca}_2\text{SiO}_4$, *Ceram. Int.* 40 (2014) 8245–8252, <https://doi.org/10.1016/j.ceramint.2014.01.022>.
- [32] I.M. Martínez, P.A. Velasquez, L. Meseguer-Olmo, P.N. De Aza, Production and study of in vitro behaviour of monolithic α -tricalcium phosphate based ceramics in the system $\text{Ca}_3(\text{PO}_4)_2\text{-Ca}_2\text{SiO}_4$, *Ceram. Int.* 37 (2011) 2527–2535, <https://doi.org/10.1016/j.ceramint.2011.03.062>.
- [33] A. Diaz-Arca, P. Mazón, P.N. De Aza, Eutectoid scaffold as potential tissue engineer guide, *J. Am. Ceram. Soc.* 102 (12) (2019) 7168–7177, <https://doi.org/10.1111/jace.16639>.
- [34] ISO/FDIS 23317, *Implants for Surgery- In Vitro Evaluation for Apatite-Forming Ability of Implant Materials*, (2007).
- [35] J. Hu, D.K. Agrawal, R. Roy, Investigation of hydration phases in the system $\text{CaO-SiO}_2\text{-P}_2\text{O}_5\text{-H}_2\text{O}$, *J. Mater. Res.* 3 (4) (1988) 772–780.
- [36] P. Vanis, I. Odler, Hydration reactions in the system $\text{CaO-P}_2\text{O}_5\text{-SiO}_2\text{-}(\text{H}_2\text{O})$, *J. Am. Ceram. Soc.* 79 (4) (1996) 1124–1126.
- [37] M.W. Barnes, M. Klimkiewicz, P.W. Brown, Hydration in the system $\text{Ca}_2\text{SiO}_4\text{-Ca}_3(\text{PO}_4)_2$, at 90°C, *J. Am. Ceram. Soc.* 75 (6) (1992) 1423–1429.
- [38] R.G. Carrodeguas, E. Córdoba, A.H. De Aza, S. De Aza, P. Pena, Bone-like apatiteforming ability of $\text{Ca}_3(\text{PO}_4)_2\text{-CaMg}(\text{SiO}_3)_2$ ceramics in simulated body fluid, *Key Eng. Mater.* 396–398 (2009) 103–106, <https://doi.org/10.4028/www.scientific.net/KEM.396-398.103>.
- [39] I.H. García-Páez, P. Pena, C. Baudín, M.A. Rodríguez, E. Córdoba, A.H. De Aza, Processing and in vitro bioactivity of $\beta\text{-Ca}_3(\text{PO}_4)_2\text{-CaMg}(\text{SiO}_3)_2$ ceramic with the eutectic composition, *Bol. Soc. Esp. Ceram. Vidrio* 55 (2016) 1–12, <https://doi.org/10.1016/j.bsecv.2015.10.004>.
- [40] R.Z. LeGeros, A.M. Gatti, R. Kijkowska, D.Q. Mijares, J.P. LeGeros, Mg-substituted tricalcium phosphates: formation and properties, *Key Eng. Mater.* 254–256 (2004) 127–130, <https://doi.org/10.4028/www.scientific.net/KEM.254-256.127>.
- [41] J. Mahamid, A. SharirC, D. Gur, E. Zelzer, L. Addadi, S. Weiner, Mapping amorphous calcium phosphate transformation into crystalline mineral from the cell to the bone in zebrafish fin rays, *Proc. Natl. Acad. Sci. U. S. A.* 107 (2010) 6316–6321, <https://doi.org/10.1073/pnas.1001401107>.
- [42] A.K. Rajasekharan, M. Andersson, Role of nanoscale confinement on calcium phosphate formation at high supersaturation, *Cryst. Growth Des.* 15 (2015) 2775–2780, <https://doi.org/10.1002/smll.201700550>.
- [43] L. Wang, G.H. Nancollas, Calcium orthophosphates: crystallization and dissolution, *Chem. Rev.* 108 (2018) 4628–4669, <https://doi.org/10.1021/cr0782574>.
- [44] A. Lotsari, A.K. Rajasekharan, M. Halvarsson, M. Andersson, Transformation of amorphous calcium phosphate to bone-like apatite, *Nat. Commun.* 9 (2018) 4170, <https://doi.org/10.1038/s41467-018-06570-x>.
- [45] A. Putnis, Mineral replacement reactions, *Rev. Mineral. Geochem.* 70 (2009) 87–124, <https://doi.org/10.2138/rmg.2009.70.3>.

9.4. Artículo 4



Article

Micro-/Nano-Structured Ceramic Scaffolds That Mimic Natural Cancellous Bone

Anabel Díaz-Arca ¹, Patricia Ros-Tárraga ¹, María J. Martínez Tomé ², Antonio H. De Aza ³, Luis Meseguer-Olmo ⁴, Patricia Mazón ¹ and Piedad N. De Aza ^{1,*}

¹ Instituto de Bioingeniería, Universidad Miguel Hernández, 03202 Elche, Spain; a.diaza@umh.es (A.D.-A.); patricia.ros01@goumh.umh.es (P.R.-T.); pmazon@umh.es (P.M.)

² Instituto de Investigación, Desarrollo e Innovación en Biotecnología Sanitaria de Elche, 03202 Elche, Spain; mj.martinez@umh.es

³ Instituto de Cerámica y Vidrio, ICV-CSIC, 28049 Madrid, Spain; aaza@icv.csic.es

⁴ Grupo de Investigación en Regeneración y Reparación de Tejidos, Universidad Católica San Antonio de Murcia, Guadalupe, 30107 Murcia, Spain; lmeseguer@ucam.edu

* Correspondence: piedad@umh.es



Citation: Díaz-Arca, A.; Ros-Tárraga, P.; Tomé, M.J.M.; De Aza, A.H.; Meseguer-Olmo, L.; Mazón, P.; De Aza, P.N. Micro-/Nano-Structured Ceramic Scaffolds That Mimic Natural Cancellous Bone. *Materials* **2021**, *14*, 1439. <https://doi.org/10.3390/ma14061439>

Academic Editor: Franz E. Weber

Received: 29 January 2021

Accepted: 12 March 2021

Published: 16 March 2021

Publisher's Note: MDPI stays neutral with regard to jurisdictional claims in published maps and institutional affiliations.



Copyright: © 2021 by the authors. Licensee MDPI, Basel, Switzerland. This article is an open access article distributed under the terms and conditions of the Creative Commons Attribution (CC BY) license (<https://creativecommons.org/licenses/by/4.0/>).

1. Introduction

Scaffold-based tissue engineering is a discipline that employs templates to stimulate and support the bone regeneration process. An ideal scaffold should have a similar micro-/nano-structure and chemical composition to that in the bone mineral phase to provide a native environment. To improve scaffold-host tissue interactions, templates can be functionalized with several cells, proteins and growth factors [1,2]. Scaffolds should also promote osseointegration by means of bioactive, osteoinductive, and osteoconductive properties. Finally, they must have surface properties to improve vascular ingrowth and to allow cell fixation and proliferation [3,4].

Porosity is one of the most important factors to control when designing scaffolds because both microporosity (<10 µm pore size) and macroporosity (>100 µm pore size) play a key role in the cellular processes that promote bone growth [5]. Other involved factors are composition and the phases present in the material constituting scaffolds. Hence ceramic materials in the Si-Ca-P family, such as Si-hydroxyapatite (Si-HA), Si-tricalcium phosphate (Si-TCP), Nurse's A phase (7CaOP₂O₅2SiO₂) and silicocarnotite (SC-5CaOP₂O₅SiO₂),

mimic the behavior of natural apatites by forming an active chemical bond on its surfaces that leads to bone tissue neoformation [6,7]. The outstanding biocompatibility of such a ceramic is thanks to the chemical similarity to the bone mineral phase, which is constituted by about 70% calcium phosphate known as hydroxyapatite [8].

A range of methods and materials has been indicated to synthesize and process these ceramics, including biological and synthetic sources and adding ions to improve their biological responses and other properties [9–12]. Here bioinspired micro-/nano-structured ceramic scaffolds sintered by a polyurethane replica technique based on calcium, phosphorus and silica are presented that can act as scaffolds for bone tissue engineering. Given the different behaviors of its constituent phases, this material develops lamellar micro-/nano-porosity when exposed to a physiological medium. To obtain micro-/nano-porosity, a distinctive composition in the TCP-SC subsystem was selected [13]. This composition was that which corresponded to the invariant eutectoid point because a lamellar structure developed during cooling [14]. In order to control the surface nanostructures and mechanical strength, the sintering process involved a new heat treatment variant, including radial heat extraction, cooling rate control via the eutectoid temperature and low cooling until room temperature.

A comparative SEM study between the bioinspired new materials and natural cancellous bone was performed to evaluate ultrastructural similarity. To estimate the scaffolds' non-cytotoxic effect, cell attachment and proliferation ability were studied in vitro. An enzyme involved in the bone formation and mineralization process (alkaline phosphatase, ALP) was grafted to scaffolds to achieve biological functionalization.

2. Materials and Methods

2.1. Ceramic Scaffolds Synthesis

SC and α -TCP powders were used as raw ceramic materials to synthesize eutectoid lamellar scaffolds following the previously reported sintering and characterization process [15]. Briefly, 53.4 wt% SC and 46.6 wt% α -TCP powder was ground to an average particle size of 12 μm (Mastersizer 2000, Malvern Instruments Ltd., Malvern, PA, USA). The barbotine suspension of grinding powder was prepared to coat the polyurethane templates (ppi 30) in the macroporous green samples prior to a sintering process run in a 50 mL platinum foil crucible at a heating rate of 85 $^{\circ}\text{C}/\text{h}$ in an Entech electric furnace, which was raised to 1550 $^{\circ}\text{C}/3\text{ h}$. In order to control the surface nanostructure and mechanical strength, from this temperature three cooling rates were studied through the eutectoid temperature (50 $^{\circ}\text{C}/\text{h}$, 16.5 $^{\circ}\text{C}/\text{h}$ and 5.5 $^{\circ}\text{C}/\text{h}$). At 1100 $^{\circ}\text{C}$, the cooling rate was changed back to 85 $^{\circ}\text{C}/\text{h}$ and cooling continued until room temperature. The manufactured scaffolds were cylinders (8 mm diameter \times 4 mm high).

2.2. Scaffolds Characterization

Scaffolds' volumetric shrinkage S_v (%) was assessed in 10 specimens for each cooling rate as:

$$S_v = (1 - V_s/V_0) \times 100\% \quad (1)$$

where V_s is the scaffold final volume and V_0 is the volume of the green body before heat treatment. Open porosity (%) (pores larger than 100 μm) was evaluated by Archimedes' method. Scaffolds' strength, in terms of maximum compressive stress before fracture, was tested by the crushing test in a Simple Manual Test Stand (NEURTEK instruments SVL-1000N). Axial force was constantly applied to scaffolds until fracture, and was recorded in a digital force gauge dst/dsv SERIES. Maximum compressive stress σ_c (MPa) was calculated as:

$$\sigma_c = F_c/A \quad (2)$$

where F_c (N) is the maximum force recorded during the test and A (mm^2) is the scaffolds' cross-sectional area perpendicular to axial force. Ten specimens for each cooling rate were tested. Results were represented by mean values \pm standard deviation.

The scaffolds' micro-/nano-structure was characterized by scanning electron microscopy in a SEM-Hitachi S-3500N device with an Energy-Dispersive X-Ray Spectroscopy (EDS-INCA, Oxford Instruments Analytical, Oxford, UK) using a JEOL JEE-400 vacuum evaporator to coat specimens with palladium. The SC-TCP lamellae interphase on scaffold surfaces was studied in more detail by a transmission electron microscopy (TEM-HRTEM-JEM-2010 Jeol Ltd., Tokyo, Japan) analysis. To determine the Raman active vibration modes of phosphate-silicate tetrahedra stretching and bending, Raman spectra were recorded at room temperature using a Witec ALPHA 300RA Confocal Raman device within the $200\text{--}1200\text{ cm}^{-1}$ frequency ranges, and with 532 nm Nd: YAG laser light source in the p-polarization mode and a $20\times$ objective lens.

2.3. SEM Examination of Natural Cancellous Bone

The cancellous bone ultrastructure analysis was performed by the SEM examination of adult pig distal femoral epiphysis in a JEOL JSM 6100 that operated at 15–20 kV. Specimens were obtained in a sagittal section from the epiphyseal plate using a 10 mm trephine (Shanghai LZQ-Technology, Shanghai, China). Bone samples, initially cut with a cylindrical morphology of 10 mm in diameter and 10.5 mm thickness, were sectioned perpendicularly to the longitudinal axis in discs that were 1.5 ± 0.3 mm thick. Specimens were cleaned to remove all types of organic matter by immersing them in H_2O_2 with continuous magnetic stirring for 12 h, and then in 10% Triton X-100 detergent solution (Merck, Darmstadt, Germany) for 24 h. Finally, they were washed with deionized water for 24 h and dried at 37°C . For the SEM examination, the extracellular matrix structures were processed as indicated below:

- Fixation for 2.5 h in a McDowell's and Trump's 4F:1G fixative solution [16] that consists in a combination of 4% commercial formaldehyde and 1% glutaraldehyde in a buffer of 176 mOsm/liter. It is recommended as a primary fixative for the SEM analysis of samples.
- Washed in cacodylate buffer at 0.1 M and saccharose at 8% overnight at 4°C .
- Fixation was completed with 1% osmium tetroxide and 0.1 M cacodylate for 1.5 h at 4°C .
- Dehydration by gradient acetone series 30%, 50%, 70%, 90%, and 100% for 10 min each at room temperature
- Critical point drying in CO_2 .
- Finally, samples were gold-coated by the Bio-Rad Polaron coater (Bio-Rad Laboratories, Hercules, CA, USA).

After removing organic bone elements, many evident images of the mineralized matrix were obtained.

2.4. Ah-MSCs: Isolation, Expansion and Characterization

Undifferentiated multipotent adult human mesenchymal stem cells (ah-MSCs) were isolated from the human bone marrow according to a previously reported protocol [17]. The previously signed informed consent of volunteers was needed for the intervention. The assay protocol was approved for the Institutional Ethics Committee of the Universidad Católica San Antonio (authorized n°CE051904). Ah-MSCs were characterized according to the minimal standard criteria established by Dominici et al. [18]. The methods followed for the culture and expansion of ah-MSCs are found in a previous work [19]. Expanded cells, passage 3 (P3), were collected for the in vitro tests.

2.5. Ah-MSCs Adhesion and Proliferation In Vitro Test

In adhesion and proliferation terms, the non-cytotoxic effect of scaffolds on ah-MSCs was studied in vitro on scaffold surfaces. The scaffold cooled at $5.5^\circ\text{C}/\text{h}$ was selected for the assay as it exhibited improved mechanical strength. Two kinds of cell culture media were used:

- (a) Basal growth medium (GM). It consists in 10% inactivated fetal bovine serum (FBS) and 1% antibiotics (penicillin (100 U/mL)/streptomycin (100 $\mu\text{g}/\text{mL}$)) supplemented in Dulbecco's Modified Eagle Medium (DMEM) (Sigma-Aldrich, St. Louis, MO, USA).

- (b) Osteogenic-inducing medium (OM). It consists in GM with an osteogenic supplement composed of L-ascorbic acid 2-phosphate (0.2 mM; mSigma, St. Louis, MO, USA), dexamethasone (10 nM; Sigma) and β -glycerolphosphate (10 mM; Merck, Darmstadt, Germany).

Sterilized scaffolds were incubated in GM for 1 h before seeding. Cells were seeded at a density of 5×10^3 cells/cm² on scaffold surfaces in 48-well plates. Incubation was performed at 37 °C, 5% CO₂, and 95% relative humidity with 800 μ L of GM for 7, 14, 21, and 28 days according to previous works [17,19]. The cells grown in plastic, in the absence of scaffolds, were used as a positive control. At 21 days, half the samples were changed from GM to OM until 28 days. After each incubation time, cell metabolic functions were assessed by the Alamar Blue assay. Samples were washed twice with phosphate buffer saline 1× (PBS 1×) and supplied with 800 μ L of GM with 10% Alamar Blue (Invitrogen, Carlsbad, CA, USA). Then, samples were incubated for 4 h in the dark at 37 °C. After 4 h, 200 μ L of reactant were placed in a new 96-well plates for the fluorescence analysis in a Synergy MX ultraviolet visible (UV–Vis) reader (BioTeK Instruments Inc., Winooski, VT, USA). The excitation–emission wavelengths were 560–590 nm, respectively. For the SEM examination, the cell-cultured scaffolds were rinsed for 10 min in PBS 1x and fixed with 3% glutaraldehyde for 1 h. Samples were preserved in cacodylate buffer (0.1 M) until fixation with 1% osmium tetroxide. They were dehydrated in a gradient series of ethanol solutions (30%, 50%, 70%, 90%, and 100% v/v) and critical point drying with liquid CO₂. Finally, samples were palladium-coated for the SEM examination.

2.6. Testing Alkaline Phosphatase Specific Activity in Cells

ALP activity is an early marker of osteogenic differentiation. The influence of scaffolds' material on the initial differentiation of ah-MSCs was estimated by ALP specific activity. The cells seeded at a density of 5×10^3 cells/cm² in 48-well plates were cultured in indirect contact with scaffolds using 800 μ L of GM for 14 and 28 days, and OM for 28 days (37 °C, 5% CO₂, and 95% relative humidity). ALP activity was assessed by the reaction with the substrate p-nitrophenyl phosphate (PNPP) (Sigma). Under optimal conditions, PNPP is hydrolyzed by the ALP to result in p-nitrophenol (PNP), characterized by a yellow color. The amount of resulting PNP is proportional to ALP activity and can be quantified by Vis-spectroscopy. Measures were taken at 405 nm by a Synergy MX ultraviolet visible (UV–Vis) reader (BioTeK Instruments Inc., Winooski, VT, USA).

2.7. Alkaline Phosphatase Grafting to Scaffolds

In order to biofunctionalize scaffolds, the ALP was grafted onto their structures. The scaffold cooled at 5.5 °C/h was selected for the assay as it exhibited improved mechanical strength. The ALP was chosen as the enzyme model because its activity plays an active role in bone formation and mineralization processes [20,21]. To prepare ALP solution (250 μ M), bovine ALP (from bovine intestinal mucosa, lyophilized powder, ≥ 10 DEA units/mg solid, Sigma–Aldrich) was dissolved in Tris (hydroxymethyl) aminomethane ((HOCH₂)₃CNH₂, 99.9+% ultrapure grade, Sigma–Aldrich) buffer (55 mM, pH 9) with ultrasonic stirring.

Three scaffolds were immersed in 1 mL of ALP solution for 24 h at 4 °C. When incubation ended, samples were rinsed in 5 mL of Tris buffer with magnetic stirring for 10 min and then dried at room temperature. Finally, they were stored hydrated in Tris buffer in a Petri dish at 4 °C. The functionalized samples' effectiveness was investigated by running an enzymatic activity test as described below.

2.8. Enzymatic Activity Test

The ALP grafted onto scaffolds should be biologically active to achieve suitable enzymatic functionalization. Enzyme activity was studied by the reaction between the grafted ALP and substrate PNPP. In order to determine grafted ALP activity after 7, 14, 21 days of functionalization, samples were placed in 5 mL of the 50 μ M PNPP (Fisher Scientific, Fair Lawn, NJ, USA) solution in Tris buffer. The reaction between the ALP

grafted onto scaffolds and PNPP was quantified by measuring absorbance at 405 nm in a UV-2700 Spectrophotometer (Shimadzu, Tokyo, Japan) every 40 min for 2 h. At the end of each test, samples were rinsed 3 times in 5 mL of Tris buffer with magnetic stirring for 10 min. Then they were stored hydrated in Tris buffer in a Petri dish at 4 °C until the next test.

2.9. Statistical Analysis

Data are represented by mean \pm standard deviation. Anova was used to analyze the variance between different groups. The *p*-value denotes statistically significant differences when $p < 0.05$.

3. Results

3.1. Scaffolds' Characterization and Cancellous Bone Examination

After each heat treatment, all the scaffolds showed a 30% volumetric shrinkage average (Table 1). The SEM examination proved that, despite shrinkage, all scaffolds continued to maintain a highly interconnected 3D microstructure with a pore size range of 150–600 μm and an open porosity of $85 \pm 2\%$ (Figure 1A,B).

Table 1. Scaffolds' structural parameters and compressive strength for different cooling rates.

Cooling Rate	50 °C/h	16.5 °C/h	5.5 °C/h
Volumetric Shrinkage (%) *	30 ± 0.5	30 ± 0.5	30 ± 0.5
Compressive strength (MPa) *	0.62 ± 0.07	1.67 ± 0.05	3.38 ± 0.06
Lamellar width range (nm)	100–250	300–560	600–940

* Data represented as mean \pm standard deviation.

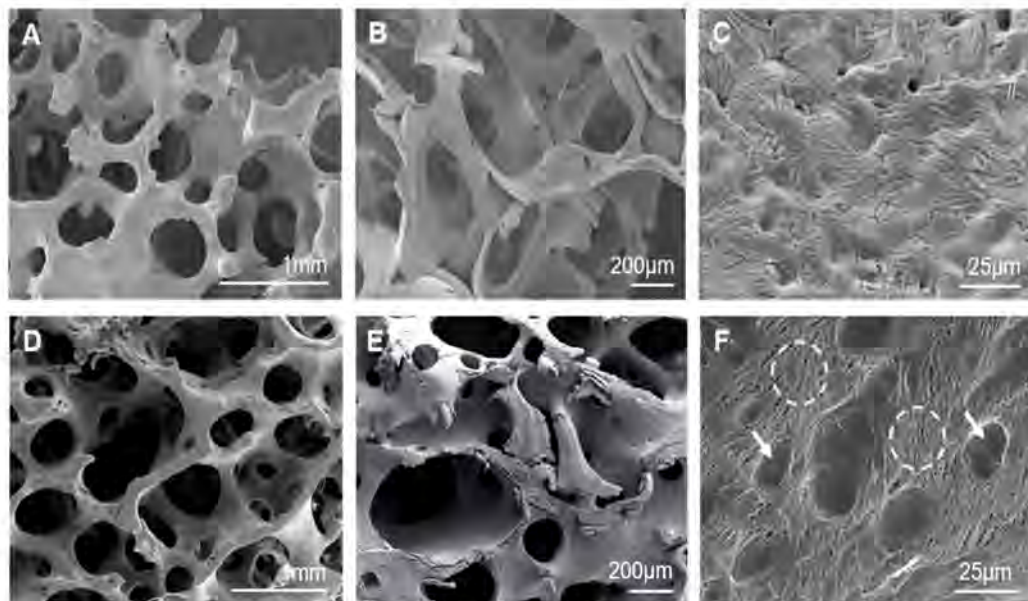


Figure 1. SEM micrographs at different magnifications showing the micro-/nano-structure of: (A–C) the eutectoid lamellar scaffold cooled at 50 °C/h as being a representative sample of them all and (D–F) natural cancellous bone.

The nanostructure of scaffold surfaces was seen in detail after being etched for 4 s with 1% dilute acetic acid (Figure 1C). Scaffold nanostructures came in the form of alternating lamellae, which suggests an irregular eutectoid structure that is homogeneously distributed over the entire surface of pore walls and struts. After chemical etching, EDS indicated the presence of calcium, phosphorous and silicon at a ratio $1.34 < \text{Ca}/(\text{P}+\text{Si}) < 1.88$. On average, this value came close to that of stoichiometric silicocarnotite ($\text{Ca}/(\text{P}+\text{Si}) = 1.66$)

which suggests that α -TCP could be the phase eliminated by chemical etching. The results from mechanically testing scaffolds are displayed at Table 1. Scaffold strength, in terms of maximum compressive stress before fracture, increased as the cooling rate lowered. The scaffold cooled at $5.5\text{ }^{\circ}\text{C/h}$ reached a mechanical strength within the range for cancellous bone (2–12 MPa) [22].

The SEM examination of the natural cancellous bone microstructure showed a highly interconnected trabeculae network with heterogeneous distributions of macropores, whose pore size range was 100–700 μm and an open porosity of $87 \pm 1\%$ (Figure 1D,E). EDS confirmed the presence of calcium and phosphorous at a ratio of $1.50 < \text{Ca/P} < 1.60$.

The nanoscale surface topography of natural cancellous bone (Figure 1F), which resulted from removing the bone organic component, showed two well-defined areas: resorbing and resting surfaces. Resorbing surfaces (the arrows in Figure 1F) were identified as resorption bays, known as Howship's lacunae, produced by osteoclast erosion. Resting surfaces (the circles in Figure 1F) were identified as lamellae that alternated in a random orientation. This morphology corresponds to the pattern of the collagen fiber bundles previously removed by sample cleaning processes. This observation agrees with the SEM data for cancellous bone reported by other authors [23–25]. Both the micro-/nano-structure of the sintered scaffolds came close to that of examined natural cancellous bone.

3.2. Characterization of the Nanostructure of Scaffold Surfaces

Figure 2 shows representative TEM images of scaffold surfaces (scaffold cooled at $50\text{ }^{\circ}\text{C/h}$ as being representative of all the scaffolds). Figure 2A illustrates an irregular alternating lamellae nanostructure, which confirmed the presence of two phases in scaffolds. The EDS analysis displayed a silicon-rich phase (● Figure 2) that corresponded to the SC phase and a calcium-phosphate phase (○ Figure 2) that corresponded to the α -TCP phase. Both phases look compact and dense with neither porosities nor cracks.

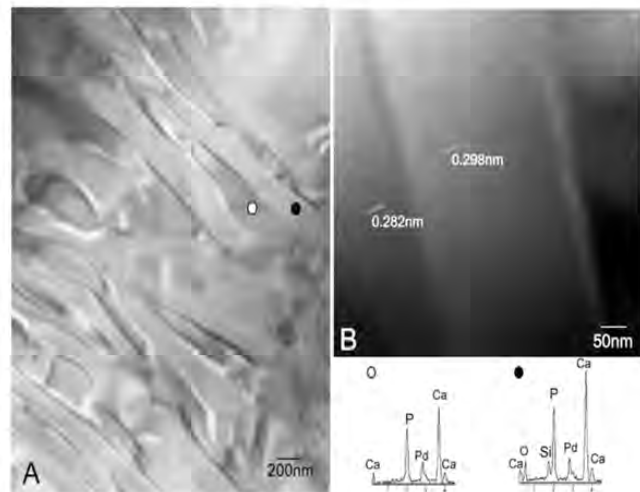


Figure 2. (A) Representative TEM image of the eutectoid scaffold surfaces and (B) the HRTEM image of the α -TCP-SC lamellae interphase and the EDS analysis. The scaffold cooled at $50\text{ }^{\circ}\text{C/h}$ was representative of all the scaffolds.

The HRTEM examination of the interfaces between SC and α -TCP (Figure 2B) indicated a smooth continuous morphology between both phases. There was no intermediate region among the lamellae up to the lattice plane resolution level. No resolved lattice plane was interrupted up to the interface, and they were all free of defects. The lattice fringes associated with $d = 0.298\text{ nm}$ corresponded to a preferred (034) orientation, as determined in Figure 2B, which confirmed that the lighter phase was α -TCP and the darker phase was SC with $d = 0.282\text{ nm}$ corresponding to a preferred (230) orientation.

A more detailed SEM analysis of scaffold surfaces, after being etched for 4 s with 1% dilute acetic acid (Figure 3), showed that lamellae thickened as the cooling rate lowered to give a lamellar width range of 100–250 nm, 300–560 nm and 600–940 nm for the cooling rate of 50 °C/h, 16.5 °C/h, and 5.5 °C/h, respectively (Table 1). Therefore, it is possible to control the eutectoid nanostructure on scaffold surfaces with the cooling rate of the sintering process.

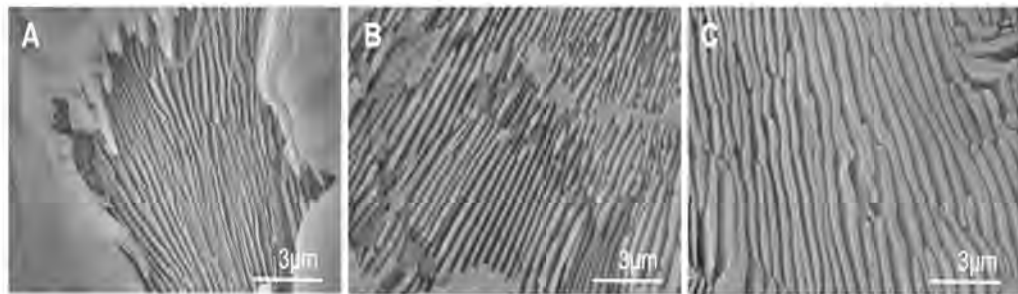


Figure 3. SEM micrographs of scaffold surfaces after chemical etching with acetic acid for a cooling rate of: (A) 50 °C/h (B) 16.5 °C/h and (C) 5.5 °C/h.

Figure 4 displays the confocal optical micrographs of the scaffold cooled at 50 °C/h as being a representative sample of all the scaffolds. A similar lamellar nanostructure to that observed in the SEM images in Figures 1C and 3 is seen. Raman scanning was performed in the marked selected square in Figure 4A, which allowed a colored Raman image to be obtained with phase distribution (Figure 4B). Two eutectoid composition phases can be discriminated: SC and α -TCP. The average Raman spectrum of phases SC and α -TCP are shown in Figure 4D. For comparison purposes, Raman spectra were also obtained for two single phase SC and α -TCP dense ceramics manufactured in our laboratory (Figure 4E) [7,26].

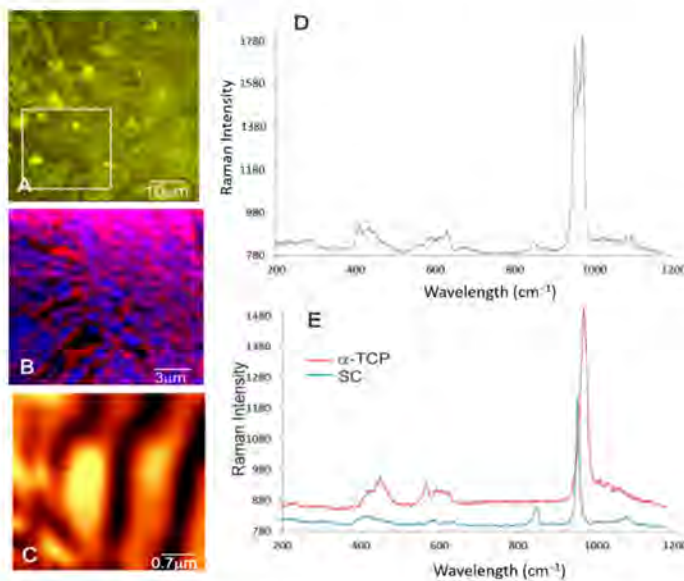


Figure 4. (A) Confocal optical micrograph of the scaffold cooled at 50 °C/h as being a representative sample. (B) Raman image of the area selected in (A) in which phases SC and α -TCP are represented in colors and display an irregular eutectoid pattern. (C) A Rayleigh light-scattering microscopy image showing a nanostructured sinusoidal disordered pattern. (D) The average Raman spectra from the scaffold. (E) Single-phase dense ceramics of SC and α -TCP for comparison purposes.

The Raman spectrum of SC displayed the following bands (cm^{-1}): 302 and 234 $\nu(\text{Ca-O})$; 420 $\nu_2(\text{SiO}_4)$; 470 $\nu_2(\text{PO}_4)$; 580 [$\nu_2(\text{PO}_4)$ + (SiO_4)]; 640 $\nu_4(\text{PO}_4)$; 850 $\nu_1(\text{SiO}_4)$;

956 $\nu_1(\text{PO}_4)$; 1000 $\nu_1(\text{SiO}_4)$; 1080 [$\nu_3(\text{PO}_4) + \nu_3(\text{SiO}_4)$] [7,27]. The strongest bands were assigned to the vibrations of (SiO_4) and (PO_4) tetrahedra.

The Raman spectrum of α -TCP displayed the following bands (cm^{-1}): 439, 460, 475, 483 $\nu_2(\text{PO}_4)$; 565, 578, 588, 599, 611, 624 $\nu_4(\text{PO}_4)$; 960, 970 $\nu_1(\text{PO}_4)$; 1005, 1016, 1031, 1046, 1060, 1075, 1085, 1090 $\nu_3(\text{PO}_4)$ [28,29]. The Raman spectrum of the scaffold was separated into six groups of bands as follows (cm^{-1}): 256–300; 425–467; 551–640; ~844; 950–970; 1000–1096.

Overlapping took place with the (PO_4) and (SiO_4) groups from SC and α -TCP. Isolated peak was distinguished at 845 that belonged to $\nu_1(\text{SiO}_4)$ from SC and a triple peak at 956–976–970, which allowed to distinguish $\nu_1(\text{PO}_4)$ from SC, and $\nu_1(\text{PO}_4)$ from α -TCP.

A mixture of SC and α -TCP phases was identified in the average Raman spectrum of the analyzed scaffold regions. In an attempt to distinguish both phases, Rayleigh light-scattering was carried out to verify the different phase compositions of the lamellae in the scaffold. Figure 4C depicts a Rayleigh image that was taken from a lamellar micrograin. It reveals a striped pattern with bright and dark areas, where yellow denotes the SC phase and dark areas depict the α -TCP phase.

3.3. Cell adhesion and Proliferation In Vitro Test

The scaffold cooled at 5.5 °C/h was evaluated in terms of the adhesion and proliferation ability of the ah-MSCs seeded on their surfaces. This scaffold was selected for the assay as it exhibited improved mechanical strength. The SEM micrographs of ah-MSCs' evolution on scaffold surfaces are shown in Figure 5 for different incubation times in GM. After seven days (Figure 5A,B), the agglomeration of a spherical Ca-P precipitate formed a dune-like layer that covered scaffold surfaces. Individual cells were observed to adhere to scaffold surfaces by means of extensive cytoplasmic projections (the arrows in Figure 5A,B). For 14 days after seeding (Figure 5C–G), flattened and completely adhered cells (the arrow in Figure 5C) formed isolated groups and came into close physical contact with one another and the scaffold surfaces through numerous cytoplasmic projections. At this time, some cell-free areas were still visible on scaffold surfaces where the typical lamellar nanostructure was distinguished (the circle in Figure 5C).

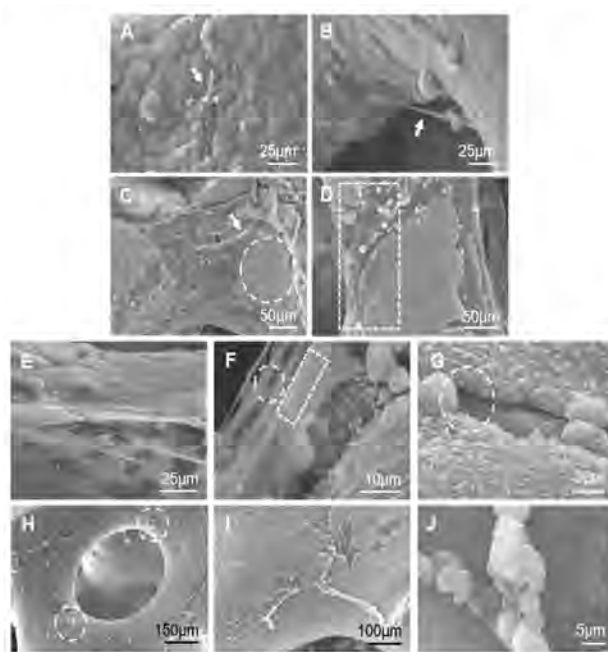


Figure 5. SEM micrographs at different magnifications of scaffold surfaces seeded with ah-MSCs in GM for: (A,B) 7, (C–G) 14 and (H–J) 28 days.

Moreover, some cells formed a monolayer adhered on the dune-like precipitate and, at the same time, a new dune-like precipitate was formed above the cell monolayer in

close contact with their membranes (Figure 5D). The rectangle in Figure 5D shows some cells spreading onto the new precipitate, which suggests the formation of a layer-by-layer structure. Figure 5E shows a cross-sectional view where the dune-like precipitates were observed in the background and at the top of the cell monolayer.

Figure 5F shows some processes in detail that took place on the periphery of cell membranes. A basal process, with many exocytosis vesicles (the rectangle in Figure 5F), was observed and their content was assembled to form the collagen-like fibrils observed around cell membranes (the circle in Figure 5F). This collagen-like meshwork initially took a random spatial orientation and was integrated with the dune-like precipitate (the circle in Figure 5G). For 21 days, the SEM observation showed a similar behavior on scaffold surfaces (data not shown). By prolonging the incubation time to 28 days, the layer-by-layer cell and dune-like deposition precipitate formed a dense and almost complete layer over the entire scaffold surfaces (Figure 5H,I). SEM revealed that this monolayer looked granular with some superficial protrusions (the circles in Figure 5H).

The presence of a fibrillary meshwork together with Ca-P mineral deposits suggests the initial formation of mineralization nodules at these superficial protrusions (see the detail in Figure 5J).

Figure 6 provides details of a broken scaffold strut, after 28 days in GM with ah-MSCs. The ultrastructural analysis revealed two different zones on the strut boundary. The layer-by-layer cell and dune-like precipitate deposition was identified (the rectangle in Figure 6A). The detail in Figure 6B shows a globular niche produced after collagen-like fibril formation that corresponds to the previously reported SEM observations for the cell-mediated extracellular matrix formation during the biomineratization process [30,31]. Moreover, a cell-free zone was also detected (the circle in Figure 6A). The magnification in Figure 6C showed three well-defined consecutive structures:

- (1) A dense dune-like layer on the GM-scaffold boundary with an average Ca/P ratio of 1.55. EDS indicated less silicon than the original sample (3). This layer was about $9 \pm 0.05 \mu\text{m}$ thick. The crystalline nature of this dune-like layer and the Ca/P ratio corresponded to the precipitated calcium-deficient nonstoichiometric hydroxyapatite.
- (2) A lamellar microstructure lay beneath the precipitated hydroxyapatite layer with an average Ca/P ratio of 1.98. EDS confirmed that the silicon was not present in the lamellar microstructure.
- (3) The original scaffold material remained inside the structure with an average Ca/P ratio of 1.64. EDS indicated higher silicon content than the precipitated hydroxyapatite layer.

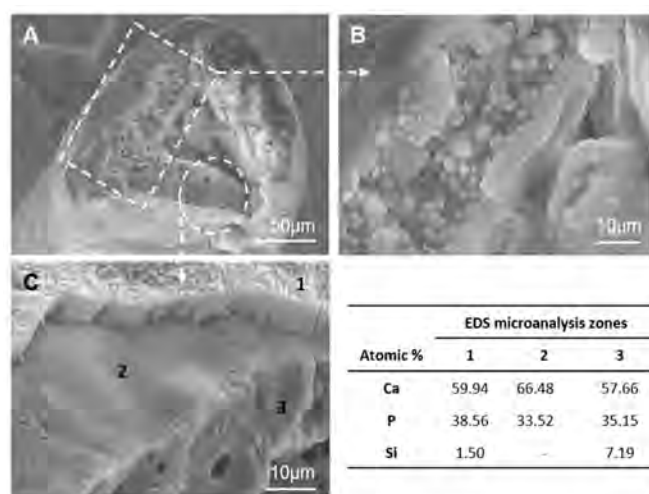


Figure 6. SEM micrographs at different magnifications of a broken scaffold strut after 28 days in GM with ah-MSCs: (A) the broken strut, (B) detail of a globular niche produced after collagen-like fibril formation and (C) detail of three well-defined consecutive structures.

The TEM-HRTEM analysis was performed to study the changes in the hydroxyapatite layer in more detail after incubation times. After seven days in culture, elongated crystals were observed whose lengths ranged between 15 and 150 nm (Figure 7A). These growing crystals were seen to grow from dark regions (* in Figure 7A). The formation of amorphous calcium phosphate clusters, associated with dark areas, has been reported by Liao et al. [32] and Dey et al. [33], who described the geometry of crystals as a “parallel array of needles” and their size with CO_3^{2-} content. Figure 7B shows several overlapped crystals in which a single one was approximately 12 nm wide and 20 nm long. Finally, an HRTEM image (Figure 7C) shows a higher density of crystals joined with lattice fringes between them ($0.238 < d < 0.263 \text{ nm}$).

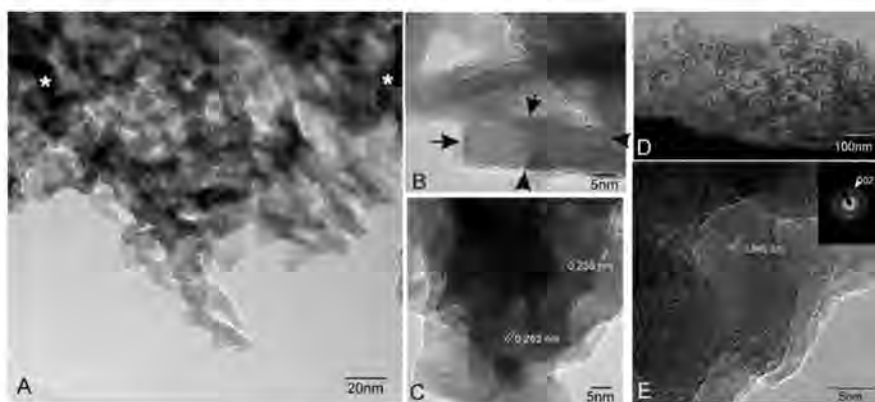


Figure 7. TEM images of the scaffold surfaces’ product: (A) after 7 days in culture (* dark regions from where the crystals grew), (B) zoom into the rectangular crystals, (C) the HRTEM image of the region, (D) after 28 days in culture showing the morphology of the new precipitate Ca-P phase and (E) the HRTEM of the region with a SAD pattern.

After 28 days, a significant density of needle arrays was seen (Figure 7D), where the Ca/P ratio of ~ 1.55 evidenced the formation of calcium-deficient apatite, which is usually found in bioactive materials [6,10,34]. In this phase, these needle-like crystals had completely merged to form a homogeneous layer with practically no space left between nanocrystals. It is noteworthy that the morphology and composition of crystals observed by TEM coincided with the growth of the needle-like crystals that formed the globular precipitated observed by SEM after seven days in culture (Figure 5A). The compositional gradient found in the EDX analysis of the cross-sectional view confirmed the TEM results. It revealed calcium-deficient apatite with Si contents. The HRTEM performed of the mature crystallized apatite layer is found in Figure 7E, where a higher density of joined crystals was observed with lattice fringes of $d = 0.340 \text{ nm}$.

There was no evidence for either cytotoxicity or cell morphological alterations throughout the observational SEM analysis. The number of cells on scaffold surfaces increased with culture time. The hydroxyapatite layer did not obstruct cell adhesion and proliferation.

Cell proliferation was quantified by the Alamar Blue assay whose results confirmed the SEM observation. Figure 8 shows metabolic activity of the ah-MSCs seeded on scaffold surfaces (S) and on the 2D tissue culture polystyrene plates as the positive control (Control) after different culture times in GM and OM.

Cell metabolic activity on scaffold surfaces progressed linearly with time until the end of the assay and its value overtook that of the control after 28 days. At this time, the low absorbance value of the control was associated with cell confluence. On polystyrene plates, cells grew in a 2D environment and proliferation was restricted by the available surface area, cell-cell interactions and nutrient availability on the cell-GM/OM boundary. Scaffolds’ 3D structure and porosity provided a bigger surface area for cell proliferation and a more efficient oxygen and nutrients exchange. The cells seeded on scaffold surfaces

showed significant differences in metabolic activity at 28 days compared to the positive control ($p < 0.05$).

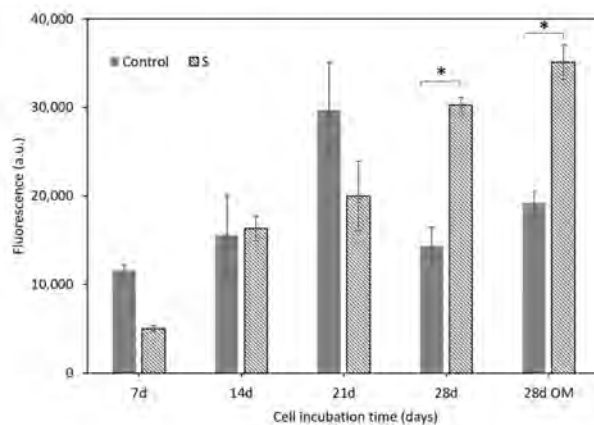


Figure 8. Metabolic activity of the ah-MSCs seeded on scaffold surfaces (S) and the positive control (Control) after different culture times in GM and OM. * denotes significant differences ($p < 0.05$) between them at the same culture time.

3.4. Specific Alkaline Phosphatase Activity in Cells

Cell differentiation was estimated in terms of the ALP activity of the ah-MSCs cultured in scaffolds (S) and the positive control (Control), after 14 and 28 days in GM and after 28 days in OM (Figure 9).

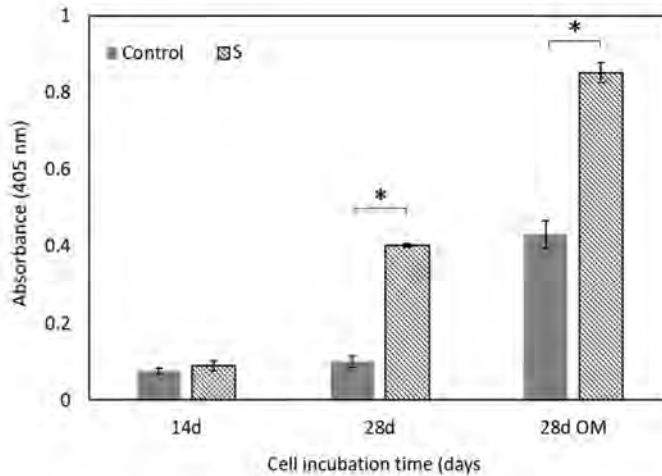


Figure 9. The quantification of ALP activity of the ah-MSCs seeded on scaffold surfaces (S) and the positive control (Control) after different culture times in GM and OM. * denotes significant differences ($p < 0.05$) between them at the same culture time.

After 14 days in GM, ALP activity was expressed at low levels and no significant differences were detected between scaffolds and the positive control. After 28 days in GM and OM, the ALP activity in the ah-MSCs incubated with the scaffold surfaces was significantly higher than in the control.

3.5. Alkaline Phosphatase Grafting to Scaffolds

The specific ALP activity on scaffolds at 7, 14, and 21 days after functionalization is shown in Figure 10. Enzyme activity was quantified by measuring absorbance at 405 nm after 40, 80 and 120 min of the reaction between the grafted ALP (250 μ M) and PNPP (50 μ M) solution. After 7 days of functionalization, the ALP grafted onto scaffolds transformed

all the PNPP at 80 min. Therefore, no difference was detected between the 80 min and 120 min measurements. This indicated that ALP was successfully grafted onto scaffolds and its active state remained. Although enzymatic activity increased with the reaction time between ALP and PNPP for the same test, it should be noted that ALP activity decreased from one test to the next. As samples were washed 3 times in Tris buffer with magnetic stirring for 10 min after each test, the grafting stability between ALP and scaffolds could be involved in this result. In this case, a fraction of grafted ALP could be released to the washing solution.

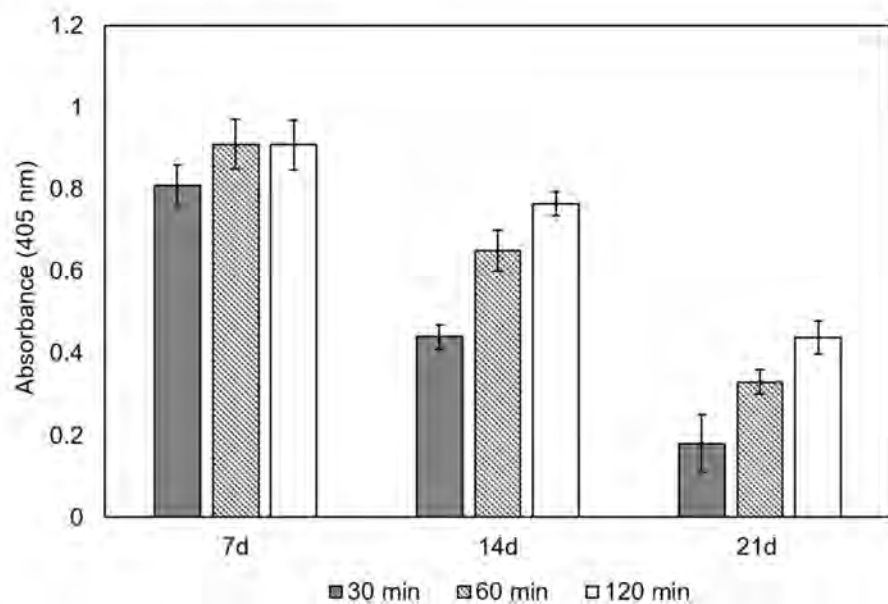


Figure 10. Specific ALP activity in scaffolds at 7, 14 and 21 days after functionalization. The enzyme activity kinetics was quantified after 40, 80 and 120 min of the reaction between the grafted ALP and PNPP solution.

4. Discussion

Nowadays, biomimetics is an essential issue for designing scaffolds whose aim is bone tissue regeneration. To provide a natural environment, an ideal scaffold must not only mimic the structure and chemical composition of natural bone, but should also consider cell biology and biomolecules as much as possible. In this context, eutectoid lamellar scaffolds were developed in the present work to mimic the micro-/nano-structure of natural cancellous bone, as well as the biomineralization process that would take place through the nucleation and growth of hydroxyapatite crystals on scaffold surfaces. Cells and protein functionalization were also supported *in vitro*.

Lamellar scaffolds were manufactured using a polyurethane template coated with a barbotine from the eutectoid ceramic composition corresponding to the TCP-SC subsystem, followed by solid-state reaction sintering [13]. Combining these methods is nothing new to other researchers, who have obtained porous scaffolds with future tissue engineering applications [2,5,8]. In the present work however, a new variant was included in the manufacturing process of scaffolds: using a unique singular composition of the system, such as a eutectoid composition, with slow cooling and radial heat extraction from the ceramic sample, to obtain a scaffold with a structure of alternating SC and α -TCP lamellae. The microstructural analysis of scaffolds showed a highly interconnected struts network enclosing large macropores similar to that observed for natural cancellous bone (Figure 1). Heterogeneous distributions of macropores were observed whose average size exceeded of 150 μm , which is reported as the minimum pore size needed to allow cell infiltration [35,36]. The larger pore size ($>300 \mu\text{m}$) improves vascularization, nutrient diffusion, and new tissue

ingrowth [37]. Open porosity was about 85% within the range reported for cancellous bone (50–90%) [38] and came close to the value observed for an adult pig bone specimen (~87%).

The nanostructure of scaffold surfaces mimicked the rough surface of natural cancellous bone. The lamellar topography provided additional porosity to scaffolds and was able to improve cell adhesion and proteins adsorption. Furthermore, inter-lamellar gaps can act as a possible site for collagen fibers organization and subsequent bone matrix mineralization. Lamellae thickened as the cooling rate lowered, with a lamellar width range between 100–250 nm, 300–560 nm, and 600–940 nm for a cooling rate of 50 °C/h, 16.5 °C/h, and 5.5 °C/h respectively (Table 1). This was related to the way in which lamellae nucleated and grew according to the cooling rate [39]. Under our study conditions, at a slow cooling rate, the results of the nucleation of a few lamellae, led to lamellae becoming considerably coarser. Therefore, nanostructures can be controlled during the synthesis process by adjusting the cooling rate.

A detailed analysis of the eutectoid lamellar nanostructure by SEM, Raman, and TEM examinations showed a well-defined mixture of alternating SC and α -TCP lamellae over the entire scaffold surfaces. The interface among lamellae was free of defects, with no intermediate regions between them.

It was also possible to control the compressive strength by the cooling rate. The compressive strength increased as the cooling rate lowered (Table 1). It is well known that the micro-/nano-structure evolution of bioceramics during the sintering process has a critical effect on their mechanical behavior [40]. For lower cooling rates, there is more time to consolidate the nanostructure that results in lamellae thickening. Furthermore, the microcracks on scaffold surfaces, which are formed by thermal shrinkage during the cooling process, can be reduced by lowering the cooling rate [41]. Accordingly, it is possible to control the micro-/nano-structure and compressive strength of the scaffolds synthesized by this method so that they resemble natural cancellous bone and are adjustable to the requirements of each bone defect.

The in vitro cell test showed that ah-MSCs adhered, spread, and proliferated over scaffold surfaces. High cell colonization was achieved by forming an extensive monolayer on the entire structure, even inside pores. The flattened cell morphology and the large number of exocytosis vesicles were indicators of a good biological response and sound metabolic activity. The Alamar Blue assay (Figure 8) proved that the scaffold's material stimulated ah-MSCs' metabolic function. From 28 days in GM and OM the proliferation rate of the ah-MSCs seeded on scaffold surfaces overtook that of the control. This effect was strong under osteogenic conditions as OM was supplemented with β -glycerophosphate, which is a source of inorganic phosphate that is known to be an important signaling molecule for cell proliferation [42]. Hence, it can be affirmed that the material did not induce cytotoxicity and stimulated cell proliferation.

ALP activity in the ah-MSCs incubated with the scaffold for 28 days was significantly greater than in the control. As ALP is an early marker of osteogenic differentiation, the scaffold's material could have stimulated the ah-MSCs to differentiate into the osteoblast phenotype. The formation of collagen-like fibrils and some mineral deposits suggest the formation of an extracellular matrix and mineralized nodules. In bone, collagen is present as fine fibers with no preferred orientation, and usually as short segments [43,44] like the collagen-like fibrils in Figure 5F,G. It is at the collagen fibers site where the first HA-crystals grow during the bone biominerilization process [38,45]. As osteoblasts are cells committed to produce collagen fibers on bone growth surfaces, ah-MSCs may have differentiated to the osteoblast phenotype on scaffold surfaces to produce collagen-like fibers. However, more detailed studies of cell differentiation in the presence of scaffolds are needed to corroborate these observations.

When scaffolds were immersed in GM solution, their surface remarkably changed and presented distinct morphologies depending on the immersion time. Different processes took place in the scaffold-GM interphase. At the beginning, individual cells adhered directly to scaffold surfaces. Those areas not covered by cells reacted with the surrounding

GM, which led to one of the phases in the alternating lamellae nanostructure to dissolve. According to SEM-EDS, lack of silicon on the scaffold surfaces meant that the dissolved phase was SC. SC phase degradation controlled the creation of a nanoporous reaction zone on scaffold surfaces. The reaction continued internally through the narrow channels within the α -TCP lamellae as SC dissolved (Figure 6). Next, spherical-shaped hydroxyapatite-like precipitation took place on scaffold surfaces. Hydroxyapatite-like precipitation was less copious at the beginning of the reaction, but turned into a heavy dense layer toward the end and covered the entire scaffold surfaces to form a layer-by-layer structure that was closely related to cell membranes (Figure 5I). This layer-by-layer structure could improve the stable chemical bonding between scaffolds and receptor bone tissue.

Si ions, which dissolved from the SC lamellae, were trapped by the new precipitate layer to produce silicon co-substituted hydroxyapatite on the periphery of scaffolds. The EDS data suggested a small quantity of Si substitution in the hydroxyapatite phase according to 59.94–38.56–1.50/Ca–P–Si atm% (Figure 6). The Si substitutions in precipitated hydroxyapatite can stimulate bone cells at the genetic level to promote cell proliferation and differentiation [46,47]. A similar reaction mechanism in simulated body fluid (SBF) has been described for this material in a previous work [48]. The eutectoid scaffold material reacts by dissolving the SC phase and then developing a hydroxyapatite microporous structure by the pseudomorphic transformation of α -TCP lamellae. Next silicon co-substituted hydroxyapatite formed a layer on scaffold surfaces.

The HRTEM and SAD patterns confirmed the hydroxyapatite phase on scaffold surfaces. The apatite crystallization process commenced with distances shorter than 0.300 nm and ended roughly at 0.340 nm, from which crystals grew in line with a preferred (002) orientation (Figure 7E, inner). This preferential orientation is related to hydroxyapatite rearrangement, whose orientation changed and favored preferential growth in new crystals. With time, single crystals started to join and form a dense layer. This crystal coalescence effect has been reported in various calcified tissue formations, referred to as “crystal fusion”, in which a single crystal tends to form from two apatite crystals joining and adhering [33,49].

The inorganic bone component is a calcium-deficient nonstoichiometric hydroxyapatite. It is well-known that the range of Ca/P values depends on many factors like the specimen donor’s gender, age and nutrition, as well as the extraction site. However, the Ca/P ratio for cancellous bone is generally considered to lie between $1.37 < \text{Ca}/\text{P} < 1.87$ [45]. The biominerization process uses mainly Ca and Si combined with carbonates and phosphates to form biological apatite. The above-described process, which takes place through the nucleation and growth of hydroxyapatite crystals on scaffold surfaces in GM, resembles the natural mechanism of bone mineralization. A similar process to bone mineralization could have taken place in vitro on scaffold structures in the presence of ah-MSCs.

In vitro SBF assays are widely used for in vivo bioactivity prediction purposes. However, some authors [50] have reported that SBF is supersaturated in relation to the hydroxyapatite crystal and forces its precipitation. Consequently, the validity of the SBF assay is questioned because a biomaterial never comes into in situ contact with inorganic fluid. Bioactive behavior not only depends on the material’s composition, but also depends on the solution used for in vitro tests. Some authors have tested the in vitro bioactivity of glass and glass ceramics in DMEM medium (containing similar ionic concentrations as blood plasma, as well as growth factors and proteins present in blood) [51,52]. Although the use of DMEM resulted in the delayed start of precipitation, the precipitated apatite layer was similar to that formed in SBF. This work reports precipitate hydroxyapatite formation in a similar organic environment similar to that of the bone mineral phase. The precipitate did not obstruct cell adhesion and proliferation.

Scaffold functionalization with different molecules and growth factors improves the interaction between the implant and surrounding tissue. In this study, ALP was chosen as the protein model for functionalization because its activity plays an active role in the mineralization process by providing local enrichment of Ca^{2+} and PO_4^{3-} ions [20,21].

Furthermore, previous studies have supported the correct functionalization of bioactive glasses and glass ceramic with an ALP model [53,54].

The ALP was successfully grafted onto scaffolds, whose enzymatic activity remained until 21 days after functionalization. It should be noted that the ALP amount decreased for 14 and 21 days compared to seven days (Figure 10). There are different types of interaction between proteins and material surfaces: simple adsorption, covalent bonding and electrostatic interaction. Regardless of anchorage type, in this case it can be affected by the washing processes between one test and the next. This may indicate that the ALP could be released to the washing solution. Therefore, more detailed studies are needed to understand the functionalization procedure's physico-chemical behavior. In any case, the enzyme was grafted onto scaffold structures and its active state remained with no prior surface functionalization treatment, which is already a good result. The presence of the ALP enzyme would support both the biomineralization process and cell activity.

5. Conclusions

The micro/nano-structure obtained in the synthesized scaffolds with the 46.6% α -TCP—53.4% SC composition mimics the micro-/nano-structure of natural cancellous bone. The nanostructure consisted of irregular eutectoid lamellae of alternating SC and α -TCP, which were affected by the cooling rate used via the eutectoid temperature. Therefore, it is possible to control the micro-/nano-structure of scaffolds and compressive strength by this sintering process, which would make them similar to natural cancellous bone and they could adjust to the requirements of each bone defect. In supplemented DMEM medium, the SC phase dissolved by modifying scaffolds' topography, which led to the in-situ formation of the nanoporous structure on surfaces. Later, a dense silicon co-substituted hydroxyapatite precipitated to form a closely related layer-by-layer structure to cell membranes to cover the entire scaffold surfaces. Scaffolds supported the adhesion and proliferation of ah-MSCs, and high colonization was achieved over entire surfaces 28 days after cell seeding. No evidence for cytotoxicity was found, although good metabolic activity was evidenced. ALP anchoring was effectively achieved, and its activity remained after 21 days since grafting. A fraction of the grafted ALP remained attached to scaffolds even after the washing process. The overall results indicate that scaffolds mimicked the structure and chemical composition of natural bone when considering cell biology and biomolecule functionalization. Therefore, the developed scaffold is an interesting material as a bone constructor for tissue engineering.

Author Contributions: Conceptualization, P.M. and P.N.D.A.; methodology, A.D.-A., P.R.-T. and M.J.M.T.; investigation, A.D.-A., P.R.-T., M.J.M.T., L.M.-O., A.H.D.A., P.M. and P.N.D.A.; writing—original draft preparation, A.D.-A., P.M. and P.N.D.A.; supervision, A.H.D.A., P.R.-T., P.M. and P.N.D.A. All authors have read and agreed to the published version of the manuscript.

Funding: Universidad Miguel Hernandez, Proyecto PAR, Resolución 02432/2020.

Institutional Review Board Statement: The study was conducted according to the guidelines of the Declaration of Helsinki, and approved by the Institutional Review Board of Universidad Católica San Antonio (Murcia) (protocol code CE051904 and date of approval 13-05-2019).

Informed Consent Statement: Informed consent was obtained from all subjects involved in the study.

Data Availability Statement: Data sharing is not applicable for this paper.

Conflicts of Interest: The authors declare no conflict of interest.

References

1. Roseti, L.; Parisi, V.; Petretta, M.; Cavallo, C.; Desando, G.; Bartolotti, I.; Grigolo, B. Scaffolds for bone tissue engineering: State of the art and new perspectives. *Mater. Sci. Eng. C* **2017**, *78*, 1246–1262. [[CrossRef](#)]
2. Jones, J.R. New trends in bioactive scaffolds: The importance of nanostructure. *J. Eur. Ceram. Soc.* **2009**, *29*, 1275–1281. [[CrossRef](#)]
3. García, J.R.; García, A.J. Biomaterial-mediated strategies targeting vascularization for bone repair. *Drug Deliv. Transl. Res.* **2016**, *6*, 77–95. [[CrossRef](#)] [[PubMed](#)]

4. Paredes, B.; Santana, A.; Arribas, M.I.; Vicente-Salar, N.; de Aza, P.N.; Roche, E.; Such, J.; Reig, J.A. Phenotypic differences during the osteogenic differentiation of single cell-derived clones isolated from human lipoaspirates. *J. Tissue Eng. Regen. Med.* **2011**, *5*, 589–599. [[CrossRef](#)] [[PubMed](#)]
5. Agarwal, R.; García, A.J. Biomaterial strategies for engineering implants for enhanced osseointegration and bone repair. *Adv. Drug Deliv. Rev.* **2015**, *94*, 53–62. [[CrossRef](#)]
6. Yu, H.; Liu, K.; Zhang, F.; Wei, W.; Chen, C.; Huang, Q. Microstructure and in vitro bioactivity of silicon-substituted hydroxyapatite. *Silicon* **2017**, *9*, 543–553. [[CrossRef](#)]
7. Serena, S.; Caballero, A.; de Aza, P.N.; Sainz, M.A. New evaluation of the in vitro response of silicocarnotite monophasic material. *Ceram. Int.* **2015**, *41*, 9412–9419. [[CrossRef](#)]
8. Eliaz, N.; Metoki, N. Calcium Phosphate Bioceramics: A Review of Their History, Structure, Properties, Coating Technologies and Biomedical Applications. *Materials* **2017**, *10*, 334. [[CrossRef](#)]
9. Kokubo, T.; Ito, S.; Huang, Z.T.; Hayashi, T.; Sakka, S.; Kitsugi, T.; Yamamuro, T. Ca, P-rich layer formed on high-strength bioactive glass-ceramic A-W. *J. Biomed. Mater. Res.* **1990**, *24*, 331–343. [[CrossRef](#)]
10. Lotsari, A.; Rajsekharan, A.K.; Halvarsson, M.; Andersson, M. Transformation of amorphous calcium phosphate to bone-like apatite. *Nat. Commun.* **2018**, *9*, 4170. [[CrossRef](#)]
11. Mate-Sánchez de Val, J.E.; Calvo-Guirado, J.L.; Delgado-Ruiz, R.A.; Ramirez-Fernandez, M.P.; Negri, B.; Abboud, M.; Martinez, I.M.; de Aza, P.N. Physical Properties, Mechanical Behavior, and Electron Microscopy Study of a New α -TCP Block Graft with Silicon in an Animal Model. *J. Biomed. Mater. Res. A* **2012**, *12*, 3446–3454. [[CrossRef](#)] [[PubMed](#)]
12. Wu, C.; Chang, J. A Review of Bioactive Silicate Ceramics. *Biomed. Mater.* **2013**, *8*. [[CrossRef](#)] [[PubMed](#)]
13. Martínez, I.M.; Velasquez, P.A.; de Aza, P.N. The sub-system α -TCPss-silicocarnotite within the binary system $\text{Ca}_3(\text{PO}_4)_2$ – Ca_2SiO_4 . *J. Am. Ceram. Soc.* **2012**, *95*, 1112–1117. [[CrossRef](#)]
14. De Aza, P.N.; Serena, S.; Luklinska, Z.B. Manufacture and characterization of a new Si-Ca-P biphasic ceramic. *Ceram. Int.* **2018**, *44*, 13623–13629. [[CrossRef](#)]
15. Díaz-Arca, A.; Mazón, P.; de Aza, P.N. Eutectoid scaffold as potential tissue engineer guide. *J. Am. Ceram. Soc.* **2019**, *102*, 7168–7177. [[CrossRef](#)]
16. McDowell, E.M.; Trump, B.F. Histologic fixatives suitable for diagnostic light and electron microscopy. *Arch. Pathol. Lab. Med.* **1976**, *100*, 405–414.
17. Meseguer-Olmo, L.; Aznar-Cervantes, S.; Mazón, P.; De Aza, P.N. “In vitro” behavior of adult mesenchymal stem cells of human bone marrow origin seeded on a novel bioactive ceramic in the Ca_2SiO_4 – $\text{Ca}_3(\text{PO}_4)_2$ system. *J. Mater. Sci. Mater. Med.* **2012**, *23*, 3003–3014. [[CrossRef](#)]
18. Dominici, M.; Le Blanc, K.; Mueller, I.; Slaper-Cortenbach, I.; Marini, F.; Krause, D.; Deans, R.; Keating, A.; Prockop, D.; Horwitz, E. Minimal criteria for defining multipotent mesenchymal stromal cells. The international society for cellular therapy position statement. *Cytotherapy* **2006**, *8*, 315–317. [[CrossRef](#)]
19. De Aza, P.; García-Bernal, D.; Cagnolini, F.; Velasquez, P.; Meseguer-Olmo, L. The effects of Ca_2SiO_4 – $\text{Ca}_3(\text{PO}_4)_2$ ceramics on adult human mesenchymal stem cell viability, adhesion, proliferation, differentiation and function. *Mater. Sci. Eng. C* **2013**, *33*, 4009–4020. [[CrossRef](#)]
20. Golub, E.E.; Boesze-Battaglia, K. The role of alkaline phosphatase in mineralization. *Curr. Opin. Orthop.* **2007**, *18*, 444–448. [[CrossRef](#)]
21. De Jonge, L.T.; Leuwemburg, S.C.G.; van den Beucken, J.J.P.; Wolke, J.G.C.; Jansen, A. Electrosprayed enzyme coatings as bioinspired alternative to bioceramic coatings for orthopedic and oral implants. *Adv. Funct. Mater.* **2009**, *19*, 1–8. [[CrossRef](#)]
22. Hench, L.L. Bioceramics: From Concept to Clinic. *J. Am. Ceram. Soc.* **1991**, *74*, 1487–1510. [[CrossRef](#)]
23. Boyde, A.; Hobdell, M.H. Scanning Electron Microscopy of Lamellar Bone. *Z. Zellforsch.* **1968**, *93*, 213–231. [[CrossRef](#)]
24. Boyde, A.; Hobdell, M.H. Scanning Electron Microscopy of primary membrane bone. *Z. Zellforsch.* **1969**, *99*, 98–108. [[CrossRef](#)]
25. Jayasinghe, J.A.P.; Jones, S.J.; Boyde, A. Scanning electron microscopy of human lumbar vertebral trabecular bone surfaces. *Virchows Archiv. A Pathol. Anat.* **1993**, *422*, 25–34. [[CrossRef](#)]
26. Martínez, I.M.; Velasquez, P.A.; de Aza, P.N. Synthesis and stability of α -tricalcium phosphate doped with dicalcium silicate in the system $\text{Ca}_3(\text{PO}_4)_2$ – Ca_2SiO_4 . *Mater. Charact.* **2010**, *61*, 761–767. [[CrossRef](#)]
27. Ibáñez, J.; Artús, L.; Cuscó, R.; López, A.; Menéndez, E.; Andrade, M.C. Hydration and carbonation of monoclinic C_2S and C_3S studied by Raman spectroscopy. *J. Raman Spectrosc.* **2001**, *38*, 61–67. [[CrossRef](#)]
28. Antonakos, A.; Liarokapis, E.; Leventouri, T. Micro-Raman and FTIR studies of synthetic and natural apatites. *Biomaterials* **2007**, *28*, 3043–3054. [[CrossRef](#)] [[PubMed](#)]
29. Jillavenkatesa, A.; Condrate, R.A. The infrared and Raman spectra of β -and α tricalcium phosphate ($\text{Ca}_3(\text{PO}_4)_2$). *Spectrosc. Lett.* **1998**, *31*, 1619–1634. [[CrossRef](#)]
30. De Brujin, J.D.; van Blitterswijk, C.A.; Davies, J.E. Initial bone matrix formation at the hydroxyapatite interface in vivo. *J. Biomed. Mater. Res.* **1995**, *29*, 89–99. [[CrossRef](#)]
31. Goonoo, N.; Fahmi, A.; Jonas, U.; Gimé, F.; Arsa, I.A.; Bénard, S.; Schönherr, H.; Bhaw-Luximon, A. Improved Multicellular Response, Biomimetic Mineralization, Angiogenesis, and Reduced Foreign Body Response of Modified Polydioxanone Scaffolds for Skeletal Tissue Regeneration. *ACS Appl. Mater. Interfaces* **2019**, *11*, 5834–5850. [[CrossRef](#)]

32. Liao, S.; Watari, F.; Xu, G.; Ngiam, M.; Ramakrishna, S.; Chan, C.K. Morphological Effects of Variant Carbonates in Biomimetic Hydroxyapatite. *Mater. Lett.* **2007**, *61*, 3624–3628. [[CrossRef](#)]
33. Dey, A.; Bomans, P.H.H.A.; Müller, F.A.; Will, J.; Frederik, P.M.; de With, G.; Sommerdijk, N.A.J.M. The Role of Prenucleation Clusters in Surface-Induced Calcium Phosphate Crystallization. *Nat. Mater.* **2010**, *12*, 1010–1014. [[CrossRef](#)]
34. Porter, A.E.; Botelho, C.M.; Lopes, M.A.; Santos, J.D.; Best, S.M.; Bonfield, W. Ultrastructural comparison of dissolution and apatite precipitation on hydroxyapatite and silicon-substituted hydroxyapatite in vitro and in vivo. *J. Biomed. Mater. Res. A* **2004**, *69*, 670–679. [[CrossRef](#)] [[PubMed](#)]
35. Freyman, T.M.; Yannas, I.V.; Gibson, L.J. Cellular materials as porous scaffolds for tissue engineering. *Prog. Mater. Sci.* **2001**, *46*, 273–282. [[CrossRef](#)]
36. Lu, J.X.; Flautre, B.; Anselme, K.; Hardoiun, P.; Gallur, A.; Descamps, M.; Thierry, B. Role of interconnections in porous bioceramics on bone recolonisation in vitro and in vivo. *J. Mater. Sci. Mater. Med.* **1999**, *10*, 111–120. [[CrossRef](#)]
37. Hutmacher, D.W.; Schantz, J.T.; Lam, C.X.; Tan, K.C.; Lim, T.C. State of the art and future directions of scaffold-based bone engineering from a biomaterials perspective. *J. Tissue Eng. Regen. Med.* **2007**, *1*, 245–260. [[CrossRef](#)] [[PubMed](#)]
38. Buckwalter, J.A.; Glimcher, M.J.; Cooper, R.R.; Recker, R. Bone Biology. Part I: Structure, Blood Supply, Cells, Matrix, and Mineralization. *J. Bone Jt. Surg. Am.* **1995**, *77*, 1256–1275. [[CrossRef](#)]
39. Stefanescu, D.M. *Science and Engineering of Casting Solidification*, 3rd ed.; Springer International Publishing: Cham, Switzerland, 2015.
40. Bang, L.T.; Ishikawa, K.; Othman, R. Effect of silicon and heat-treatment temperature on the morphology and mechanical properties of silicon—Substituted hydroxyapatite. *Ceram. Int.* **2011**, *37*, 3637–3642. [[CrossRef](#)]
41. Kim, Y.U.; Lee, B.H.; Kim, M.C.; Kim, K.N.; Kim, K.M.; Choi, S.H.; Kim, C.K.; LeGeros, R.Z.; Lee, Y.K. Effect of Cooling Rate and Particle Size on Compressive Strength of Macroporous Hydroxyapatite. *Key Eng. Mater.* **2006**, *309*–*311*, 1047–1050. [[CrossRef](#)]
42. Kanatani, M.; Sugimoto, T.; Kano, J.; Chihara, K. IGF-I mediates the stimulatory effect of high phosphate concentration on osteoblastic cell proliferation. *J. Cell. Phys.* **2002**, *190*, 306–312. [[CrossRef](#)] [[PubMed](#)]
43. Jones, S.J. Secretory territories and rate of matrix production of osteoblasts. *Calcif. Tissue Res.* **1974**, *14*, 309–315. [[CrossRef](#)]
44. Pazzaglia, U.E.; Congiu, T.; Marchese, M.; Dell'Orbo, C. The shape modulation of osteoblast-osteocyte transformation and its correlation with the fibrillar organization in secondary osteons. *Cell Tissue Res.* **2010**, *340*, 533–554. [[CrossRef](#)]
45. Wu, S.; Liu, X.; Yeung, K.W.K.; Liu, C.; Yang, X. Biomimetic porous scaffolds for bone tissue engineering. *Mat. Sci. Eng. R.* **2014**, *80*, 1–36. [[CrossRef](#)]
46. Pietak, A.M.; Reid, J.W.; Stott, M.J.; Sayer, M. Silicon substitution in the calcium phosphate bioceramics. *Biomaterials* **2007**, *28*, 4023–4032. [[CrossRef](#)]
47. Fielding, G.; Feuerstein, J.; Bandyopadhyay, A.; Bose, S. SiO₂ and SrO Doped β-TCP: Influence of Dopants on Mechanical and Biological Properties. In *Biomaterials Science: Processing, Properties and Applications II*; John Wiley & Sons Inc.: Hoboken, NJ, USA, 2012; Volume 237, pp. 171–181. [[CrossRef](#)]
48. Díaz-Arca, A.; Velasquez, P.; Mazon, P.; De Aza, P.N. Mechanism of in vitro reaction of a new scaffold ceramic similar to porous bone. *J. Eur. Ceram. Soc.* **2020**, *40*, 2200–2206. [[CrossRef](#)]
49. Rey, C.; Combes, C.; Drouet, C.; Sfih, H.; Barroug, A. Physico-Chemical Properties of Nanocrystalline Apatites: Implications for Biominerals and Biomaterials. *Mater. Sci. Eng. C* **2007**, *27*, 198–205. [[CrossRef](#)]
50. Bohner, M.; Lemaitre, J. Can bioactivity be tested in vitro with SBF solution? *Biomaterials* **2009**, *30*, 2175–2179. [[CrossRef](#)]
51. Lutisanova, G.; Palou, M.T.; Kozankova, J. Comparison of bioactivity in vitro of glass and glass ceramic materials during soaking in SBF and DMEM medium. *Ceram. Silik.* **2011**, *55*, 199–207.
52. Theodorou, G.; Goudouri, O.M.; Kontonasaki, E.; Chatzistavrou, X.; Papadopoulou, L.; Kantiranis, N.; Paraskevopoulos, K.M. Comparative Bioactivity Study of 45S5 and 58S Bioglasses in Organic and Inorganic Environment. *Bioceram. Dev. Appl.* **2011**, *1*, 1–4. [[CrossRef](#)]
53. Verné, E.; Ferraris, S.; Vitale-Brovarone, C.; Spriano, S.; Bianchi, C.L.; Naldoni, A.; Morra, M.; Cassinelli, C. Alkaline phosphatase grafting on bioactive glasses and glass ceramics. *Acta Biomater.* **2010**, *6*, 229–240. [[CrossRef](#)] [[PubMed](#)]
54. Verné, E.; Ferraris, S.; Vitale-Brovarone, C.; Cochis, A.; Rimondini, L. Bioactive glass functionalized with alkaline phosphatase stimulates bone extracellular matrix deposition and calcification in vitro. *Appl. Surf. Sci.* **2014**, *313*, 372–381. [[CrossRef](#)]